

EDITORIAL BOARD

Editor-in-Chief

B.E. Paton

Scientists of PWI, Kiev

S.I. Kuchuk-Yatsenko (*vice-chief ed.*),

V.N. Lipodaev (*vice-chief ed.*),

Yu.S. Borisov, G.M. Grigorenko,

A.T. Zelnichenko, V.V. Knysh,

I.V. Krivtsun, Yu.N. Lankin,

L.M. Lobanov, V.D. Poznyakov,

I.A. Ryabtsev, V.F. Khorunov,

K.A. Yushchenko

Scientists of Ukrainian Universities

M.N. Brykov, ZNTSU, Zaporozhie

V.V. Dmitrik, NTU «KhPI», Kharkov

V.V. Kvasnitsky, NSU, Nikolaev

V.D. Kuznetsov, NTUU «KPI», Kiev

Foreign Scientists

N.P. Alyoshin

N.E. Bauman MSTU, Moscow, Russia

Guan Qiao

Beijing Aeronautical Institute, China

A.S. Zubchenko

DB «Gidropress», Podolsk, Russia

M. Zinigrad

College of Judea & Samaria, Ariel, Israel

V.I. Lysak

Volgograd STU, Russia

Ya. Pilarczyk

Welding Institute, Gliwice, Poland

U. Reisgen

Welding and Joining Institute, Aachen, Germany

O.I. Steklov

Welding Society, Moscow, Russia

G.A. Turichin

St. Petersburg SPU, Russia

Founders

E.O. Paton Electric Welding Institute, NASU

International Association «Welding»

Publisher

International Association «Welding»

Translators

A.A. Fomin, O.S. Kurochko, I.N. Kutianova

Editor

N.A. Dmitrieva

Electron galley

D.I. Sereda, T.Yu. Snegiryova

Address

E.O. Paton Electric Welding Institute,

International Association «Welding»

11 Kazimir Malevich Str. (former Bozhenko Str.),

03680, Kiev, Ukraine

Tel.: (38044) 200 60 16, 200 82 77

Fax: (38044) 200 82 77, 200 81 45

E-mail: journal@paton.kiev.ua

www.patonpublishinghouse.com

State Registration Certificate

KV 4790 of 09.01.2001

ISSN 0957-798X

Subscriptions

\$348, 12 issues per year,

air postage and packaging included.

Back issues available.

All rights reserved.

This publication and each of the articles contained herein are protected by copyright.

Permission to reproduce material contained in this journal must be obtained in writing from the Publisher.

CONTENTS

Activities of the E.O. Paton Chinese-Ukrainian
Welding Institute 2

SCIENTIFIC AND TECHNICAL

Belyavin A.F., Kurenkova V.V., Fedotov D.A., Saly S.G.
and *Shcherbinin A.P.* Extension of the life of GTK 10-4 working
blades from EI 893 alloy after long operating period 8

Liang Wang, Yong Hu, Shiyong Song and Jianhua Yao.
Influence of electric-magnetic composite field on WC particles
distribution in laser melt injection 24

Makhnenko O.V., Mirzov I.V. and Porokhonko V.B. Modelling
of residual stresses, radiation swelling and stressed state
of in-service WWER-1000 reactor baffle 32

Babinets A.A. Properties of high-alloyed metal deposited using
electroslag two-strip method 39

INDUSTRIAL

Makhlin N.M. Improvement of electron devices for initial and
repeated ignitions of alternating current arc 43

Burlaka V.V., Gulakov S.V. and Podnebennaya S.K.
State-of-the-art inverter power sources with increased
power factor 48

Paustovsky A.V., Tkachenko Yu.G., Alfintseva R.A.,
Yurchenko D.Z. and Khristov V.G. Composition, structure and
technology for production of electrode materials for electric
spark restoration and strengthening of worn-out parts 53



Activities of the E.O. Paton Chinese-Ukrainian Welding Institute



The E.O. Paton Chinese-Ukrainian Welding Institute (CUWI) is a form of international scientific and technical cooperation in the PRC, which represents a platform for promotion and implementation of achievements and experience of the E.O. Paton Electric Welding Institute (PWI) of the National Academy of Sciences of Ukraine (NASU) and other institutions of the NASU as well as Ukrainian research institutions and enterprises in China and Ukraine, and also to conduct joint developments and joint high-tech production in the field of shipbuilding, marine engineering, aviation, railway transport, extraction and transportation of oil and gas, power engineering, energy saving and other fields of industry with Chinese partners.

Such a form of cooperation has no analogs in the scale of implemented projects.

The establishment of CUWI was approved and affirmed by the following international agreements and documents signed at the level of PWI with the Governmental organizations of China and the documents signed at the level of Ukrainian and Chinese authorities:

- ◆ Agreement on establishment of CUWI, signed by PWI, Guangdong General Research Institute of Industrial Technology (GGRIT) and Guangdong Science and Technology Department on 24 February, 2011;

- ◆ Regulations about CUWI, signed by PWI, GGRIT and Guangdong Science and Technology Department, Guangzhou Science and Information Department on February 24, 2011;

- ◆ Memorandum of Understanding between the Ministry of Science and Technology of PRC and the State Agency for Science, Innovation and Information of Ukraine and rendering support for establishment of CUWI, signed in May 2011;

- ◆ Intergovernmental agreement between PRC and Ukraine on economic and scientific-technical cooperation signed in the framework of the State visit of the Head of PRC to Ukraine in 8–20 of June, 2011.

At present, according to the Chinese legislation, CUWI, which is a part of the Guangdong Academy of Sciences. All the activities on international cooperation in the frames of CUWI are funded by the Chinese party. The sources for receiving funds of the Chinese party are the applied projects of the PRC Central Government, Government of Guangdong Province, Guangzhou, or state industrial corporations as well as joint-stock and private companies in the PRC. The financial support of projects is carried out on a competitive basis, i.e. to receive funds in China for each project in the



Signing of official documents on establishment and activity arrangement of CUWI (2012–2013): *from left to right*: Mr. Zhu Xiaodan, Governor of Guangdong Province; Prof. B.E. Paton, President of the NASU, Honorary Chairman of the CUWI Council; Mr. Cao Jianlin, Deputy Minister of Science and Technology of PRC, Honorary Chairman of the CUWI Council; I.V. Krivtsun, Academician of the NASU, Deputy Director of PWI, Chairman of the CUWI Council



Equipment for flash-butt welding, developed at PWI and delivered to the laboratory and technological base of CUWI in Guangzhou

competition the state institutions and enterprises of PRC, as well as leading foreign companies in the field of welding and related processes are involved.

Within the scope of CUWI in realization of international projects a number of institutes of the NASU, leading technical universities of Ukraine as well as large industrial enterprises and research-and-production innovation companies participate. In particular, except of PWI in such cooperation within the framework of CUWI, I.M. Frantsevich Institute of Problems of Materials Science and Physical-and-Technological Institute of Metals and Alloys participate. Among technical universities in international projects in the framework of CUWI, NTUU «Kiev Polytechnic Institute» and Admiral Makarov National Shipbuilding University most actively participate. Also, for the fulfillment of production tasks, in particular, for production of critical units of high-tech equipment, CUWI attracts a number of industrial, scientific-and-industrial enterprises from different regions of Ukraine, in particular, from Dnepropetrovsk, Kharkov, Zhitomir, Nikolaev, Kiev, Sumy and other cities of Ukraine.

Main directions of works and joint projects in the PRC on which CUWI is currently working:

- ◆ development of universal equipment and technology of flash-butt welding of structural steels, aluminum and titanium alloys and their industrial application;



Prototype of machine for producing welded joints of titanium and titanium alloys of up to 4 m length and up to 120 mm thickness (a), and macrosection of welded joint of titanium of increased thickness (b)



Innovative universal equipment for plasma, hybrid and combined (tandem) plasma-MIG welding, developed at PWI and delivered to the laboratory and technological base of CUWI in Guangzhou

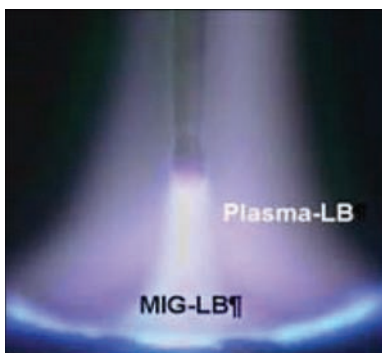
- ◆ creation of new generation of equipment for flash-butt welding of pipes (114–320 mm), preparation of organization of its joint production in the PRC;

- ◆ creation of advanced flux-cored wires for arc welding of high-strength steels, surfacing and spraying, development of technology for their production, including improvement of reliability and longevity of critical structures of high-strength steels of the offshore platforms for oil and gas production;

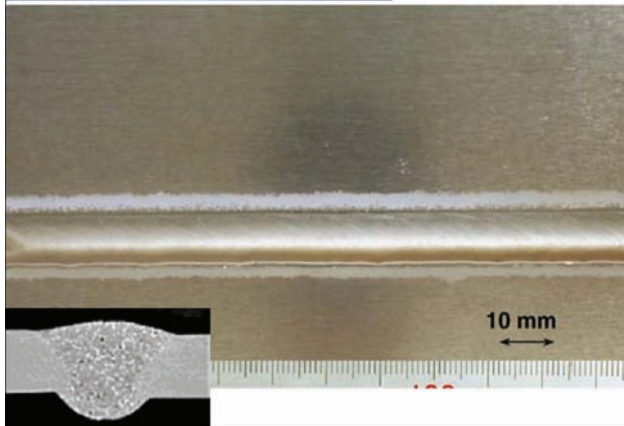
- ◆ creation of technology and universal equipment for high-speed plasma, hybrid and combined (tandem) plasma-MIG welding, its integration into robotic complex;

- ◆ development of technology and equipment for orbital welding over the flux layer (A-TIG) of pipelines for power equipment;

- ◆ creation of technology and new generation of equipment for microplasma (plasma) and hybrid laser-microplasma (plasma) welding using pulsed current at variable-polarity modes;



Hybrid «Plasma-MIG» welding process

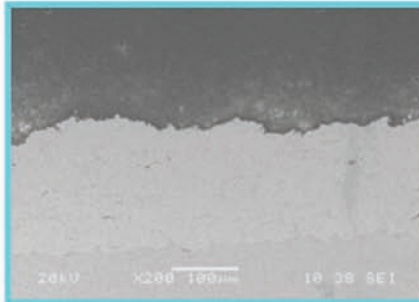
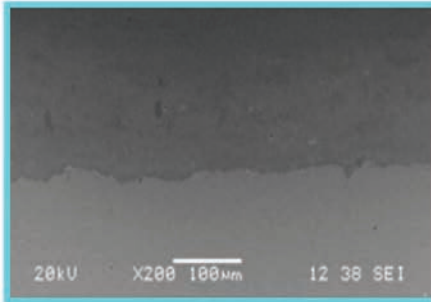
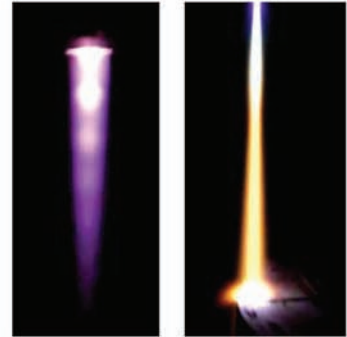


Appearance of weld of Al-3 % Mg alloy produced using hybrid «Plasma-MIG» process ($\delta = 5$ mm, $v_w = 50$ cm/min)



Line for production of flux-cored wires for arc welding, surfacing and thermal spraying at the laboratory and technological base of CUWI in Guangzhou





b Cr₂O₃

Al₂O₃

WC-17Co

Appearance of equipment, supersonic plasma spraying process, developed at PWI and delivered to the laboratory and technological base of CUWI in Guangzhou (a), and produced high-quality ceramic and metal-ceramic coatings (b)

- ◆ development of technology of diffusion welding of Ni₃Al-based heat-resistant alloys with controlled stress-strain state;
- ◆ modification of equipment for high-frequency welding of live tissues, its adaptation to the working conditions at the Chinese medical institutions;



Laser welding and cutting as well as hybrid laser welding with two robots using 10 kW laser at the laboratory and technological base of CUWI in Guangzhou (deep penetration laser welding, hybrid laser-MIG welding, laser welding using scanning, laser welding using two beams, 3D laser cutting)

焊接研究与应用

WELD RESEARCH AND APPLICATION



2016年6月行第一期 设备·材料·工艺·资讯

Journal published by CUWI with papers of Chinese and Ukrainian specialists

- ◆ development of new compositions of powders of high-strength titanium alloys and technologies of their production applying plasma technologies;

- ◆ development of new technologies for plasma titanium-steel welding and their introduction into production of bimetallic pipes for oil and gas transportation;

- ◆ creation of specialized equipment and technology of orbital plasma welding of titanium pipes for the needs of oil and gas production;

- ◆ creation of specialized equipment and technology of high-efficient (up to 45 kg/h) electroslag two-strip surfacing of large products of power engineering equipment;

- ◆ creation of equipment and technology of electrodynamic treatment of welded joints of aluminum alloys for shipbuilding with the purpose of efficient reduction and control of welding deformations;

- ◆ development of technology and equipment for high-efficient plasma cutting of metals of high thicknesses (up to 120–200 mm) at reverse polarity, its integration with the systems of numerical program control as-applied to the produc-

tion of large-size structures;

- ◆ development of technology and equipment for automatic narrow-gap arc welding in controlled magnetic field of long structures (up to 4 m) of titanium alloys of increased thickness (up to 120 mm);

- ◆ development and application of advanced technologies for manufacture and repair of gas turbine blades based on advanced welding and electron beam technologies;

- ◆ development of innovative technologies for welding, cutting and life improvement for manufacture of hull structures of vessels (including polar transport icebreakers) using advanced welding-and-assembly processes.

Creation of laboratory and technological base of CUWI in the PRC. To carry out joint works on realization of projects of international scientific and technical cooperation at the facilities of CUWI in the PRC, the laboratory and industrial areas were created, where at the moment more than 25 different types of experimental-industrial equipment were installed, including those developed at PWI and supplied by the Ukrainian part, namely, line for production of new types of flux-cored wires for welding, surfacing and spraying; equipment for flash-butt welding (two installations for welding of



Awarding the CUWI Director on the PWI part V.N. Korzhik (from the left) (from the right: Vice Premier of the PRC State Council Ma Kai)

pipes and parts of other profiles); equipment for welding of live tissues (4 devices); universal equipment for hybrid and combined (tandem) plasma-MIG welding; installation for A-TIG welding; installation for supersonic plasma spraying of coatings; high-power laser (10 kW) and equipment for laser and hybrid laser-MIG welding; different equipment for arc welding (TIG, MIG, friction, FSW, etc.), as well as the equipment for arc surfacing and high-efficient electroslag two-strip surfacing.

Scientific achievements of CUWI. In the process of international scientific and technical cooperation in the CUWI framework, the following basic scientific achievements in the field of fundamental investigations of physical processes of transfer of energy, mass and charge in arc, plasma, laser, hybrid plasma-arc and laser-arc welding, plasma spraying, for the development of new innovative technologies and related equipment on this basis, were gained:

- ◆ software for theoretical investigations and computer modeling of processes of transfer of energy, pulse, mass and charge in column and anode region of welding arcs, as well as for numerical modeling of thermal field and field of dynamical changing in the weld pool in hybrid laser-arc welding was developed;

- ◆ mathematical models and software for calculation of temperature field, field of velocities and electromagnetic characteristics of arc plasma generated by plasmatrons of direct action, characteristics of thermal and dynamic interaction of plasma with the material being welded, were developed;

- ◆ computer program for modeling (calculation of dimensions and shape) of single-pass butt welds in A-TIG welding was developed;

- ◆ computer program for mathematical modeling of stress-strain state and mechanical properties of material in the zone of circumferential butt welded joint in arc welding (A-TIG and TIG) was developed;

- ◆ technological principles of hybrid plasma welding with axial current-carrying wire («Plasma-MIG») were developed, technical solutions for creation of hybrid plasmatrons and installations for plasma hybrid welding were created.

Using opportunities of CUWI in China, PWI participates actively in international conferences and exhibitions on welding and related technologies with reports on developments and experience of PWI in implementation of welding technologies. Keeping the course of CUWI, the PWI staff members delivered nearly 25 reports at the international scientific and technical conferences, published more than 35 scientific papers in different leading top-rated scientific and technical journals of the PRC, as well as in the USA, Ukraine, EU and other countries, prepared nearly 30 scientific papers for publication. The applications for 10 patents were submitted in the PRC, 19 patents were prepared for submission in the PRC and Ukraine.

Estimates of the CUWI activity results. CUWI has a high prestige in the PRC, the activity results of CUWI and contribution of PWI to this activity were highly appreciated by the PRC Government. In particular, Prof. Korzhik V.N., Director of CUWI on the PWI part, was awarded a number of governmental awards and titles of PRC (Medal of Guangdong Government «For high achievements in international scientific-technical and economic cooperation», 2013, and highest award of the PRC Government and the State Administration of Foreign Experts, 2014) and also was awarded with honorary titles (international expert of the Chinese Ministry of Human Resources and Social Security, honorary citizen of Guangzhou).

Prof. Korzhik V.N.,
CUWI Director on the PWI part

EXTENSION OF THE LIFE OF GTK 10-4 WORKING BLADES FROM EI 893 ALLOY AFTER LONG OPERATING PERIOD

A.F. BELYAVIN¹, V.V. KURENKOVA¹, D.A. FEDOTOV¹, S.G. SALY² and A.P. SHCHERBININ²

¹«Paton Turbine Technologies» Ltd.

26 Raketnaya Str., 03028, Kiev, Ukraine. E-mail: VKurenkova@patontt.com

²Repair Enterprise «Ukrgazenergoservis», Subdivision of PJSC «Ukrtransgaz» of NJSC «Naftogaz Ukrainy»
49 Mayakovsky Str., 08151, Boyarka, Ukraine

During prolonged operation (thousands of hours) degradation of base material — EI 893 alloy — proceeds in working blades of GTK 10-4 unit under the impact of static and dynamic loads, temperature gradient, fuel combustion products, etc. Structural changes in the basic blade alloy influence the changes of its mechanical properties, compared to metal in initial state, namely, increase of ultimate strength, yield limit, hardness values and lowering of ductility characteristics take place and, therefore, also lowering of their creep resistance and high-cycle fatigue. For this reason, extension of service life of expensive items in turbine hot section is an extremely important task, which is solved by integrated restoration of initial structure and mechanical properties of EI 893 alloy. The objective of this work was studying GTE material state after operational aging on seven working blades (from sets with different operating lives), determination of their reparability and selection of modes of recovery heat treatment. It was found that during long operation periods at the temperature of 630–670 °C an essential change of structural-phase state of base material proceeds in the working blades, which is manifested in dissolution, coagulation and non-uniform distribution of strengthening phase in matrix solution volume and carbide precipitation on subgrain boundaries within the grains and on grain boundaries, and formation of carbides of a more complex composition. It was established that optimum base structure with sufficient hardness and microhardness forms at two-step recovery heat treatment, namely, a certain reduction of difference in grain dimensions (mainly, 2–4 grain size point), reduction of density and dimensions of stable carbide phases in intergranular interlayers, and uniform and regular distribution of disperse strengthening phase. Structure recovery after recovery heat treatment leads to improvement of ductile characteristics ($\delta = 33.2\text{--}35.6\%$) and, consequently, also of fatigue resistance at admissible values of strength and fracture toughness, that, on the whole, ensures the serviceability of reconditioned items. 16 Ref., 5 Tables, 10 Figures.

Keywords: *high-pressure turbine (HPT), low-pressure turbine (LPT), recovery heat treatment (RHT), hardness, microhardness, ultimate strength, yield limit, ductility, fracture energy, deposited weld, heat-affected zone*

Working blades of gas-pumping units (GPU) drive turbines are operating in combustion products of fossil fuel under complex temperature conditions, where the concurrent factors are high working temperature of gas flow; significant temperature gradients between the airfoil root and middle part; cyclic thermal stresses (starting, stopping, etc.); simultaneous impact of static tensile (centrifugal) forces; bending loads arising from the impact of pulsed gas flow and dynamic vibratory stresses.

When addressing the problems of reliability and extension of working blade operating life, the main element is control of structural changes proceeding in blade material, which lead to lowering of resistance to creep and high-cycle fatigue of metal, as about 80 % of unforeseen fractures of parts in turbine hot section in service are of exactly fatigue nature. Magnitude of alternating loads can be up to 50–80 MPa, and total (equivalent) stresses, applied to blades in turbine I stage, reach 150 MPa [1].

At present a significant number of GTK 10-4 GPU are operating in Ukraine in the main gas pipelines. Most of the units have exhausted their service life specified by manufacturer-plant, and, in keeping with industrial safety requirements in gas line compressor stations [1, 2], the need arises to provide engineering and economic substantiation of the approach to extension of the life of the main parts for a maximum term. This, primarily, pertains to extension of the period of safe and reliable operation of working blades of HPT, made from EI 893 alloy, which consists in providing the full cycle of RHT alongside performance of the required stages of welding/brazing repair. Solving the problem of maximum extension of GTK 10-4 GPU life is associated, in particular, with taking out of service and conducting destructive testing of material of the most representative main parts of GPU with maximum operating life, in order to determine the influence of operational factors on mechanical properties.

Wrought high-temperature alloy EI 893 VD has become extensively applied in manufacture of work-

ing blades of gas-turbine unit (GTU) of GTK 10-4, GTN-16, GT-100-750 type and other critical parts of drive turbines with operating life measured in tens of thousands of hours. Influence of long-term operation on EI 893 alloy structure and its physico-mechanical properties is considered in detail in [1–3].

Experience of PWI work on deposition of protective condensed coatings on working blades of energy turbines of peak power, made from EI 893 VD alloy, and application in this process of RHT, accepted by the enterprises of FSU Ministry of Power Engineering, allowed realization of a similar mode of reconditioning of GTK 10-4 unit working blades made from the same alloy.

Selected and approved mode of three-stage heat treatment is applied many times in reconditioning EI 893 alloy blades after different operating periods. However, under the conditions of saving the energy resources and in order to lower the cost of reconditioning repair of working blades, a decision was taken to optimize (simplify) the modes of EI 893 alloy heat treatment with preservation of all the properties and operational reliability of GTK 10-4 HPT and LPT items in further operation.

Materials and experimental procedure. «Paton Turbine Technologies» Ltd. performed assessment of reparability of four sets of HPT working blades and three sets of LPT working blades (564 pcs all together) after different periods of operation in GTK 10-4 unit. Blades with a large number of defects were selected from each set (one from each set) for cutting up and conducting comprehensive metallographic examination, both after operation and after various kinds of RHT. Samples from blade edges, cut-off before building-up and from the root were used for performance of research of impeller sets of EI 893 alloy working blades (HPT + LPT).

The structure of metal of GTK 10-4 working blades was studied using the techniques of optical and scanning electron microscopy, tensile mechanical testing at 20 and 750 °C in air, measurement of metal hardness and microhardness in the blade root

and airfoil. Microstructural examination of the samples was performed in electron microscope CamScan with energy-dispersive X-ray microanalyzer Energy 200 (with INCA software). Microhardness of the base in different states was determined with application of Micro-Duromat 4000E instrument at 0.5 N load, and Brinell hardness was measured in TSh-2M instrument.

RHT of blades and samples was performed in laboratory SNV furnace and industrial Abar furnace at residual gas pressure not higher than $1 \cdot 10^{-4}$ Torr.

Sample testing for uniaxial tension was conducted in upgraded rigid-type R-0.5 machine, and dual cantilever load cell was used as force measure device. Force measure device was pre-calibrated using reference dynamometer of the Chamber of Weights and Measures. Tension chart was recorded in P – τ coordinates (kg–min) by KSP-4 recorder.

Results and discussion. As is known, prolonged operation of working blades results in essential changes of structural-phase state base material, i.e. its degradation takes place. This is manifested in the change of both grain structure, and fine ($\gamma + \gamma'$) structure of the alloy, running of phase transformations, etc. Operational ageing leads to lowering of fatigue resistance (endurance limit) of blade metal, as, consequently, reliability of operation of the turbine unit as a whole.

For instance, lowering of fatigue properties (by 20 %) in GTK 10-4 working blades from EI 893 alloy is observed after 40,000–60,000 h of operation at temperature of 630–670 °C, which is the result of microstructural changes in base alloy. Thus, the structural factor predominates during operation of EI 893 alloy working blades: quantitative transformations of some alloy components as a result of material ageing at exposure to high-temperature gas flow and stresses developing in the parts.

Metallographic investigations of initial samples cut out of seven working blades (after different operating time) consisted in determination of alloy chemical composition (including carbon content), evaluation of grain structure; measurement of hardness and

Table 1. Some characteristics of EI 893 alloy of GTK 10-4 working blades after undetermined operating period in different HPT and LPT sets

Blade number	Blade type	Grain point	Characteristics of strengthening γ' -phase		Hardness HB , MPa	Micro-hardness H_{μ} , MPa	Carbon content, wt.%
			Volume fraction, %	Particle size, μm			
0084	RL 1 st TVD	2–4	7	0.05–0.17	2058	3017	0.040
0103	RL 1 st TVD	2–3	8–9	0.02–0.16	2342	3518	0.051
0240	RL 1 st TVD	2	7–8	0.05–0.18	2165	2998	0.046
0285	RL 1 st TVD	2–3	10–11	0.01–0.03	2264	3519	0.043
0369	RL 2 st TVD	3	4–5	0.01–0.10	2244	3447	0.042
0430	RL 2 st TVD	4	7–8	0.05–0.10	2957	3947	0.062
0760	RL 2 st TVD	3	8–9	0.02–0.10	2999	4040	0.038

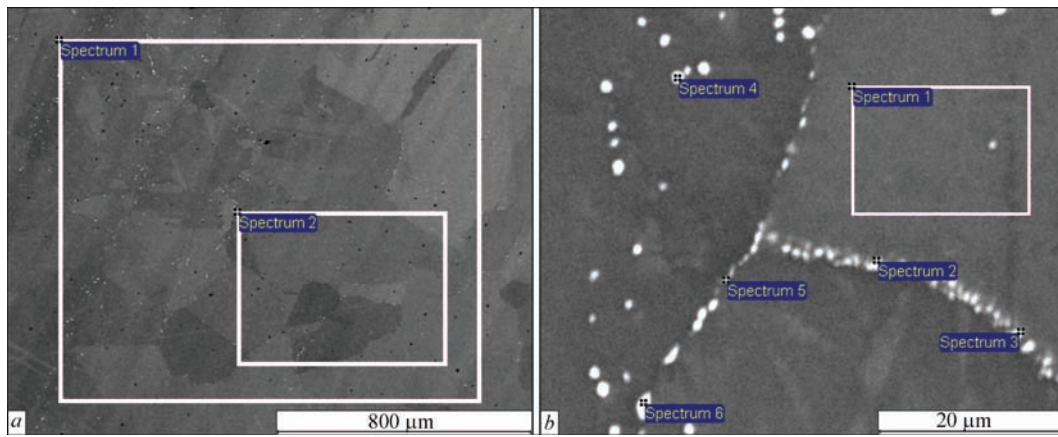


Figure 1. Regions of EDXA performance over sectional area of the sample fragment (*a*) and locally on phases on triple boundary of EI 893 alloy after operation (*b*)

microhardness, evaluation of fine ($\gamma + \gamma'$)-structure, determination of phase composition and distribution of secondary phases (Table 1). It was established that chemical composition of seven blades from different sets fully corresponded to specified alloy EI 893 (Kh-N65VMTYu), wt.%: Ni-(15–17)Cr-(3.5–4.5)Mo-(8.5–10)W-(1.2–1.6)Al-(1.2–1.6)Ti-0.6Mn-0.6Si- $<3\text{Fe}$ - $<0.07\text{C}$, in particular for carbon (Table 2; Figure 1, *a*).

At in-coming inspection of working blade sets after operation at working temperatures, erosion-corrosion damage, nicks, dents, etc. were found on the rejected blade surface. Blade material did not have cracks, but structure of blades after different operating periods was characterized by 2–4 point grain (78–177 μm) to GOST 5639–82, and difference in material grain size was also observed (Figure 2, *a, c*).

After long-term operation of blades (about 60,000 h) cracks can initiate on base alloy grain boundaries (where grains have different size) during subsequent operation, in view of different deformability of coarse and fine grains. Cracks can be of both transcrystalline and intragranular nature. Authors of [4] studied the influence of grain size on structural fatigue strength of blades (32 pcs) from EI 893 alloy,

and established that the dimensional factor of grain size (from 0.5–1.0 to 3–5 mm) only slightly influences the level of fatigue strength. It was determined that at asymmetrical loading and room temperature the increase of grain size from 0.1–0.35 to 0.4–1.5 mm leads to lowering of blade endurance limit by just 4.6 %, and this enables allowing the presence of regions with up to 1.5 mm grain size, in the structure of EI 893 alloy working blades for stationary GTU, without any adverse influence on item serviceability. The same authors also showed [4] that fatigue crack initiation is influenced to a greater extent by defects of mechanical origin and variation of edge rounding-off radius.

During long-term operation the level of mechanical properties of metal of working blades from EI 893 alloy is characterized by a change of ductility and strength values, compared to metal in the initial state: metal ductility decreases at simultaneous increase of *HB* hardness and ultimate strength and yield limit. Lowering of impact toughness, notch sensitivity and fatigue properties is associated with ductility lowering. Change of mechanical characteristics is due to structural changes in the metal in operation, i.e. during operation at blade working temperature of

Table 2. Chemical composition of base alloy of GTK 10-4 I stage blades after undetermined operating period (blade 0084)

Spectrum number	Al	Ti	Cr	Ni	Mo	W	C
Chemical composition of EI 893 alloy after operation (airfoil) (acc. to Figure 1, <i>a</i>)							
1	1.29	1.36	16.37	67.78	4.52	8.68	0.04*
2	1.24	1.36	16.8	68.48	3.95	8.17	
EI 893 regular composition	1.2–1.6	1.2–1.6	15–17	60.9–60.6	3.5–4.5	8.5–10	≤ 0.07
Chemical composition of phases in EI 893 alloy matrix after operation (airfoil) (acc. to Figure 1, <i>b</i>)							
1	1.15	1.17	16.61	65.13	3.80	8.79	3.34**
2	0.87	1.23	14.79	43.37	10.64	20.60	8.49**
3	1.03	1.26	14.36	46.69	9.67	18.32	8.69**
4	0.48	0.68	11.33	25.88	13.58	36.93	10.49**
5	1.10	1.23	15.43	58.52	5.02	10.92	7.78**
6	0.46	0.77	11.68	25.04	14.64	36.47	10.94**

*Carbon content measured by the method of burning a sample in oxygen environment.
**Carbon content determined by qualitative EDXA.

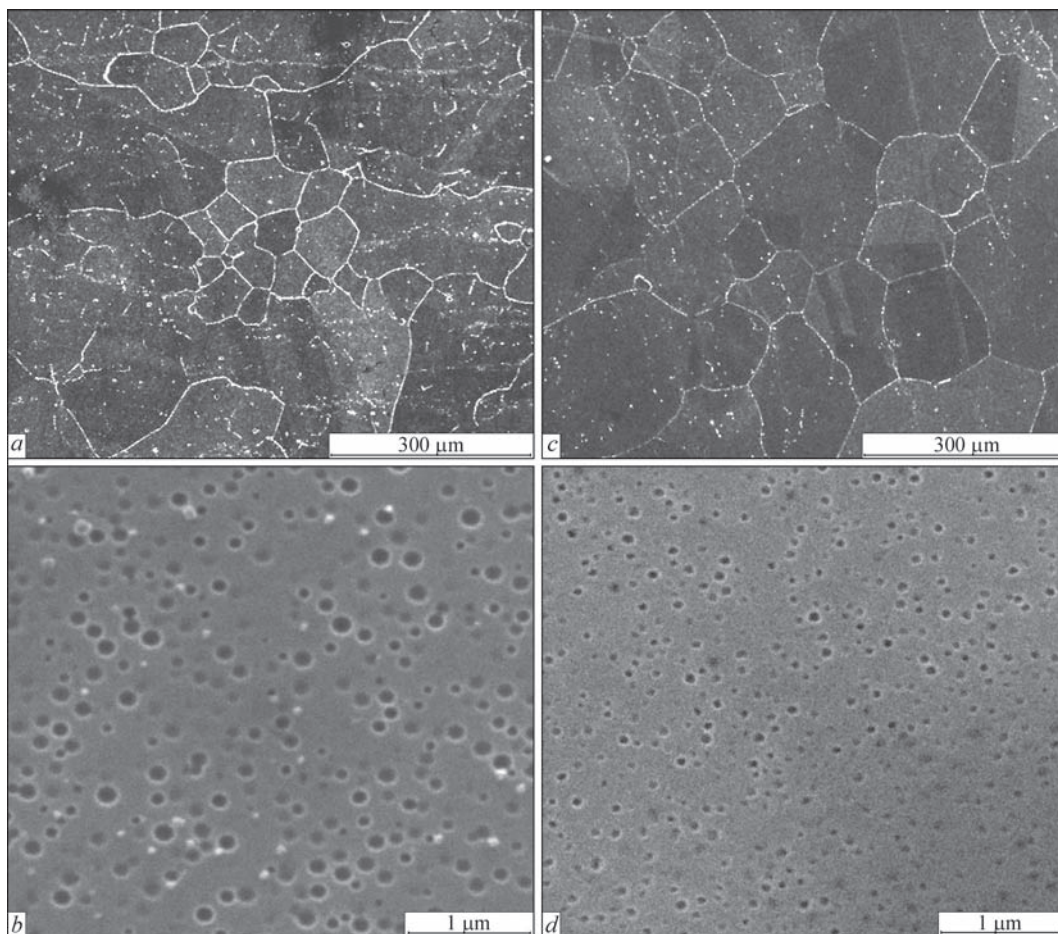


Figure 2. Micro- and macrostructure of alloy in blades 0084 (*a, c*) and 0764 (*b, d*) after different operating periods

630–670 °C ageing of EI 893 alloy leads to additional precipitation and coagulation of particles of both strengthening γ' -phase, and carbides of MeC, Me_6C , Me_{23}C_6 type in the grain bulk and on the boundaries [5]. Decomposition of MeC and Me_{23}C_6 carbides can lead to formation of particles of a more complex M_6C carbide. Carbide coarsening and coalescence in intergranular interlayers to 0.5–6.0 μm , partial fringing of the boundaries by γ' -phase particles can have an adverse effect: reduction of blade metal relative elongation to 20–28 %. So, decrease of yield limit over 60,000 h of operation is equal to 250 MPa on average, i.e. fracture toughness decreases and cracking probability rises [6].

In seven studied blades after different operation periods the structure is characterized, primarily, by irregular distribution (4–11 vol.%) of the main strengthening phase of 0.01–0.18 μm size in matrix solution volume, i.e. its partial dissolution, coagulation and running of carbide reactions, proceeding mainly on grain boundaries with further coagulation of carbide phases (Figure 2, *b, d*). After operation these carbide phases mainly are globular MeC carbides (based on W, Mo, Cr), their size not exceeding 2 μm (see Table 2 and Figure 1, *b*).

Hardness is a mechanical characteristic of material, the value of which is correlated reliably with the values of yield limit (ultimate strength) of tested material in a broad temperature range. To assess the properties of blades after long service or RHT operations, a control operation of measurement of blade metal hardness *HB* is necessarily used, usually, on root end face in the vicinity of 1st tooth, where the part area allows producing the respective imprint by pressing down the indenter — sphere of 10 mm diameter with 3000 kg force.

Real working blades demonstrate a noticeable scatter of physico-mechanical properties by item height, whereas the blade root is not exposed to any significant temperature impact in operation, compared to its profile part (i.e. root metal can characterize the alloy properties in the initial state). As is seen from Table 1, the most probable hardness values of EI 893 VD alloy in blades with different operating times are in the range of *HB* 2058–2999, and are indicative of the fact that 60 % of all the studied blades have hardness close to that of initial material (*HB* 2170–2770) and correspond to the level of *HB* values earlier obtained on GT-100 and GTK 10-4 working blades, that is in agreement with the data of authors of [6–8].

In the case of working blades 0430 and 0760, EI 893 alloy hardness was equal to HB 2957–2999. These rather high hardness values and slight increase of microhardness were indicative of development of metal ageing process, and in the case of blade 0760 — of structure overageing in operation with precipitation of ultrafine phase of 0.01–0.03 μm (see Table 1). Quite high hardness values could also be determined by stamping deformation texture and inherited texture of recrystallization and carbide striation in an actual item.

Structural changes in base alloy as a result of long-term operation are reversible. It requires application of RHT in vacuum, which restores physico-mechanical properties of working blade metal (in particular, EI 893 alloy) to the level, corresponding to initial state (before operation).

Application of three-stage heat treatment of working blades of power GTU HPT at some time (1980s) provided high operating reliability of peak power turbines even with gas temperature increase. RHT mode did not lower the strength properties of metal, including structural endurance of blades and provided a high level of base alloy properties, not differing from (or even exceeding) the level of metal properties after standard multistage heat treatment after billet stamping, namely: 1020 °C, 2 h + 1160 °C, 3 h, air + 1000 °C, 4 h, air + 900 °C, 8 h, air + 850 °C, 15 h, air.

RHT of blades after operation is traditionally performed in vacuum furnaces with forced cooling by argon in the following mode: heating to 1040 °C, 4 h, cooling to 300 °C, heating to 900 °C, 8 h, cooling to 300 + 820 °C, 15 h. Cooling rate should be not lower than 12 deg/min in high-temperature cooling section (to 650 °C).

Earlier studies of reference blades of industrial batches of HPT and LPT I and II stages (EI 893 alloy) of GT-100-750 power unit after three-stage RHT showed that at 20 °C the main test results for yield limit fall within the range of 500–600 MPa, and ultimate strength exceeds 900 MPa (reaching 1040 MPa), elongation at fracture is more than 20 % with 30–40 % maximum of values. A certain scatter of values was observed for impact toughness with a maximum in the range of 60–80 J/cm².

To recover the service properties of blades from EI 893 alloy, the authors of [6] proposed a simplified (two-stage) RHT schematic: annealing in argon at 1050 °C (2 h), rapid cooling, heating to 850 °C, soaking for 5 h, and cooling by argon.

No significant change of alloy phase composition occurs as a result of RHT. Metal M_6C remains the main carbide phase. Quantity of strengthening γ' -phase somewhat decreases and corresponds to initial state

(before operation). After RHT, blade metal hardness level decreases, and ductile characteristics increase, reaching initial values. Authors of [7] also considered two-stage RHT after operation (1050 °C 3 h, cooling in air, and subsequent ageing at 850 °C (12 h), cooling in air) and studied EI 893 alloy mechanical properties after it. It was shown that two-stage treatment provides optimum values of structural and mechanical properties (so, relative elongation is equal to 36 % at ultimate strength of 920 MPa).

In connection with the need for build-up welding of blade end seal, the blades after operation should be subjected to austenitizing (vacuum annealing) at 1160 °C and residual gas pressure of $1 \cdot 10^{-4}$ Torr in the working chamber. Blade material structure as a result of annealing becomes close to single-phase one and acquires the ability to be welded in a satisfactory manner without crack initiation. After welding and machining of built-up sections, the parts are subjected to RHT by 1040 + 900 + 820 °C mode. Therefore, GTK 10-4 working blades, coming in for repair and reconditioning after various periods of operation, should be subjected to four-stage heat treatment, including primary homogenizing before building-up (welding) and three-stage ageing. Three RHT variants (with different duration of stages) were considered in order to select and optimize the modes:

- 1160 + 1040 + 900 + 820 °C (four-stage);
- 1160 + 900 + 820 °C (three-stage);
- 1040 + 820 °C (two-stage).

All the samples, cut out of seven sectioned blades after different operation periods, were taken through the stages of one of the three heat treatment variants. Changes in base material structure were studied after each RHT stage. So, after homogenizing at 1160 °C, grain coarsening, fine grain boundary dissolution and partial dissolution of coarse grain boundaries were observed. In such a mode not only the main strengthening γ' -phase, but also carbide phases in the grain middle and on their boundaries dissolve to the maximum degree (Figure 3, *a*). After homogenizing, the secondary phases are represented by dispersed particles (1–2 μm) of stable carbide phases of MeC type based on tungsten and molybdenum (Table 3; Figure 4, *a*).

Me_6C carbide forms at 1030 °C, so that at heat treatment at close temperature it is exactly the main carbide phase, that lowers the possibility of carbide reactions running during subsequent operation (this carbide is stable up to 1250 °C and in high-temperature alloys it can form from the melt). After long-term operation at higher temperatures of operational ageing (for instance, blade airfoil), this carbide can transform into $\text{Me}_{12}\text{C}-\eta$ carbide, belonging to the same

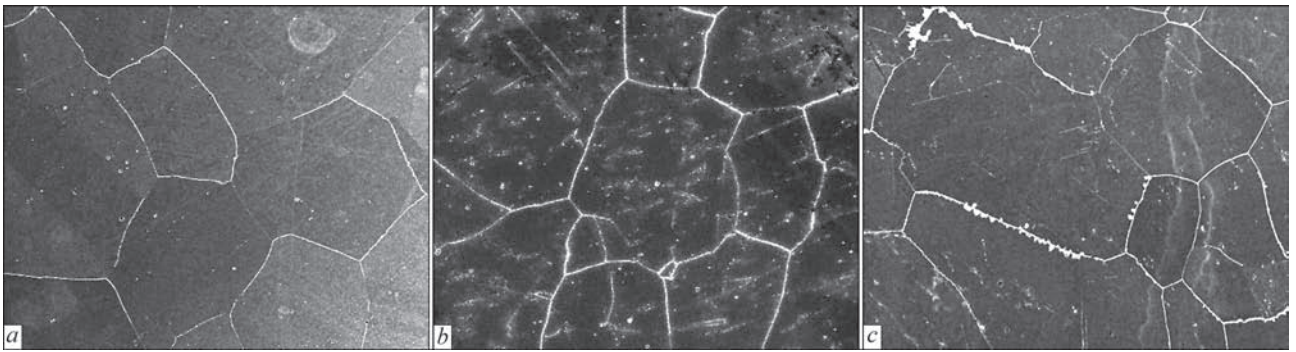


Figure 3. Macrostructure ($\times 100$) of alloy on blades after different RHT stages: *a* — 1160; *b* — 1160 + 1040; *c* — 1160 + 1040 + 900 °C

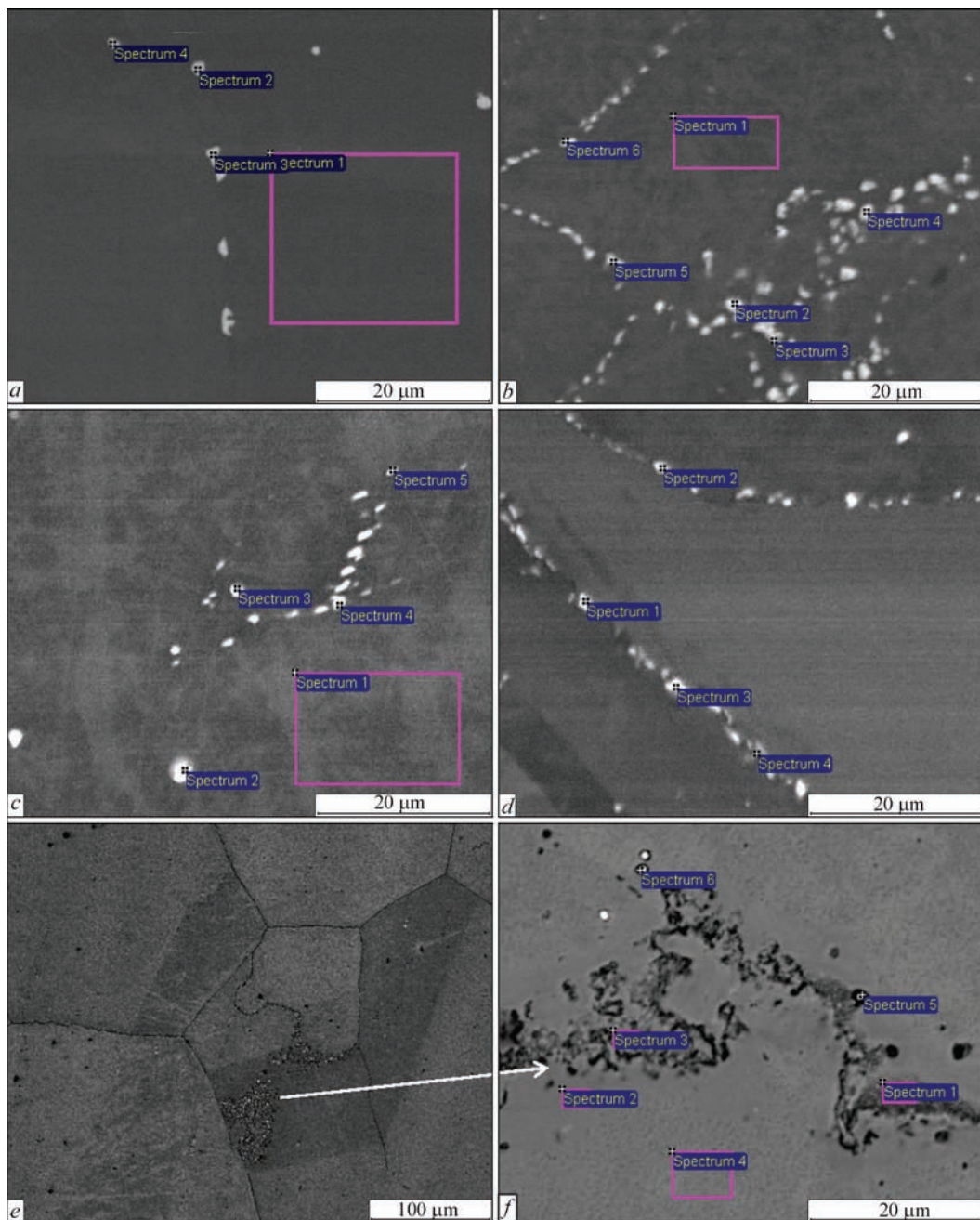


Figure 4. Regions of determination of chemical composition of EI 893 alloy structural components after different stages of heat treatment: *a* — 1160; *b* — 1160 + 1040; *c* — 1040 + 820; *d* — 1160 + 1040 + 900 + 820; *e, f* — 1160 + 900 + 820 °C

Table 3. Chemical composition of phases in matrix of EI 893 alloy after different heat treatment stages

Spectrum number	C	Al	Ti	Cr	Fe	Ni	Mo	W
After homogenizing at 1160 °C (acc. to Figure 4, a)								
1	3.27	1.48	1.69	15.81	0.05	64.95	4.32	8.44
2	9.91	0.24	0.45	16.68	0.24	11.80	20.11	40.57
3	9.37	0.12	0.69	15.53	0.24	19.72	17.52	36.81
4	8.64	0.64	0.72	17.36	0.27	21.74	18.34	32.29
After homogenizing at 1160 + 1040 °C (acc. to Figure 4, b)								
1	3.47	1.25	1.39	15.55	–	65.17	3.72	9.44
2	9.04	0.67	0.93	16.31	–	38.37	11	23.68
3	8.90	0.60	0.99	13.12	–	40.92	10.59	24.89
4	7.25	1.32	1.34	16.18	–	55.71	5.29	12.90
5	7.64	1.12	1.30	15.84	0.36	56.65	4.93	12.16
6	7.89	1.32	1.37	15.51	0.35	61.85	3.56	8.15
After heat treatment at 1040 + 820 °C (acc. to Figure 4, c)								
1	2.95	1.11	1.10	15.91	–	65.63	3.68	9.61
2	11.59	–	0.65	2.10	–	29.22	48.11	8.34
3	9.41	0.60	0.88	12.50	–	34.29	12.33	29.99
4	7.25	0.42	0.71	12.37	–	28.50	15.03	35.73
5	5.66	1.10	1.31	15.29	–	61.95	3.74	10.95
After heat treatment at 1160 + 1040 + 900 + 820 °C (acc. to Figure 4, d)								
1	9.83	0.45	1.06	12.79	0.47	33.13	12.55	29.72
2	6.09	1.02	1.33	15.24	0.54	64.29	3.76	7.73
3	5.14	1.24	1.60	16.10	0.42	55.31	6.28	13.91
4	6.14	2	1.87	23.11	0.16	51.20	5.65	9.86
After heat treatment at 1160 + 900 + 820 °C (acc. to Figure 4, f)								
1	8.17	0.65	0.87	19.74	1.56	56.69	3.84	8.47
2	4.27	0.98	1.08	16.29	1.85	63.86	3.18	8.48
3	6.74	0.65	0.73	23.16	1.57	52.96	4.55	9.63
4	3.70	1.09	1.12	15.38	1.65	64.07	3.76	9.23
5	3.18	0.19	0.57	22.77	1.02	34.20	11.69	26.38
6	4.46	0.68	0.98	17.79	1.56	57.95	4.72	11.86

class of stable carbides. Thus, after high-temperature ageing stage, Me_6C and primary MeC carbides are the secondary strengthening phases in EI 893 alloy (see Table 3; Figure 4, b). Partial recrystallization of material proceeds at the same heat treatment stage (see Figure 3, b).

Chromium-based Me_{23}C_6 carbide starts precipitating at 840–925 °C by $\text{MeC} + \gamma \rightarrow \text{Me}_{23}\text{C}_6 + \gamma'$ reaction on grain boundaries, where diffusion and phase transformations, respectively, proceed more readily. This carbide precipitates during multistage ageing on grain boundaries (except for Me_6C , the particle size of which is 0.3–0.5 μm). This carbide is rather unstable and in operation at 550–750 °C, it undergoes transformation on grain boundaries by the reaction of $\text{Me}_{23}\text{C}_6 \rightarrow \text{Me}_6\text{C} \rightarrow \text{Me}_{12}\text{C}$. After formation of the last carbides, their coagulation takes place (up to 1.0–1.5 μm). Temperature of complete dissolution of unstable chromium carbide Me_{23}C_6 is equal to 900–1040 °C.

After heat treatment by the mode of 1160 + 1040 + 900 °C the base structure shows local thickening of grain boundaries with formation of sequences or colonies of Me_{23}C_6 carbide phases of more than 3–5 μm size (see Figure 3, c).

Certain RHT modes (homogenizing and ageing temperatures) can promote formation of various qualitative ratios of structural phases in the matrix solution. Secondary phases of EI 893 alloy usually amount to 1.1–1.3 vol.% and are MeC , Me_{23}C_6 , Me_6C carbides and Me_3B_2 and Me_5B_6 borides, influencing the alloy mechanical properties, particularly distribution morphology. It is obvious that in order to create alloy structure closer to equilibrium one after RHT, it is necessary to ensure formation of stable phases of MeC and Me_6C type based on tungsten and molybdenum, and minimization of chromium carbide phases. The higher the homogenizing temperature, the higher is the temperature of stable phase formation. So, only stable Me_6C and Me_3B_2 phases are found after homogenizing at 1200 °C, which are preserved after long-term operation, irrespective of variants of subsequent heat treatment, that characterizes stable state of EI 893 alloy. Considered three modes of recovery heat treatment of two, three and four stages, eventually lead to formation of significantly different base structures (Figure 4, c, d, f and Figure 5).

So, at two-stage RHT base macrostructure consists, mainly, of equiaxed grains of 2–4 point with thin grain boundaries (Figure 5, a, b). Here, the mi-

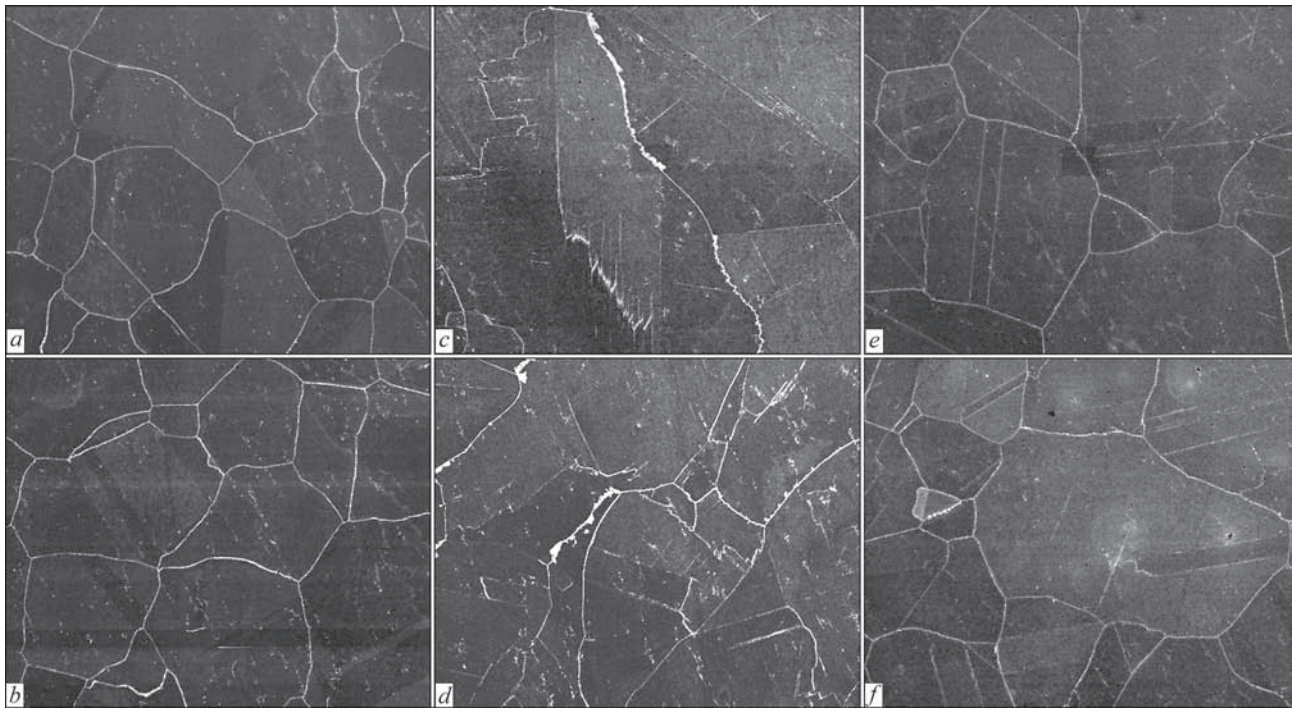


Figure 5. Microstructure ($\times 100$) of EI 893 alloy on sample 2040 after heat treatment at 1040 + 820 (*a, b*), 1160 + 900 + 820 (*c, d*) and 1160 + 1040 + 900 + 820 °C (*e, f*)

Microstructure is a homogeneous solid solution with discrete precipitations of globular carbide phases of Me_6C and MeC type (see Figure 4, *c* and Table 3). Primary stable MeC carbides are most often located inside and on grain boundaries and correspond to complex carbide of II group (W, Mo, Cr)C. At not more than 1 μm grain size and discrete distribution through the grain, particles of this carbide phase have no adverse influence on metal mechanical characteristics.

At three-stage RHT mode (without 1040 °C annealing), material structure clearly demonstrates presence of both grains of different size, and precipitates of a large amount of carbide phases on grain boundaries, slip bands and stacking faults (Figure 5, *c, d*). On the one hand, at heat treatment at 1160 + 900 + 820 °C only Me_{23}C_6 carbide is found in the metal, the discrete particles of which are of 0.3–0.4 μm size, and we could speak about a high level of ductility and impact toughness at 20 °C (exceeding the level after stepped HT). These carbide phases, however, are not an effective obstacle to intergranular slipping. Moreover, these phases also form carbide sequences and clusters (colonies) of more than 5 μm size in the alloy matrix. Coarsening and coalescence of Me_{23}C_6 carbides up to 5 μm in intergranular interlayers, partial fringing of boundaries by γ' -phase particles can have an adverse influence on fracture toughness lowering and can increase the probability of crack initiation. Lowering of impact toughness, notch sensitivity and fatigue properties is related to ductility lowering (see Figure 4, *f* and Table 3).

Standard four-stage RHT mode leads to formation of a structure with different grain size and slip bands, the presence of which can lead later on to microcrack initiation and propagation, and to fracture at fatigue testing (Figure 5, *e, f*). Secondary phases precipitate, mainly, on grain boundaries, and consist of carbides of three types, namely MeC , Me_{23}C_6 , Me_6C (see Table 3 and Figure 4, *d*).

The main strengthening phase of EI 893 alloy is γ' -phase precipitating during prolonged ageing in temperature range of 950 to 550 °C. Its amount depends on ageing temperature and is equal to 9 % at 850, 5 % at 900, 2 % at 950 and 16 % at 650–670 °C (maximum quantity) [9]. Formation of equilibrium γ' -phase proceeds at temperature of 650 °C after ageing for 1000 h. During investigations it was found that RHT application for used blades promoted dissolution of coarsened γ' -phase and subsequent precipitation of regular fine-dispersed strengthening phase. Here, application of two-stage heat treatment promoted precipitation of a larger amount of γ' -phase: 8–10 % (compared to 7–8 % at four-stage RHT) with finer particles of 0.21–0.06 μm (Figure 6).

Hardness, being quite an important characteristic of working blade material, is determined, primarily, by structural state of EI 893 alloy, namely, grain size, quantity and morphology of secondary (most probably) boundary phases, determined by the number of worked hours. Hardness graphs clearly show the structural changes, occurring at different RHT stages (Figure 7, *a, b*). So, during homogenizing at 1160 °C dis-

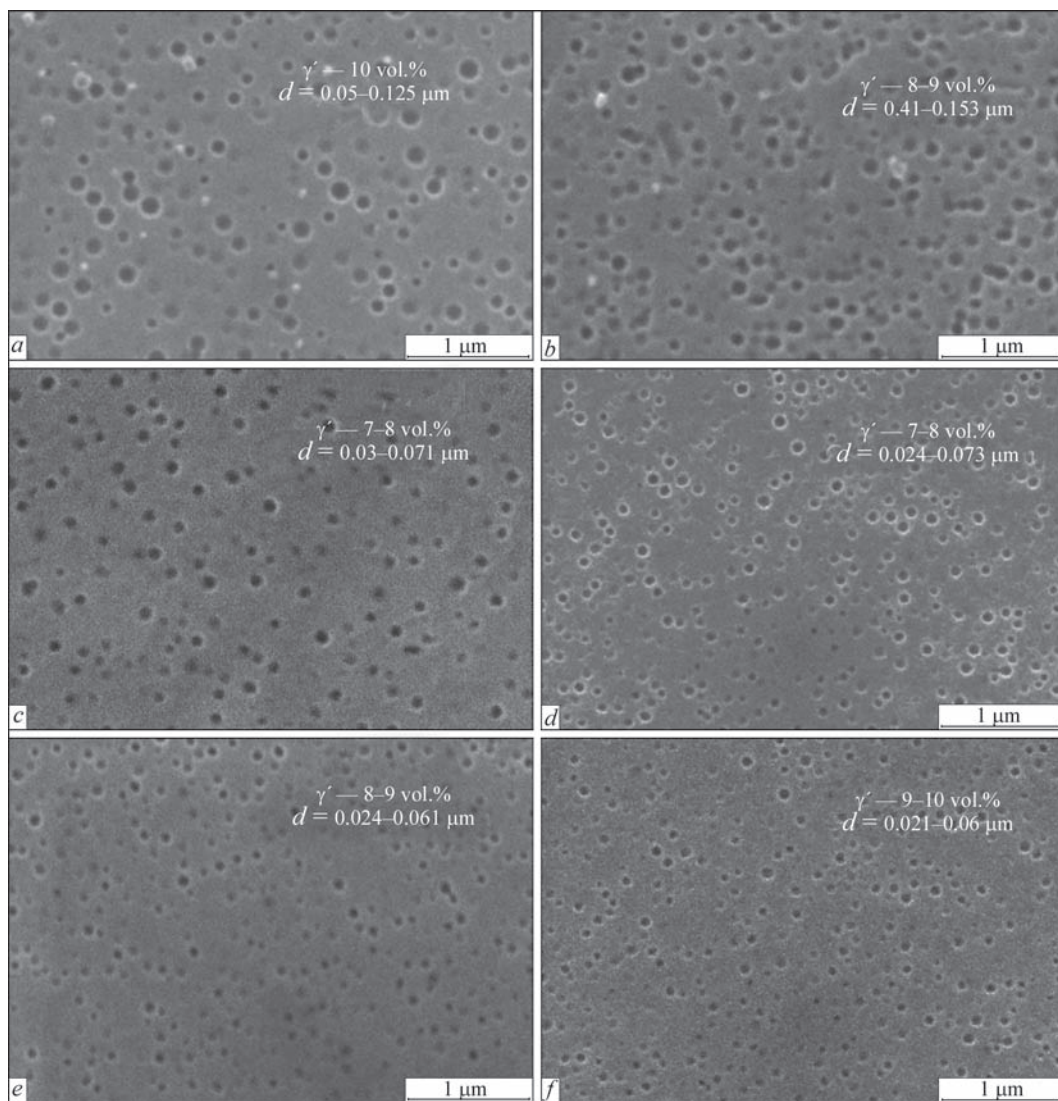


Figure 6. Microstructure of EI 893 alloy after operation (*a, b*), after four- (*c, d*) and two-stage RHT (*e, f*) in blades 0084 (*a, c, e*) and 0103 (*b, d, f*)

solution of the main strengthening γ' -phase and most of the secondary carbide-boride phases (particularly, on grain boundaries) takes place, leading to definite lowering of material hardness. Partial recrystallization of metal (grain refinement), precipitation and stabilization of Me_6C type carbides proceed at subsequent annealing at 1040 °C, leading to increase of material hardness. At subsequent ageing stages, namely at 900 and 820 °C, secondary and main strengthening phases precipitate, which influence material hardness increase.

Graphs of hardness measured at different RHT stages, for each of seven blades studied, are indicative of lowering of its values at high- or low-temperature homogenizing and subsequent increase during ageing. After each of the three RHT modes, blade hardness finally reached the base level of values — 2100–2700 MPa, that confirmed recovery of item material technological properties.

Microhardness, mainly, is the characteristic of grain body strengthening by secondary phases and

main strengthening γ' -phase. Microhardness graphs for all the samples suggest that homogenizing leads to complete dissolution of the strengthening phase and majority of secondary phases in the matrix, while 1040 °C temperature is that of partial dissolution of γ' -phase and complete dissolution of unstable boundary chromium carbides of Me_{23}C_6 type, as well as stabilization temperature of Me_6C carbide, leading to microhardness increase. Subsequent two-stage ageing causes a more complete increase of the amount of γ' -phase and subsequent increase of *HV* values (Figure 7, *c, d*).

Presented graphs and microstructures confirm the correctness of judgments about structural regeneration of the alloy after RHT. So, a certain reduction of difference in grain size (mainly, grain point of 2–4), lowering of ductility and reduction of dimensions of carbide phases in intergranular interlayers, and uniform precipitation of the strengthening phase, are observed. Application of two-stage RHT mode led to absence of

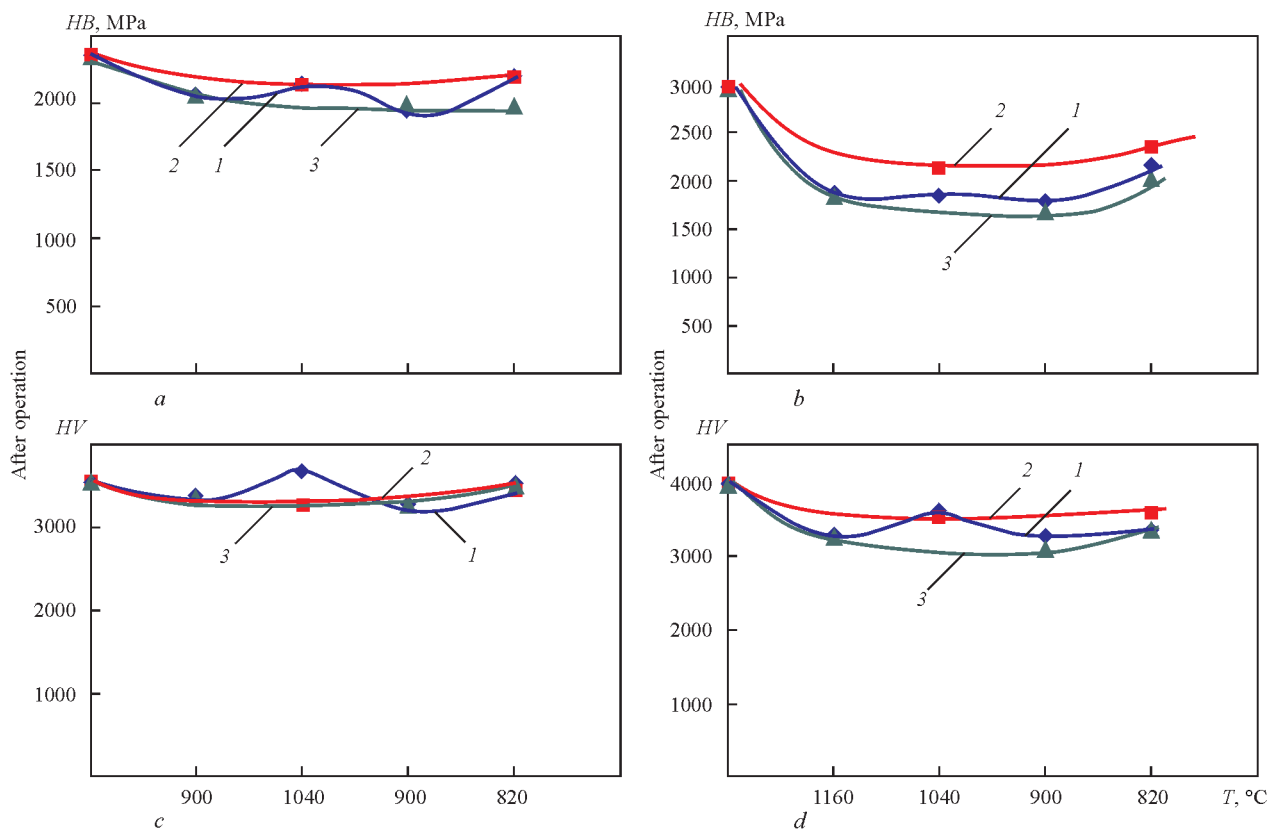


Figure 7. Hardness *HB* (a, d) and microhardness *HV* (c, d) of EI 893 alloy in blades 0103 (a, c) and 0430 (b, d) after different heat treatment stages: 1 — 1160 + 1040 + 900 + 820; 2 — 1040 + 820; 3 — 1160 + 900 + 820 °C

more than 5 μm clusters of Me_{23}C carbides (characteristic for RHT with 900 °C stage) and non-uniformity of distribution and diversity of secondary phases, as in the case of three- and four-stage RHT mode.

So, for instance, for blade 0430 from the set of working blades of GTK 10-4 II stage, the quite high hardness *HB* 2957 of EI 893 alloy after operation decreases to normal level of 2300 MPa as a result of RHT (Figure 7, b).

RHT leads to lowering of base alloy hardness (increase of ductility) due to redistribution of impurities from grain boundaries into matrix solution and reverse dissolution of embrittling phases, precipitated on grain boundaries as a result of interstitial impurity segregation and unfavourable carbide transformations in the alloy in turbine blade operation, as well as partial dissolution of the strengthening γ' -phase.

Selection of heat treatment mode was controlled by performance of mechanical testing of qualification samples, cut out of blade airfoil and root part after long-term operation. Sample testing for uniaxial tension was applied to assess mechanical properties (strength, ductility) of EI 893 alloy after operation and possibility of their improvement after RHT.

Tables 4 and 5 summarize the results of testing samples of MI-9 and MI-12 type (according to PWI specification), cut out of the roots and lower part of airfoil of HPT I stage working blades, after opera-

tion in different regions (including reference-blades 86 and 016 from GTK 10-4 BKF-05 blade set after 57,373 h of operation).

Results of tensile mechanical testing were fully consistent with TU 14-1-2662-79 (or TU 108-02-005) for EI 893 VD alloy. A certain lowering of alloy ductile properties (δ and ψ) was noted at simultaneous increase of hardness *HB*, yield limit $\sigma_{0.2}$ and strength σ_t as a result of operation (see Tables 4 and 5). During RHT performance low-temperature ductility (up to $\delta = 35.6\%$) increased simultaneously with lowering of blade metal strength and hardness. Physico-mechanical properties of EI 893 alloy exceeded those of initial EI 893 VD alloy before mounting the blades in the turbine (according to TU). Obtained results demonstrated the practically complete coincidence of mechanical properties of blade metal after operation and after RHT by the data of testing performed in 2004–2005 and given in the report [9].

Results of tensile testing showed a slight deviation of physico-mechanical properties of metal of blade profile part from those of root metal, in view of different temperature conditions of operation, i.e. higher temperature through the airfoil.

Strength and ductility properties at increased temperature of 750 °C are quite important physico-mechanical characteristics of the alloy for working blades (see Table 5). High-temperature testing was

Table 4. Mechanical properties of metal of GTK 10-4 working blades at 20 °C after operation and RHT in vacuum

Blade number	Analysis location	$\sigma_{0.2}$, MPa	σ_r , MPa	δ , %	ψ , %
After 57,000 h of operation					
86	Root lower tooth	606.2	1073.5	33.2	37
		629.4	1107	36	35.8
	Root middle tooth	629.4	1100	33.6	30.5
		640.2	1111	32.4	30.5
66	Airfoil front part	629	1103	28.2	31
		692	1050	28.5	31.7
After 3-stage RHT					
122	3rd tooth	575	981	36	23.4
		531.7	987.5	41.3	30.5
	2nd tooth	542.6	970	37.5	27.6
		531.7	955	34.8	30.5
123	3rd tooth	543	972	33	30.5
		578.4	1032	40	28.8
	2nd tooth	602.2	1025	37.6	27
		580.3	1011.6	33.8	30
151	3rd tooth	573	1003	31.2	23.8
		547.4	991.7	32.3	32.3
	2nd tooth	616.4	1107	34.8	30.5
		662.3	1096	38.5	35.5
86	3rd tooth	629.4	1076.5	36.7	27
		621.3	1083.4	33.2	26.9
	2nd tooth	629.4	1096	33.3	32.8
		After 2-stage RHT			
86	3rd tooth	543	957	34.7	25.6
		531.7	948.5	36.2	27.6
	2nd tooth	572.6	998	32.4	28.8
		570.8	946.6	27.6	22.6
		562.8	967.8	34.4	23.4
		553.4	944	27.4	23.3
	Airfoil lower part, leading edge, core	499.2	929	31.2	23.4
		566.6	931	35.5	24.6
		514.6	943.8	33.6	22.7
		514.6	935	32	22.8
Requirements to TU 14-1-2662-79		500	850	20	22

performed on MI-9/1k samples (test part diameter of 5 mm, test section length of 25 mm) to PWI specification, cut out of the metal of root upper tooth and from airfoil lower part in its most massive region, adjacent to leading edge.

After RHT, strength level (756.5–780.0 MPa) greatly exceeded the level of 650 MPa specified by the TU for the alloy. It was, however, somewhat lower than the results of testing metal after operation (867 MPa). Ductility of blade metal after RHT was higher than that of blade metal after operation, and was equal to $\delta = 36.8$ – 38.9 and $\psi = 30.1$ – 40.8 %, respectively, compared to 22.2 and 26.9 %. Also noticeable is a certain increase of ultimate strength and ductility exactly after two-stage heat treatment process. RHT ensured increase of fracture energy and elongation, and yield limit and ultimate strength of base alloy EI 893 somewhat decreased, compared to the alloy after long-term operation of the items. Practically 1.5 times higher values of elongation and reduction were obtained, compared to the data after operation

at almost the same strength level. This is indicative of much greater fracture energy of material at tensile testing (area under deformation diagram curve) (Figure 8).

Value of EI 893 VD alloy elongation, equal to 20 % and less at 750 °C, is critical in terms of irreversible lowering of blade metal fracture toughness. Elongation and degree of reduction in cross-sectional area of the stretched sample, preceding fracture, is determined by many factors, in particular, grain size and volume fraction of particles of the main strengthening phase and secondary phase particles, precipitating both in the bulk and on boundaries of grains (see Table 3). True deformation at fracture of high-temperature nickel alloys decreases markedly, with increase of volume content of hard carbide and boride particles, which is exactly what was observed in operation.

Analysis of sample fractures after tensile testing provides the required additional information on EI 893 alloy metal structure, uniformity of phase component distribution, features of their plastic deformation

Table 5. Mechanical properties of metal of GTK 10-4 working blades at 750 °C after operation and RHT in vacuum

Blade number	Analysis location	$\sigma_{0.2}$, MPa	σ_r , MPa	δ , %	ψ , %
After 57,000 h of operation					
86	1st tooth	515.8	870.3	23.6	27.7
16		524.5	864.2	20.8	26
After 3-stage RHT					
151		542	794.3	36.8	45.2
		532.3	786	39.2	48.4
123	1st tooth	460.2	746.3	37.8	39.4
		462	736.8	35.2	42.2
122		439.6	739.3	36.4	39.2
		437.8	736.3	35.4	36.2
After 2-stage RHT					
16	Airfoil lower part, leading edge, core	445	781	41.2	29.2
17		469.6	784.3	37	29.4
19		449.6	784.3	39.5	29.4
20		443	771.3	37.7	32.5
Requirements to TU 14-1-2662-79		N/D	650	11	15

(transcrystalline or intergranular fracture), defects, microporosity, and on obvious stress raisers, leading to premature fracture of material. In high-temperature operation of blades, the developing ageing processes lead to segregation of secondary phases on grain boundaries, resulting in ductility lowering. The shape of inclusion particles, according to the data of [8, 10], influences the ductility, namely, elongated inclusions cause greater embitterment than do the equiaxed ones. At application of external load, inner cavities can form in the alloy matrix, when local stress exceeds the strength of adhesion of the inclusion to the matrix solution, and tearing occurs over the interface, or in the case of fracture of second phase particles proper.

The higher the intensity of strain hardening, the smaller the strain, required for stress increase to the level leading to particles tearing from the matrix. At deforming of multiphase structure with relatively soft matrix, the main deformation occurs in the solid solution. At a certain concentration of hard (brittle) excess carbide phases, the maximum strength is achieved, when these phases are the most refined (uncoagulated), and particles precipitate in the matrix with minimum intervals (interparticle distances) [11, 12]. Thus, operating time and initial chemical composition of metal of a specific blade will determine its real residual fatigue life.

Application of multistage RHT allows reaching uniform distribution of all interstitial impurities in the matrix. Homogenizing temperature above 1160 °C is inadmissible, as the grain will start growing. In such a case, we will not achieve the required uniformity of strengthening phase precipitation in the alloy matrix and material fracture toughness respectively.

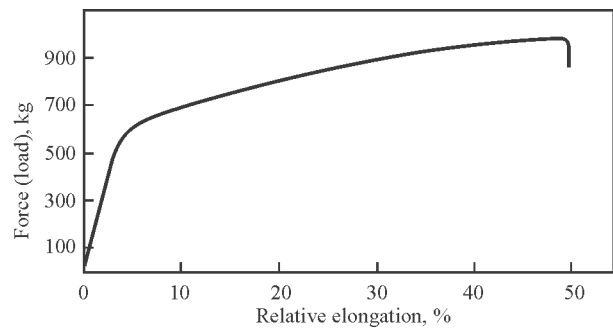
**Figure 8.** Typical diagram of strain hardening of cylindrical samples of EI 893 VD alloy after undetermined operating period and RHT at uniaxial tension at 20 °C with $\epsilon = 1.6 \cdot 10^{-3}$ 1/s, $\sigma_1 = 963.4$ MPa, $\sigma_{0.2} = 514.6$ MPa and $\delta = 45$ %

Figure 9 gives the characteristic microstructures of fracture surface of cylindrical samples of RH-treated EI 893 alloy after testing for uniaxial tension. Analysis of fracture pattern of EI 893 alloy samples from GTK 10-4 working blades after operation and RHT showed that fracture, on the whole, is similar, irrespective of material state: it is ductile fracture, occurring over a plane normal to sample axis [13], without formation of local necking on working surface. On microscopic scale, fracture along the normal is fracture from inner necking or from massive shear along alternating planes inside each separate grain, reaching the intergranular boundary (Figure 10).

In fracture of samples, made from blade material after operation, predominantly intragranular (transcrystalline) fracture is visible (see Figure 9, a, c). Intercrystalline fracture sites are observed simultaneously, which are due to predominant precipitation of carbide phase particles, as a result of natural ageing of EI 893 alloy at long-term operation. Intergranular surface shows pits from carbide particles, precipitating on the boundaries (Figure 9, e). Hard particles are stress raisers and generate sliding dislocation displacement to adjacent grains. This way, running of uniform plastic deformation in polycrystalline sample volume is ensured at the initial loading stage.

RHT technology, promoting homogenizing of blade metal structure and refining of strengthening phase particles, makes plastic deformation more uniform through the entire polycrystal volume, ensuring plastic flow in the regions, directly adjacent to grain boundaries. Fracture appearance and repeated form of stretching diagrams, point to a low intensity of strain hardening (see Figure 8). It follows that considerable deformation should be applied to achieve such a stress level, which will lead to particle tearing from the matrix, and cause formation of discontinuities in polycrystal volume. After RHT ductile fracture mode prevailed in all the samples (see Figure 9). Ductile fracture pits were observed on fractograms of samples, cut out of set blades and subjected to RHT. So, a

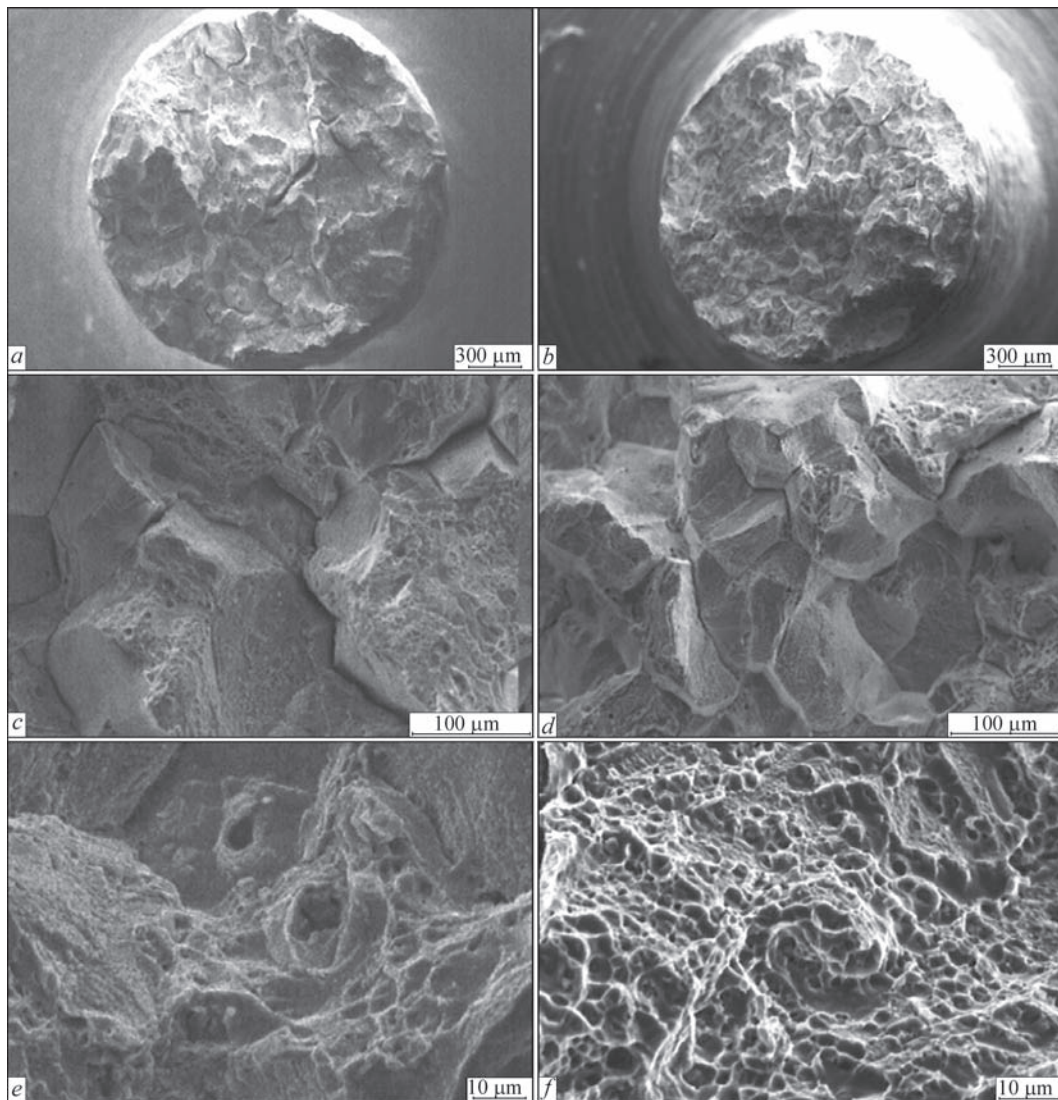


Figure 9. Fracture mode of samples prepared from blade EI 893 alloy after undetermined operating period (*a, c, e*) and RHT (*b, d, f*) sample, cut out of a tooth of GTK 10-4 RL root after RHT, had relative elongation of 33.2 %. It was characterized by practically complete ductile (pit) fracture with minor elements of intergranular fracture. Shear deformation prevailed in the grain bulk (see Figure 9, *d, f*).

As the intensity of strain hardening decreases in nickel alloys with FCC lattice with temperature rise, reduction in area should increase, which we observed in experiments (see Tables 4 and 5). Increase of localized ductility was compensated by a certain lowering of uniform elongation of samples, that is indicative of operational reliability.

Alloys, strengthened, predominantly, through solid solution alloying, should have higher fatigue fracture resistance, owing to increased slip resistance and strain hardening resistance, respectively. Ability to accommodate strain hardening increases fatigue life, owing to increased slip dispersion. It is anticipated that the technology of anticorrosion protection of working blades, using surface plastic deformation

of coatings on blades, will provide increased fatigue fracture resistance. Thus, EI 893 alloy, at preservation of chemical composition, is little prone to fatigue fracture compared to high-temperature alloys, as large fracture energy is required for sample fracture.

In the case of wrought alloys, strengthening γ' -phase is structurally unstable. Particularly, at increased temperature of 700–750 °C (blade airfoil) and availability of temperature gradient along blade airfoil, non-uniformity of its distribution and non-uniformity of particle size are observed. This may cause stress concentration in the blade in operation and lowering of metal endurance. In this respect, there is the risk of formation of «pure» zones near the crystallite boundaries, associated with carbide phase precipitation on the boundaries. Deformation bands form in such precipitation-free near-boundary regions, which may lead to microcrack initiation and fatigue fracture.

Inclusions and microvoids have a strong influence on metal fatigue resistance. Coarse MeC or Me₆C carbide particles, forming on crystallite boundaries after

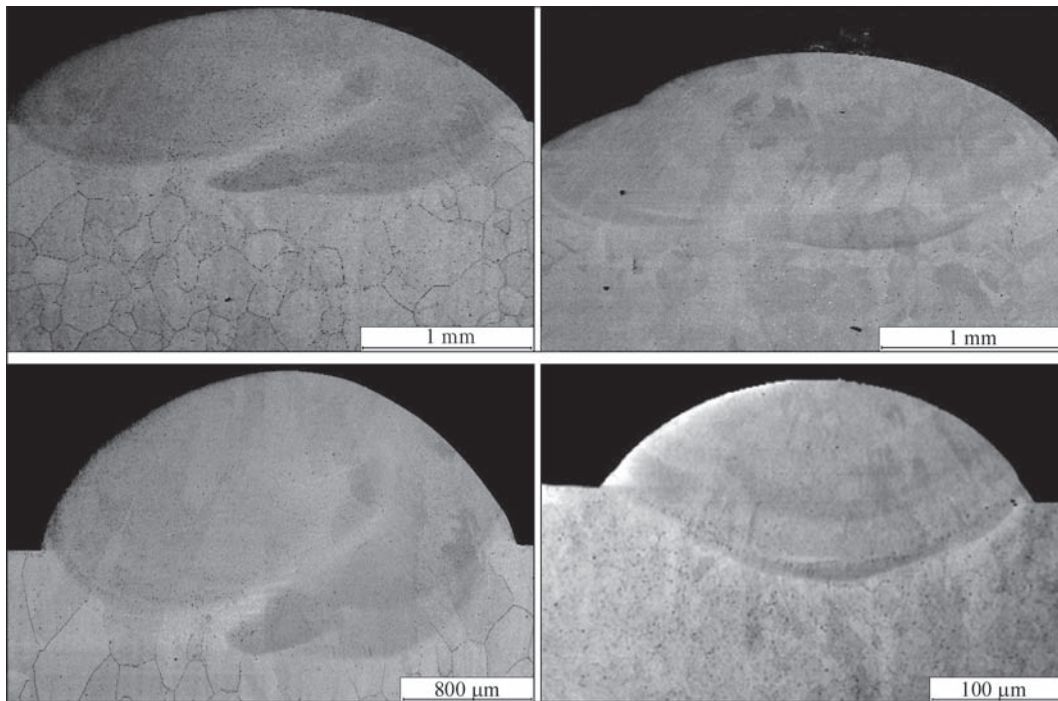


Figure 10. Microstructure of welds deposited on upper tips of airfoil of different working blades from EI 893 alloy with IN-625 welding wire after two-stage RHT

more than 50,000 h of operation, lower the fatigue life, while non-metallic inclusions or faceted pores can be the site of fatigue fracture initiation, in view of the difference of their and matrix solution moduli of elasticity. Fatigue at operating temperature is largely similar to fracture at creep, which makes a significant contribution into total deformation on grain boundaries. Pores on grain boundaries and wedge cracks become fatigue fracture sites. At increased temperature, oriented slipping along certain crystallographic planes is inhibited and replaced by intergranular fracture.

Evolution of initial alloy microstructure proceeds during long-term high-temperature testing. Thermally activated microstructural changes in a certain way influence the time characteristics of long-term strength, particularly at exposure to corroding medium, which the products of fuel combustion are.

Different level of fatigue life — fatigue and creep resistance — can be achieved, depending on the size of γ' -phase particles in EI 893 VD alloy, associated with deviations of matrix composition and heat treatment type. So, at optimizing of the size of strengthening γ' -phase particles by selection of the mode of high-temperature ageing (RHT), creep deformation of polycrystalline material can be reduced, thus increasing its fatigue resistance [7, 10]. Long-term strength and creep limit are design characteristics of structural strength of GTU working blades.

At blade operation in the turbine, the impact of aggressive gas flow at high temperature can result in depletion of the surface layer of the part, particularly,

in the airfoil upper part, in titanium, aluminium and chromium, and oxide particles of aluminium and titanium can form in it. Data of testing working blades for structural endurance, obtained by authors of [14], showed that lowering of alloying element content in surface layer of EI 893 alloy blades of 30 to 100 μm depth does not have any significant influence on endurance limit value. Fatigue resistance level with 50 % fracture probability in new parts, and in blades with dealloyed zone depth of 30 μm , corresponding to 25,000–32,000 h of operation in the turbine, is approximately the same and equal to $\sigma_{-1} = 150$ MPa. Sensitivity to presence of dealloyed zone is manifested only in the region of stresses, exceeding endurance limit ($\sigma_{\text{max}} = 200$ MPa), when number of cycles to fracture was equal to $N_f = 1.7 \cdot 10^6$, compared to base experimental value of $3.2 \cdot 10^6$ cycles [14]. Thus, if lowering of structural endurance limit of blades after prolonged operation is observed, the cause for this phenomenon should be attributed to presence of surface defects (nicks, dents, undercuts), causing stress concentration in blade airfoil critical sections. The authors of [15] also showed that defects of mechanical origin and variation of edges rounding-off radius have a significant role in fatigue crack initiation in parts operation in the turbine.

It follows from the above said that recovery of alloy structure, preservation of part geometry and sound preparation of blade surface ensure operational reliability of the item. As was shown, structure optimization is achieved at two-stage RHT mode. High-tem-

perature ageing at 1040 °C is designed for structure stabilization, namely, dissolution of present irregular coagulated γ' -phase in grain center and on the boundaries; dissolution of unstable chromium carbides (and clusters) of Me_{23}C_6 type, formed in long-term operation, and partial dissolution and refinement of quite stable MeC and Me_6C carbides (up to 0.5–1.0 μm) on grain boundaries and their uniform distribution. Low-temperature ageing at 820 °C leads to regular precipitation of the main strain-hardening γ' -phase of 0.07–0.12 μm size with 9–11 % bulk density.

Building-up of upper tip of GTK 10-4 working blades was performed by argon-arc surfacing with IN-625 wire of the following composition, wt. %: Ni–21.5Cr–9Mo–3.6Nb–1Co–0.4Al–0.4Ti–0.5Si–0.5Mn–0.1C. Surfacing with application of this filler material was performed on samples, cut out of seven working blades after different operating periods. Samples were built-up in as-delivered condition without pre-homogenizing, which was followed by two-stage heat treatment.

Analysis of sample structure after all the stages of RHT showed that repaired sections had no defects of any kind, namely solidification cracks, pores, lacks-of-penetration, etc. (see Figure 10). This was the result of correct selection of low-alloyed filler material for welding solid solution strengthening nickel alloy. Deposit metal was dense and was characterized by cellular-dendritic structure with discrete dispersed precipitations of strengthening carbide phases on individual crystallite boundaries.

Weld structure clearly shows the boundary of transition from fusion line to base EI 893 metal. Difference in composition of IN-625 welding wire and blade alloy promoted redistribution on the fusion line of base and filler components (Nb, W, Mo, Ti, etc.) in solidified metal.

HAZ, the depth of which was equal to about 500 μm , did not contain any cracks, boundary eutectics or pores. Microhardness of base alloy was equal to $H_{\mu} = 2350\text{--}2700$ MPa, as a result of precipitation of the main and redistribution of secondary strengthening phases. As weld metal is matrix γ -solid solution, weakly strengthened by dispersed carbide phases, its microhardness was equal to approximately 2515 MPa, and in the HAZ microhardness increased to 2800 MPa. Therefore, microhardness of different zones of all the deposited welds was close in value and ensured the serviceability of reconditioned blade sections.

Proceeding from the results of present and earlier research of numerous GTK 10-4 working blades made from EI 893 alloy, we can say that these items are little prone to fatigue fracture at standard oper-

ating conditions of all the turbine components. So, fracture of blades of GTK 10-4 set, which has operated for 78,000 h (Berdichev, Ukraine) occurred for a number of reasons, namely unsatisfactory preparation of part edges, corrosion-fatigue impact of fuel combustion products, irreversible overageing of base alloy, and impact of foreign bodies [16]. As no intermediate RHT was performed for this set, blade metal was characterized by irreversible overageing, which in the presence of increased stress raisers and mechanical impact led to rapid destruction of items. Microstructure of EI 893 metal of blades, being in an overaged state and not having sufficient resistance to crack propagation (as a result of lowering of fracture energy), was the material science cause of accelerated fatigue fracture (endurance lowering) of blades in thermophysical and gas-dynamic studies of modified combustion chamber.

Therefore, RHT performance is required after first 45,000–55,000 h of operation. Above 65,000–70,000 h irreversible structural changes occur in EI 893 alloy at operational ageing, leading to lowering of ductility and fracture toughness. Recovery of initial structure and mechanical characteristics of metal of working blades with different operating time, after RHT performance can guarantee them an additional operating life of 20,000–24,000 h.

Conclusions

A procedure was developed for determination of repairability of GTK 10-4 HPT and LPT set working blades after different operating periods, including visual inspection, geometry control, penetrant inspection, metallographic macro- and microanalyses, chemical and phase analysis of base alloy EI 893. It is established that an essential change of structural-phase state of base material takes place during prolonged operation (operational ageing at 630–670 °C) of working blades, made of EI 893 alloy, determining the change of its mechanical properties, compared to metal in the initial state, namely increase of ultimate strength, yield point, hardness and lowering of ductility properties.

Comprehensive metallographic studies were conducted on optimization of the modes of RHT of GTK 10-4 HPT and LPT working blades. It is established that two-stage RHT ensures structural regeneration of EI 893 base alloy after operation (45,000–55,000 h). Data of mechanical testing at room and working temperature and data on hardness and microhardness confirmed recovery of base properties and their full compliance with EI 893 VD alloy TU: after RHT performance blade metal hardness and ultimate strength

somewhat decrease and ductility rises (to $\delta \approx 33.2\text{--}35.6\%$) that exceeds the properties of initial EI 893 VD alloy before mounting the blades in the turbine.

Selected two-stage RHT mode did not have any adverse impact on formation of dense sound welds at reconditioning the working blade airfoil tip, using IN-625 filler material.

Reversibility of structural changes of working blade metal at correspondence of chemical composition to nominal composition of EI 893 alloy guarantees an additional operating life of 20,000–24,000 h to them after RHT performance, owing to correspondence of structure and mechanical properties of reconditioned blade metal to its initial state.

1. Verin, A.D., Sims, C.T., Hagel, W.C. (1976) Microstructure and properties of heat-resistant alloys. In: *Heat-resistant alloys*. 207–241. Moscow: Metallurgiya.
2. Getsov, L.B. (1996) *Materials and strength of gas turbine parts*. Moscow: Nadra.
3. Majner, R.V. (1995) *Fatigue. Superalloys II. Heat-resistant materials for aerospace and industrial power plants*, Vol. 1, 336–372. Moscow: Metallurgiya.
4. Nemajzer, Yu.A., Gursky, G.L., Dobina, N.I. et al. (1982) Influence of grain size on structural fatigue strength of blades from KhN65VMTYu (EI 893) alloy. *Energomashinostroenie*, **5**, 18–21.
5. Pigrova, G.D., Kabanov, B.S., Sedov, V.M. (2002) Method of physico-chemical phase analysis for evaluation of structural state of heat-resistant materials in life prediction. *Trudy NPO TsKTI*, Issue 289, 39–47.
6. Shajdak, B.P., Ivanov, S.A., Ivanov, A.V. et al. (2002) Prolongation of service life of blades of drive gas turbine units. Service life and reliability of materials and welded joints of power plants. *Ibid.*, 191–204.
7. Berdnik, O.B., Tsaryova, I.N., Razov, E.N. (2011) Development of technology for prolongation of life of KhN65VMTYu alloy turbine blades. *Vestnik SamarGAKU*, **27(3)**, 240–246.
8. Pigrova, G.D. (2006) Diagnostics of structural changes in metal of GTU parts during operation by the method of phase physico-chemical analysis. *Trudy NPO TsKTI*, Issue 295, 55–64.
9. (2005) *Development of procedure for prolongation of the life of GTK 10-4 GPU (HPT) 1st stage blades and specifying the life of repaired BKF-05 set*: Report of RC Pratt & Whitney Paton. Kiev.
10. Rybnikov, A.I., Kryukov, I.I. (2006) Carbide transformations in intergranular interlayers of heat-resistant nickel-base alloys during ageing and long-term operation. *Trudy NPO TsKTI*, Issue 295, 154–163.
11. Rybnikov, A.I., Shajdak, B.P., Ivanov, S.A. (2006) Influence of structural factor on structural fatigue strength of blades of stationary GTU. *Ibid.*, 79–90.
12. Getsov, L.B. (2010) *Materials and strength of gas turbine parts*, Vol. 1. Rybinsk: Gasoturb. Technologii.
13. Fridman, Ya.B. (1974) *Mechanical properties of metals*, Vol. 2. Moscow: Mashinostroenie.
14. Sorokin, V.G., Guzanov, B.N., Kositsyn, S.V. et al. (1980) Study of EI 893 alloy blades after long-term operation in gas turbine unit. *Energomashinostroenie*, **3**, 25, 26, 29.
15. (2000) *Instructions on investigation of causes of blading fracture of gas turbine units in gas-pumping units*. Moscow: Gazprom, VNIIGAZ.
16. (2005) *Analysis of causes of spontaneous fracture of GTK 10-4 unit HPT 1st stage blades, CS Berdichev (after 78,000 h of operation)*: Report of RC Pratt & Whitney Paton. Kiev.

Received 30.12.2015

INFLUENCE OF ELECTRIC-MAGNETIC COMPOSITE FIELD ON WC PARTICLES DISTRIBUTION IN LASER MELT INJECTION*

LIANG WANG^{1,2}, YONG HU^{1,2}, SHIYING SONG^{1,2} and JIANHUA YAO^{1,2}

¹Research Center of Laser Processing Technology and Engineering, Zhejiang University of Technology
18 Chaowang Str., 310014, Hangzhou, PRC. E-mail: ddtwl@foxmail.com

²Zhejiang Provincial Collaborative Innovation Center of High-end Laser Manufacturing Equipment
Hangzhou, PRC

The laser melt injection (LMI) method is always used to prepare a metal-matrix composite layer on the surface of substrate. In LMI process, the laser beam melts the surface layer of substrate locally while simultaneously injecting particles of additional material. In order to control the distribution of reinforcement particles in LMI layer, an electric-magnetic composite field can be applied. The effect of electric-magnetic synergistic on the reinforcement particles distribution in LMI was investigated using experimental and numerical method. The spherical WC particles were used because their regular shape was most close to the simulation conditions and good tracer performance in the melt flow. The distribution of WC particles in longitudinal section was observed by SEM and calculated by computer graphics processing. The trajectory of WC particles in the melt pool was simulated by a 2D model coupled the equations of heat transfer, fluid dynamics, drag force, Lorentz force and phase transition. The simulation results were compared with experimental data and were in good agreement. The results indicated that the effect of electric-magnetic synergistic on the reinforcement particles distribution was verified. The distribution of WC particles in LMI-layer was influenced by the direction of Lorentz force induced by electric-magnetic composite field. When the Lorentz force and gravity force are in the same direction, the vast majority of particles are trapped in the upper region of LMI-layer, and when these forces are in the opposite direction, most particles are concentrated in the lower region. 34 Ref., 8 Figures.

Keywords: *laser melt injection, WC particles, Lorentz force, particles distribution, electric-magnetic composite field*

Metal-matrix composites (MMC) reinforced with ceramic particles exhibit a number of advantages over monolithic alloys and have been used extensively in industry [1]. The laser melt injection (LMI) method is always used to prepare a MMC layer on the surface of substrate with low particle dissolution rate, high surface performance and low cracking tendency [2–5]. LMI has been mainly applied for improving the surface hardness and wear resistance of the metallic substrate, such as stainless steels [4, 6], aluminum alloys [7, 8], titanium alloys [1, 2, 9–11], low carbon steels [12–16] and tool steels [3, 5, 17]. In contrast with laser cladding, the reinforcement particles (usually ceramics) injected in the molten pool without any other metal-matrix powder and moved with the melt flow preserve solid state or micromelt state due to rapid solidification during LMI process [7].

Graded materials can be designed at microstructural level to tailor specific materials for their functional performance in particular applications [18, 19].

The controlled gradients in mechanical properties offer attractive challenges for the design of surfaces with resistance to contact deformation and damage [9]. In order to optimize the particle utilization ratio, machinable property and gradient distribution performance of LMI-layers, it is necessary to control the distribution of reinforcement particles. The previous LMI process usually chose the special designed lateral nozzle as a powder delivery nozzle for avoiding the excessive dissolution of reinforcement particles [16]. Therefore, the injection angle with respect to the surface normal [20], relative position between the powder spot and laser spot [21] and powder injection velocity [7, 22] are the key process parameters during powder injection, which influence the distribution status of reinforcement particles sensitively. Consequently, it is difficult and time-consuming to adjust the distribution of reinforcement particles because the processing parameters window of LMI using lateral nozzle powder delivery system is very narrow [6, 7].

*Based on materials presented at Seventh International Conference «Laser technologies in welding and materials processing», September 14–18, 2015, Odessa, Ukraine.

In this research, a common coaxial nozzle was chosen to replace the special designed lateral nozzle to simplify the adjusting process of powder delivery system. However, both the injection angle with respect to the surface normal and the relative position between the powder spot and laser spot are fixed during coaxial LMI process. In order to control the distribution of WC particles using coaxial nozzle, an external force was introduced during LMI process, which applies an electric-magnetic composite field (EMCF) to the melt pool.

The application of electromagnetic field is a positive practice in laser welding and laser alloying to influence the distribution of added elements. Effect of electromagnetic stirring on the element distribution in laser welding was investigated by numerical and experimental methods. It was shown that the change of distribution of the filler material results from modulation of the melt flow due to periodic induced electromagnetic volume forces [23]. The frequency is a main parameter to determine the spatial distribution of elements, whereas the magnetic flux density is the main parameter determining the overall scale of the magnetic manipulation [24, 25].

A numerical model is built to investigate the laser-melted aluminum pool under the influence of static magnetic field. The solute distribution in the solid depends on the applied magnetic induction [26]. The other effects of electromagnetic field include suppressing surface undulation of laser remelting, damping the velocity of molten pool [27], reducing the defects of laser welding [28, 29], preventing gravity dropout of the melt during laser full-penetration welding [30 et al.].

The previous investigations in electromagnetic fields were mostly focused on the influences of the elements, temperature, velocity and defects distribution on the melt pool during laser processing, all of which are induced through AC magnetic field or melt flow in the steady magnetic field. In this work, both

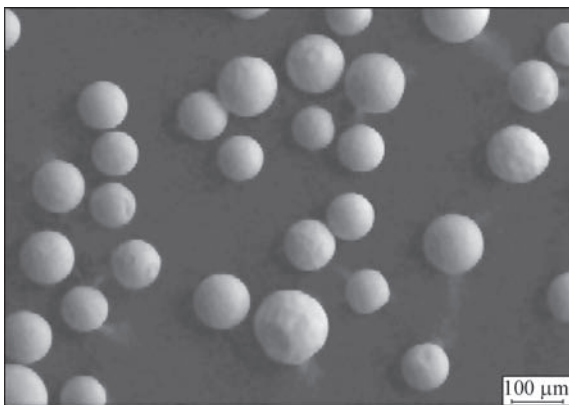


Figure 1. SEM-image of spherical monocrystalline WC particles used

the external steady electric field and the steady magnetic field were added in the molten pool during LMI process synchronously. The Lorentz force, generated by the electric-magnetic synergistic effect, is a kind of directional volume force in the melt pool in LMI, similar to gravity. This Lorentz force can function as an additional volume force acting on the melt flow with variable direction. Consequently, the positions of WC particles trapped in the molten pool will be changed without changing LMI parameters.

In this research, a 2D transient multi-physics numerical model, concerning heat transfer, fluid dynamics, phase transition, drag force acted on the particles and electromagnetic field, was employed to study the distribution mechanism of reinforcement particles during LMI under the EMCF. The partial differential equations were solved with the finite-element solver COMSOL Multiphysics. The simulation results were verified by experimental measurements.

Experimental methods. AISI 316L austenitic stainless steel was used as the substrate because of its paramagnetic property. The chemical composition of AISI 316L was as follows, wt. %: 0.02C, 0.55Si, 1.55Mn, 0.03P, 0.03S, 10Ni, 16.5Cr, 2.08Mo, Fe — base. Spherical monocrystalline WC particles (without W_2C) were chosen as the reinforcement particles, because the particles of this shape were used in the simulation study due to their good tracing performance in the melt flow. The size of WC particles was 75–150 μm (Figure 1). The substrate specimens were machined to long strips with dimensions of 200×20×10 mm. Figure 2 shows the schematic diagram of the LMI process with EMCF applied. The electromagnets were used to provide the steady magnetic field (maximum magnetic flux density is 2 T), and large-capacity lead-acid batteries (2 V, 500 A·h) were used to provide high current (steady electric field) for the melt pool. In the melt pool zone, the magnetic flux density was of about 0.4–2.0 T, and the average current density — of about 5 A/mm².

LMI was conducted using the 2 kW diode laser LASERLINE, powder feeder and coaxial nozzle. Argon was used as a shielding gas to reduce oxidation of the specimen and WC particles. Laser beam diam-

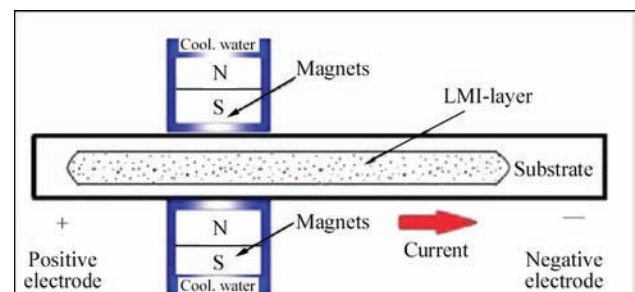


Figure 2. Schematic of LMI process with EMCF

eter, optimized laser power, scanning speed and powder feed rate in this experiment were 4 mm, 1.6 kW, 5 mm/s and 10 g/min, respectively. The distribution of WC particles and elements in the melt pool were observed using SEM (Carl Zeiss SIGMA HV-01-043) and EDS (Bruker Nano X-Flash Detector 5010). The gradient distribution of microhardness HV was test by the microhardness tester (Shimadzu HMV-FA2).

Numerical simulation. Governing equations. The numerical simulation of the LMI process involves a classical computational fluid dynamics approach, that concerns fluid flow field and pressure as well as temperature. The movement of injected particles was calculated by the Lagrangian approach with fluid–particle coupling [18, 19]. The influence of Lorentz force induced by EMCF was added in the source term of momentum equations as the volume force. The computational domain was initially composed of 30×5 mm rectangle. The surrounding gas phase was not taken into account because of the large differences in density and dynamic viscosity between the liquid metal and gas phase. The basic assumptions, made on the fluid flow, temperature field, particles injection and electromagnetic field in the simulation, were as follows:

- laminar flow pattern is assumed. The main reason for this choice is that the velocities outside the shear layers at the surfaces are significantly reduced, and the Reynolds number inside the molten pool turn out to be far less than turbulent critical value (10^3) [30]. Furthermore, laminar flow assumption makes the numerical solution easier and reduces the computational effort [31];

- material properties are temperature-dependent up to evaporation temperature;

- Joule heat induced by high current is neglected due to short action time and strong laser heating of the metal up to evaporation temperature;

- buoyancy of molten pool is determined using Boissinesq approximation, because density variation caused by the temperature difference is sufficiently small;

- thermal conductivity is adjusted properly according to the actual situation, since the convective motion in the transverse plane (z -direction) is neglected in 2D models, that may result in heat redistribution due to the fluid flow [32];

- distribution of magnetic flux density in the active area is uniform;

- injection direction of particles is perpendicular to the substrate of molten pool, and particles are spherical and uniformly distributed in the powder jet;

- in the LMI process, the injecting particles maintain non-melting state, and their shape is spherical regularly. Therefore, the drag force (Stoke’s force)

acting on the particles is only related to the velocity of melt flow [7];

- heat and convection in the molten pool are not influenced by the injection of particles;

- effect of gravity and drag exerted by the surrounding gas on particle movement are negligible, and all particles have the same velocity.

The governing equations for mass conservation, energy conservation, momentum conservation including Darcy force and Lorentz force are solved using the finite-element package COMSOL Multiphysics.

Mass conservation is expressed as

$$\nabla(\rho u) = 0, \tag{1}$$

and momentum conservation is given as

$$\rho \frac{\partial u}{\partial t} + \rho(u \nabla)u = \nabla[-pI + \eta(\nabla u + (\nabla u)^T)] + F_{\text{Buoyancy}} + F_{\text{Darcy}} + F_{\text{Lorentz}}, \tag{2}$$

where ρ is the density; p is the pressure; η is the viscosity; F_{Buoyancy} , F_{Darcy} and F_{Lorentz} are the source terms, represent the buoyancy force, Darcy force, and Lorentz force, respectively. The buoyancy force comes from density gradients, which is related to the expansion of the liquid metal and is usually expressed using the Boissinesq approximation as follows:

$$F_{\text{Buoyancy}} = \rho(1 - \beta(T - T_m))g, \tag{3}$$

where β is the thermal expansion coefficient; g is the gravitational constant; T is the temperature; and T_m is the melting point.

The role of Darcy term is to dampen the velocity at the phase interface, therefore it becomes the velocity of solidified phase after transition. This term is assumed to vary with the liquid fraction and can be expressed according to the Kozeny–Carman equation [33] as

$$F_{\text{Darcy}} = -A_{\text{mush}} \frac{(1 - f_1)^2}{f_1^3 + c} u, \tag{4}$$

where F_1 is the volume fraction of the liquid phase, A_{mush} and c are the arbitrary constants (A_{mush} should be a large-valued constant accounting for damping the velocity of the mushy region, and c is the small constant to avoid division by zero in the solid region).

The liquid fraction f_1 is assumed to vary linearly with temperature in the mushy zone, which is delimited by the solidus T_s and liquidus T_L temperatures. It is defined as

$$f_L = \begin{cases} 0 & T < T_s, \\ \frac{T - T_s}{T_L - T_s} & T_s \leq T \leq T_L, \\ 1 & T > T_L. \end{cases} \tag{5}$$

The Lorentz force F_{Lorentz} induced by the external steady magnetic field, steady electric field and conductive fluid motion is described by the following equation:

$$\begin{aligned} F_{\text{Lorentz}} &= jB = \sigma(E + uB) \times \\ &\times B = \sigma(EB + uB^2), \end{aligned} \quad (6)$$

where j is the current density; B is the magnetic flux intensity; E is the external electric field; and σ is the electric conductivity.

The interaction of external magnetic field with external electric field builds up the directional Lorentz force contribution ($\sigma(EB)$). Simultaneously, the movement of conducting melt flow in the external magnetic field generates the induced electric current. This induced current in the same external magnetic field forms the nondirectional Lorentz force ($\sigma(\mu B^2)$), which has a component directed against the original melt velocity thus decelerating the melt.

Energy conservation is given as

$$\rho C_p \frac{\partial T}{\partial t} + \rho C_p u \nabla T = \nabla(k \nabla T) + Q_{\text{source}}, \quad (7)$$

where C_p is the heat capacity; k is the thermal conductivity; and Q_{source} is the heat source from laser beam.

The movement of particles in the molten pool obeys Newton's second law:

$$\frac{d(m_p v)}{dt} = F_D + F_g + F_{\text{Buoyancy}}; \quad (8)$$

$$F_D = m_p \left(\frac{1}{\tau_p} \right) (u - v); \quad (9)$$

$$F_g = m_p g; \quad (10)$$

$$F_{\text{Buoyancy}} = V_p \rho_f g, \quad (11)$$

where m_p is the particle mass; F_D is the drag force; F_g is the gravity; u is the fluid velocity; v is the particle velocity; g is gravity acceleration; V_p is the volume of one particle; and ρ_f is the fluid density.

The relative Reynolds number is $Re_r = 1-100$, and the drag coefficient based on Schiller–Naumann drag mode is calculated as follows:

$$Re_r = \frac{\rho_f |u - v| d_p}{\mu}; \quad (12)$$

$$C_D = \frac{24}{Re_r} (1 + 0.15 Re_r^{0.637}); \quad (13)$$

$$\tau_p = \frac{4 \rho_p d_p^2}{3 \mu C_D Re_r}; \quad (14)$$

where d_p is the diameter of particle; μ is the dynamic viscosity; and ρ_p is the particle density.

Boundary conditions. The temperature of the substrate is assumed to be the same as ambient temperature T_0 initially. The energy distribution of laser beam is considered uniform because of the nature of diode laser. Surface tension is added on the top surface as the boundary condition, which is relevant to the surface temperature of molten pool. In this model, surface tension is expressed by Marangoni shear stresses using the test function of the computation software:

$$-\eta \frac{\partial u}{\partial z} = \frac{\partial \gamma}{\partial T} \frac{\partial T}{\partial x}, \quad -\eta \frac{\partial v}{\partial z} = \frac{\partial \gamma}{\partial T} \frac{\partial T}{\partial y}, \quad (15)$$

where η is the viscosity; $\partial \gamma / \partial T$ is the temperature derivative of the surface tension.

The injection velocity of the WC particles is calculated as follows [34]:

$$u = \frac{3D^2 v_0^2 \cos \theta}{32\nu R}, \quad (16)$$

where D is the nozzle hydraulic diameter; v_0 is the carrier gas velocity at the nozzle; ν is the kinematic viscosity; θ is divergence angle of particle; and R is the distance between nozzle and sample. The particle injection velocity was calculated about 1.1 m/s and powder spot center was coincided with laser spot center.

Boundary conditions of numerical model are illustrated in Figure 3. The necessary velocity and heat boundary conditions were as follows:

- top boundary: $-\eta u_{i,k} = \frac{\partial \gamma}{\partial T} \frac{\partial T}{\partial x_i}$ ($i=1, 2; k=3$); $q_0 = h(T_{\text{ext}} - T)$;
- left boundary: $u \mathbf{n} = 0$; $q_0 = h(T_{\text{ext}} - T)$;
- bottom boundary: $u \mathbf{n} = 0$; $-\mathbf{n}(-k \nabla T) = 0$;
- right boundary: $u \mathbf{n} = 0$; $q_0 = h(T_{\text{ext}} - T)$.

The melting temperature of material was 1700 K; fluid density 7800 kg·m⁻³; particles density 15600 kg·m⁻³; heat capacity 746 J·kg⁻¹·K⁻¹; latent heat of fusion 30 J·kg⁻¹; heat conductivity 30 W·m⁻¹·K⁻¹; dynamic viscosity 0.006 Pa·s; surface tension coeffi-

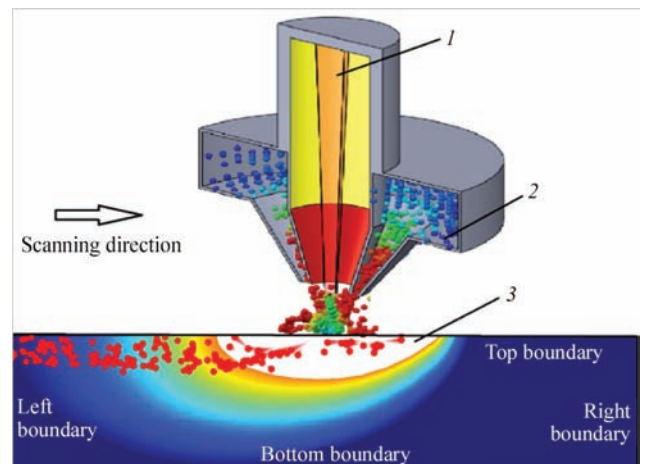


Figure 3. Boundary conditions of numerical model: 1 — laser beam; 2 — particles; 3 — molten pool

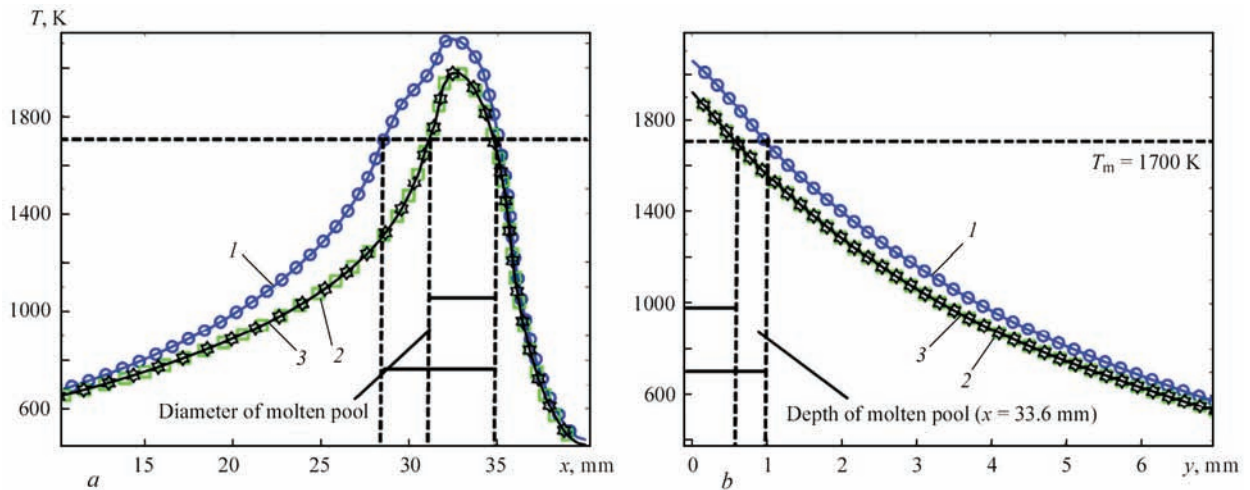


Figure 4. Temperature distribution along the surface (a) and along the depth (b) of molten pool: 1 — $B = 0$; 2 — 0.6 ; 3 — 1.2 T

cient $-0.52 \cdot 10^{-4} \text{ N} \cdot \text{m}^{-1} \cdot \text{K}^{-1}$; diameter of particles was $80 \text{ }\mu\text{m}$. The processing parameters were as follows: diameter of laser spot of 4 mm ; laser scanning speed of $4 \text{ mm} \cdot \text{s}^{-1}$; laser power of 1700 W ; powder feed rate of $15 \text{ g} \cdot \text{min}^{-1}$; shielding gas flow rate of $10 \text{ l} \cdot \text{min}^{-1}$.

Results and discussion. *Temperature and velocity distribution.* The temperature distribution along the surface of molten pool (x -direction, $y = 0 \text{ mm}$) is plotted in Figure 4, a, and along its depth at the center of laser spot (y -direction, $x = 33.6 \text{ mm}$) — in Figure 4, b. It is seen that the high temperature zone of the molten pool with Lorentz force are suppressed. No matter the Lorentz force is upward or downward, the temperature distribution with EMCF is always lower than that without it. In contrast with temperature distribution, the fluid velocity distribution is influenced by EMCF more significantly. Figure 5, a shows the velocity distribution along the surface, and Figure 5, b — the depth of molten pool. The maximum fluid velocity of molten pool is about 0.08 mm/s without EMCF. With the influence of the directional Lorentz force induced by EMCF, the maximum fluid velocity

of molten pool is decreased to less than 0.02 mm/s , whether the direction of Lorentz force is upward or downward. The double peaks of velocity distribution depict the difference in maximum velocity because of the heat accumulation effect and Marangoni effect during laser remelting process. On each side of the peak temperature location, thermal gradients are of opposite sign, leading to fluid flow velocity equal to zero at that point due to Marangoni effect. The thermal gradients become maximal at the edge of laser beam, that explains the velocity peaks observed [32].

Particles distribution. Figure 6, a, b shows the longitudinal sections of the LMI-layers with particle distribution prepared with different directions of Lorentz force induced by EMCF. Figure 6, c shows the longitudinal section of the LMI-layer prepared without external Lorentz force. Due to the same LMI process parameters conducted, the thickness of the LMI-layers and the fraction of injected particles in the LMI-layer are almost the same for the three specimens. In order to investigate the quantitative difference of particles between the three distributions, all the LMI-layers were divided into two regions (upper

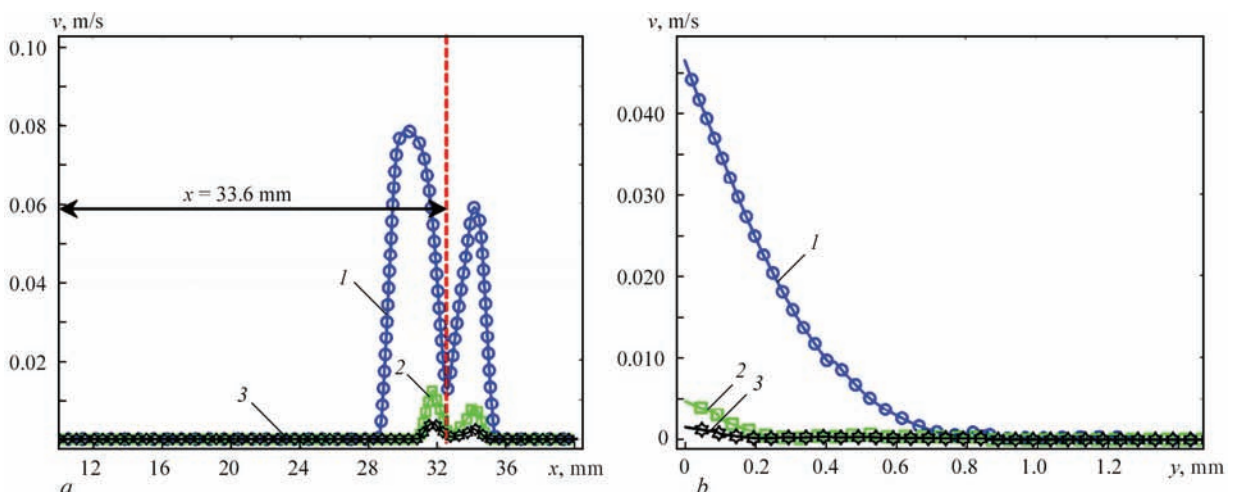


Figure 5. Velocity distribution along the surface (a) and along the depth (b) of molten pool: 1 — $B = 0$; 2 — 0.6 ; 3 — 1.2 T

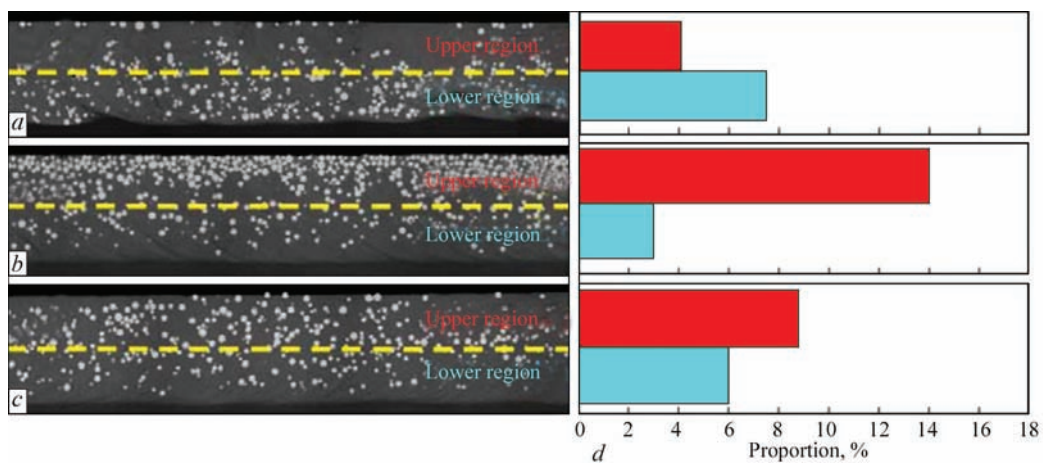


Figure 6. Distributions of WC particles in the longitudinal sections of LMI-layers at upward (a) and downward (b) direction of Lorentz force and without (c) external Lorentz force, and proportion of WC particles in upper and lower regions (d)

and lower) equally. The proportions of WC particles in both regions were computed via computer graphics processing. The calculating results are attached to the corresponding LMI-layers in Figure 6, d.

Under the upward Lorentz force, most particles are concentrated in the lower region. The proportion in the lower region is more than 50 % of that in the upper region. Only a small number of WC particles were trapped in the near-surface of LMI-layer. Contrarily, the majority of particles are trapped in the upper region when the direction of Lorentz force is downward (see Figure 6, b). The particles could hardly be sunken into the lower region of molten pool. The particles are distributed uniformly in the LMI-layer produced without EMCF applied (see Figure 6, c). The Lorentz force generated by the steady magnetic and electric field is a kind of directional steady volume force in the melt pool. The direction of the Lorentz force acting on the fluid is in the opposite direction of the corresponding force acting on the particles. Taking into consideration equations (1) and (2).

$$F_v = (jB)V, \tag{17}$$

where V is the volume of fluid displaced by one particle, and

$$F_L = -L_p, \tag{18}$$

where L_p is the counteracting Lorentz force acting on the particle. Because the WC particles are non-conducting and non-magnetic, the Lorentz force does not act on the particle directly.

Diagram of the forces acting on one particle and surrounding fluid is shown in Figure 7. When the Lorentz force acting on the fluid is assumed as upward, the following balance equation is established to express the force (in y-direction) acting on the particle:

$$-F_{iy} = F_B - L_p + F_{dy} - G_p \tag{19}$$

where F_{iy} , F_{dy} and G_p are the inertia force, drag force and gravity, respectively. F_B , F_{dy} and G_p are assumed to be constant, thus, F_{iy} and L_p are positively proportional.

Consequently, when the direction of Lorentz force acting on the fluid is upward the sinking velocity of the particle will be increased, during the continuous powder injecting process the particles are easier sunk into the lower region of the melt pool, and the particles will be trapped in the upper region when the direction of Lorentz force acting on the fluid is downward.

The exact trapped positions of particles are described by the simulation model. The particle distributions in the longitudinal sections of the LMI-layers are shown in Figure 8, a, b. The dots represent the injected particles, the orientation of tails indicates the motion direction of particles, and the length of tails indicates the magnitude of motion velocity of particles. With the same LMI process parameters, the number of injected particles, depth of melt pool and solidification duration are all the same. During the continuous LMI process, the particles are homogeneously distributed in the melt pool (see Figure 8, b). Sinking velocity of particles is damped with the effect of downward Lorentz force (see Figure 8, a).

Within the same solidification time, the particles injected into the melt pool can hardly be sunken to the bottom of melt pool before its solidification, and they

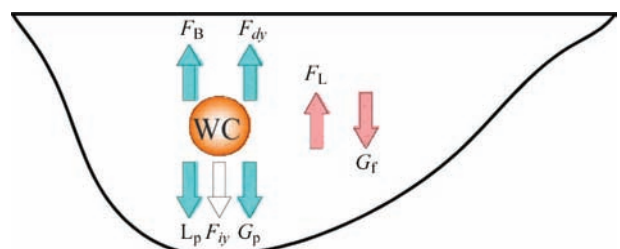


Figure 7. Diagram of forces acting on the particle and surrounding fluid

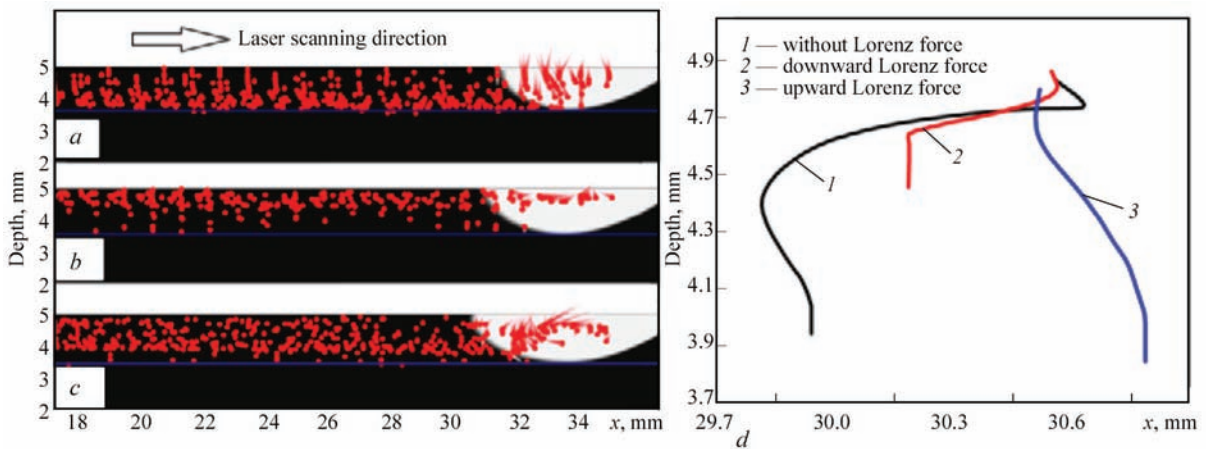


Figure 8. Simulated trapped position of particles in LMI-layer with upward (a) and downward (b) Lorentz force and without it (c), and sinking trajectories of injected particles (d)

are concentrated in the upper region of melt pool. In fact, the particles in the melt pool are not sunken along the straight line. The sinking trajectories were calculated by the simulation model (Figure 8, d). (Note that the sinking trajectories are different for the particles in different injected positions, the particles shown in Figure 8, c are taken from the central zone of the laser spot.). When the particles penetrate the surface of the melt pool, they are transmitted along with the fluid motion due to the strong Marangoni convection at the surface. The resulted sinking trajectories of particles become different mainly because of the electric-magnetic synergistic effect. The resultant buoyancy acting on the particles is increased with the downward Lorentz force. As a result, the sinking depth of the particles is reduced more obviously. Meanwhile the particles near the surface of the melt pool are influenced more by the Marangoni convection, and they are easier dragged to the edge of the melt pool, where it is prone to solidify.

Equation (18) is obtained from (16) through expanding the forces F_B and L_p . The equivalent gravity acceleration is assumed to be the synthesis of local gravity acceleration and Lorentz force related to the density of fluid. According to the above equations, when the Lorentz force and gravity force are in the same direction, the particles in the melt pool are just in hypergravity state, while when the Lorentz force and gravity force are in the opposite direction, the particles in the melt pool can be regarded in hypogravity state. In summary, the direction of the Lorentz force can be easily adjusted by changing the directions of electric and magnetic fields, thus to control the movement of the reinforcement particles in LMI process:

$$\left(g - \frac{jB}{\rho_f} \right) \rho_f V + F_{dy} - G_p + F_{iy} = 0, \quad (20)$$

where g is the local acceleration of gravity.

Conclusions

The electric-magnetic synergistic effect on the reinforcement particle distribution in LMI was studied experimentally and using simulation. The Lorentz force induced by EMCF can change the gradient distribution of WC particles. Their distributions in the LMI-layers were influenced by EMCF without adjusting the original LMI parameters. When the Lorentz force and gravity force are in the same direction, the majority of particles are trapped in the upper region, while when the Lorentz force and gravity force are in the opposite direction, most particles are concentrated in the lower region. With the assistance of EMCF the sinking velocity and trajectory of WC particles were changed due to the additional volume force acted on the fluid of melt pool during LMI process.

Acknowledgements. *The authors are grateful for financial supports from the National Natural Science Foundation of China (51475429). The authors also would like to specially appreciate Prof. Rong Liu from Carleton University for her kind help in article modification.*

1. Liu, D., Chen, Y., Li, L. et al. (2008) In situ investigation of fracture behavior in monocrystalline WCp-reinforced Ti-6Al-4V metal matrix composites produced by laser melt injection. *Scripta Materialia*, **59**, 91–94.
2. Li, L., Liu, D., Chen, Y. et al. (2009) Electron microscopy study of reaction layers between single-crystal WC particle and Ti-6Al-4V after laser melt injection. *Acta Materialia*, **57**, 3606–3614.
3. Verezub, O., Kálazi, Z., Sytcheva, A. et al. (2011) Performance of a cutting tool made of steel matrix surface nano-composite produced by in situ laser melt injection technology. *J. Materials Proc. Techn.*, **211**, 750–758.
4. Do Nascimento, A.M., Ocelík, V., Ierardi, M.C.F. et al. (2008) Wear resistance of WCp/duplex stainless steel metal matrix composite layers prepared by laser melt injection. *Surface and Coatings Techn.*, **202**, 4758–4765.

5. Cabeza, M., Castro, G., Merino, P. et al. (2014) A study of laser melt injection of TiN particles to repair maraging tool steels. *Surface and Interface Analysis*, **46**, 861–864.
6. Do Nascimento, A.M., Ocelík, V., Ierardi, M.C.F. et al. (2008) Microstructure of reaction zone in WCp/duplex stainless steels matrix composites processing by laser melt injection. *Surface and Coatings Techn.*, **202**, 2113–2120.
7. Vreeling, J.A., Ocelík, V., Pei, Y.T. et al. (2000) Laser melt injection in aluminum alloys: On the role of the oxide skin. *Acta Materialia*, **48**, 4225–4233.
8. Li, F.Q., Li, L.Q., Chen, Y.B. (2013) Arc enhanced laser melt injection of WC particles on Al surface. *Surface Eng.*, **29**, 296–299.
9. Pei, Y.T., Ocelik, V., de Hosson, J.T.M. (2002) SiCp/Ti6Al4V functionally graded materials produced by laser melt injection. *Acta Materialia*, **50**, 2035–2051.
10. Vreeling, J.A., Ocelík, V., de Hosson, J.T.M. (2002) Ti–6Al–4V strengthened by laser melt injection of WCp particles. *Ibid.*, **50**, 4913–4924.
11. Chen, Y., Liu, D., Li, F. et al. (2008) WCp/Ti–6Al–4V graded metal matrix composites layer produced by laser melt injection. *Surface and Coatings Techn.*, **202**, 4780–4787.
12. Liu, A., Guo, M., Hu, H. (2009) Improved wear resistance of low carbon steel with plasma melt injection of WC particles. *J. Materials Eng. and Performance*, **19**, 848–851.
13. Liu, A., Guo, M., Hu, H. et al. (2008) Microstructure of Cr₃C₂-reinforced surface metal matrix composite produced by gas tungsten arc melt injection. *Scripta Materialia*, **59**, 231–234.
14. Guo, M., Liu, A., Zhao, M. et al. (2008) Microstructure and wear resistance of low carbon steel surface strengthened by plasma melt injection of SiC particles. *Surface and Coatings Techn.*, **202**, 4041–4046.
15. Liu, A., Guo, M., Zhao, M. et al. (2007) Microstructures and wear resistance of large WC particles reinforced surface metal matrix composites produced by plasma melt injection. *Ibid.*, **201**, 7978–7982.
16. Liu, D., Li, L., Li, F. et al. (2008) WCp/Fe metal matrix composites produced by laser melt injection. *Ibid.*, **202**, 1771–1777.
17. Verezub, O., Kálazi, Z., Buza, G. et al. (2009) In-situ synthesis of a carbide reinforced steel matrix surface nanocomposite by laser melt injection technology and subsequent heat treatment. *Ibid.*, **203**, 3049–3057.
18. Guo, B., Fletcher, D.F., Langrish, T.A.G. (2004) Simulation of the agglomeration in a spray using Lagrangian particle tracking. *Appl. Math. Modelling*, **28**, 273–290.
19. Minier, J.-P. (2015) On Lagrangian stochastic methods for turbulent polydisperse two-phase reactive flows. *Progress in Energy and Combustion Sci.*, **50**, 1–62.
20. Chen, Y., Liu, D., Li, L. et al. (2009) Microstructure evolution of single crystal WCp reinforced Ti–6Al–4V metal matrix composites produced at different cooling rates. *J. Alloys and Comp.*, **484**, 108–112.
21. Kloosterman, A.B., Kooi, B.J., de Hosson, J.T.M. (1998) Electron microscopy of reaction layers between SiC and Ti–6Al–4V after laser embedding. *Acta Materialia*, **46**, 6205–6217.
22. Anandkumar, R., Almeida, A., Vilar, R. et al. (2009) Influence of powder particle injection velocity on the microstructure of Al–12Si/SiCp coatings produced by laser cladding. *Surface and Coatings Techn.*, **204**, 285–290.
23. Gatzen, M., Tang, Z., Vollertsen, F. (2011) Effect of electromagnetic stirring on the element distribution in laser beam welding of aluminium with filler wire. *Physics Procedia*, **12**, 56–65.
24. Tang, Z., Gatzen, M. (2010) Influence on the dilution by laser welding of aluminum with magnetic stirring. *Ibid.*, **5**, 125–137.
25. Gatzen, M. (2012) Influence of low-frequency magnetic fields during laser beam welding of aluminium with filler wire. *Ibid.*, **39**, 59–66.
26. Velde, O., Gritzki, R., Grundmann, R. (2001) Numerical investigations of Lorentz force influenced Marangoni convection relevant to aluminum surface alloying. *Int. J. Heat and Mass Transfer*, **44**, 2751–2762.
27. Bachmann, M., Avilov, V., Gumenyuk, A. et al. (2013) About the influence of a steady magnetic field on weld pool dynamics in partial penetration high power laser beam welding of thick aluminium parts. *Ibid.*, **60**, 309–321.
28. Schneider, A., Avilov, V., Gumenyuk, A. (2013) Laser beam welding of aluminum alloys under the influence of an electromagnetic field. *Physics Procedia*, **41**, 4–11.
29. Zhou, J., Tsai, H.-L. (2007) Effects of electromagnetic force on melt flow and porosity prevention in pulsed laser keyhole welding. *Int. J. Heat and Mass Transfer*, **50**, 2217–2235.
30. Bachmann, M., Avilov, V., Gumenyuk, A. et al. (2012) Numerical simulation of full-penetration laser beam welding of thick aluminium plates with inductive support. *J. Physics D: Appl. Physics*, **45**, 035201.
31. Akbari, M., Saedodin, S., Toghraie, D. et al. (2014) Experimental and numerical investigation of temperature distribution and melt pool geometry during pulsed laser welding of Ti6Al4V alloy. *Optics & Laser Techn.*, **59**, 52–59.
32. Morville, S., Carin, M., Peyre, P. et al. (2012) 2D longitudinal modeling of heat transfer and fluid flow during multilayered direct laser metal deposition process. *J. Laser Appl.*, **24**, 032008.
33. Brent, A.D., Voller, V.R., Reid, K.J. (1988) Enthalpy-porosity technique for modeling convection-diffusion phase change: Application to the melting of a pure metal. *Numerical Heat Transfer. Pt B: Fundamentals*, **13**, 297–318.
34. Fu, Y., Lored, A., Martin, B. et al. (2002) A theoretical model for laser and powder particles interaction during laser cladding. *J. Materials Proc. Techn.*, **128**, 106–112.

Received 08.12.2015

MODELLING OF RESIDUAL STRESSES, RADIATION SWELLING AND STRESSED STATE OF IN-SERVICE WWER-1000 REACTOR BAFFLE

O.V. MAKHNENKO, I.V. MIRZOV and V.B. POROKHONKO

E.O. Paton Electric Welding Institute, NASU

11 Kazimir Malevich Str., 03680, Kiev, Ukraine. E-mail: office@paton.kiev.ua

The question of effect of baffle residual welding stresses on radiation swelling value has appeared in course of works on life extension of WWER-1000 reactor internals at the second power generating unit of the South-Ukrainian NPP. The E.O. Paton Electric Welding Institute has developed and realized a mathematical model for determination of residual stress-strain state of WWER-1000 reactor baffle in electroslag welding with further heat treatment as well as a model for calculation of baffle radiation swelling taking into account radiation creep. It can be stated based on the results of mathematical modelling that the baffle stressed state after 60 years of operation, calculated taking into account residual welding stresses, is close to the results received using the model without welding. This work studies relaxation of residual welding stresses in the WWER-1000 baffle under effect of irradiation and works out their in-service value-to-time dependence. 15 Ref., 3 Tables, 11 Figures.

Keywords: WWER-1000, baffle, electroslag welding, residual welding stresses, heat treatment, radiation swelling, radiation creep, mathematical modelling

WWER-1000 reactor internals include the baffle made from 08Kh18N10T steel and subjected to in-service porosity accumulation resulting in irreversible increase of material volume. This effect is termed radiation swelling and can result in significant change of structure stressed state in operation.

According to technical documents for the second power unit of the South-Ukrainian NPP, WWER-1000 reactor baffle of V-338 series was manufactured using electroslag welding (ESW) (Figure 1). The welded joints require consideration of effect of residual welding stresses (RWS) on change of the stress-strain state (SSS) of in-service baffle. Therefore, today it is relevant to study RWS in the baffle taking into account

radiation swelling, that is interesting from point of view of design-basis justification of the internals life.

Work [1] experimentally determines insignificant reduction of the RWS in the specimens irradiated with 0.3–1.0 dpa doses at 300 °C temperature. The same work studies the baffle welded joint irradiated to the level of 20–30 dpa for 60 years taking into account structure service stresses. The similar investigation was carried out in [2] for WWER-1000 core.

The aim of the present work is development of the mathematical model for SSS determination in zone of baffle welded joints taking into account their heat treatment, calculation of baffle radiation swelling considering RWS and analysis of stressed state of

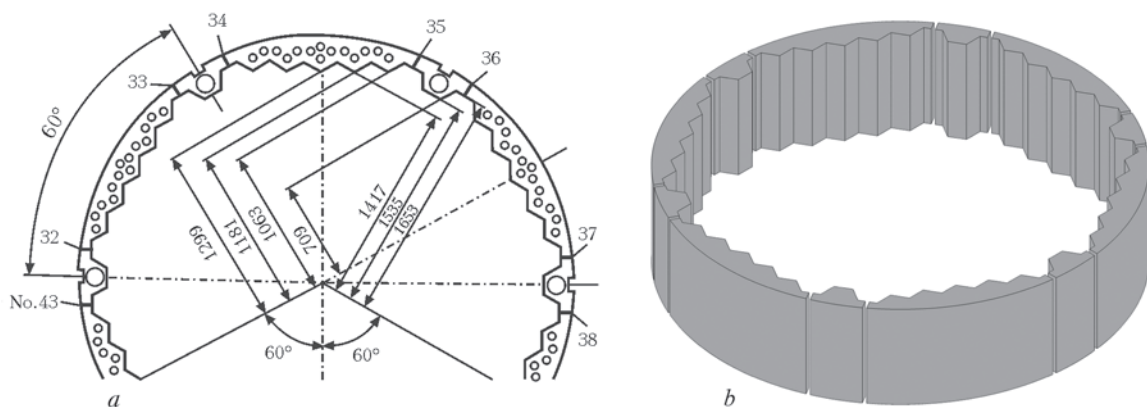


Figure 1. Baffle central ring: *a* — drawing of section from part passport with location of welds Nos 32–38–43; *b* — segments of baffle ring before ESW

Table 1. Main parameters of consumable-nozzle ESW of WWER-1000 baffle

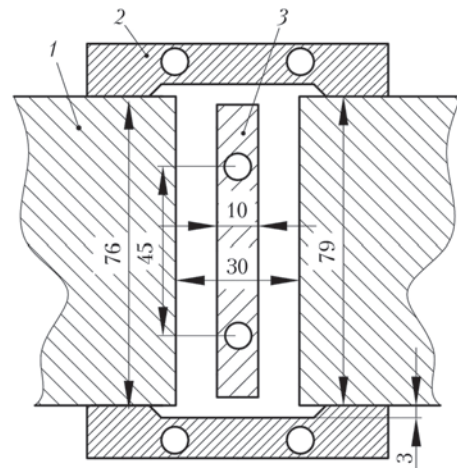
Parameter	Value
Welding current I_a , A	600
Voltage U_w , V	46
Electrode feed rate $v_{e,f}$, m/h	230
Welding speed v_w , mm/s	0.42
Depth of liquid metal pool, mm	40
Temperature of liquid metal pool T_{max} , °C	2000
Nozzle thickness, mm	10
Wire diameter, mm	3
Amount of main/reserved electrode wires, pcs	2/2
Flux	48-OF-6
Electrode wire grade [7]	Sv-04Kh19N11M3
Heat efficiency of process η	0.85

baffle welded joints after irradiation in course of 60 years of operation.

Baffle welding using electroslag technology. Baffle rings are welded from forged segments with the help of ESW [3–5]. Appearance of baffle ring welded elements is shown in Figure 1, *b*. Thickness of the metal in place of welding makes 76–79 mm (Figure 2), weld length is 814 mm.

The special documents [4] state that ESW schemes using wire electrode and consumable nozzle (Figure 3) are mainly used for assemblies and structures of NPP of 70–100 mm thickness.

As applicable to baffle ring manufacture, the safest from process point of view and the most relevant from point of view of welded joint quality is consumable nozzle ESW scheme (Figure 3, *b*). Welding is carried out per one pass on special stands with rigid fixation of welded part.


Figure 2. Parameters of part assembly for ESW: 1 — parts to be welded; 2 — water-cooled forming plate (mold); 3 — nozzle

The welding gap is set taking into account shrinkage deformations. It makes 28 mm in the joint lower part and 30 mm is the upper one [6]. The consumable nozzle is made from the same steel grade that in the base metal. The nozzle includes the channels for main and reserved wires (Sv-04Kh19N11M3 wire is used) [7]. The technology provides for a starting block and run-on plates which are mechanically removed after welding. The main parameters of baffle ESW with consumable nozzle are given in Table 1. Welding power source can be evaluated: $P = IU\eta = 600 \cdot 46 \cdot 0.85 \approx 23$ kW.

ESW joints are subjected to heat treatment on modes determined for the base metal.

Development of mathematical models. The E.O. Paton Electric Welding Institute developed and realized the mathematical model of baffle ESW with further heat treatment. The results of RWS calculation using this model made a basis for calculations of baffle radiation swelling, made using the model of CRI of Structural Materials «Prometey», St.-Petersburg [7, 8]. Also data on volumetric heat generation and

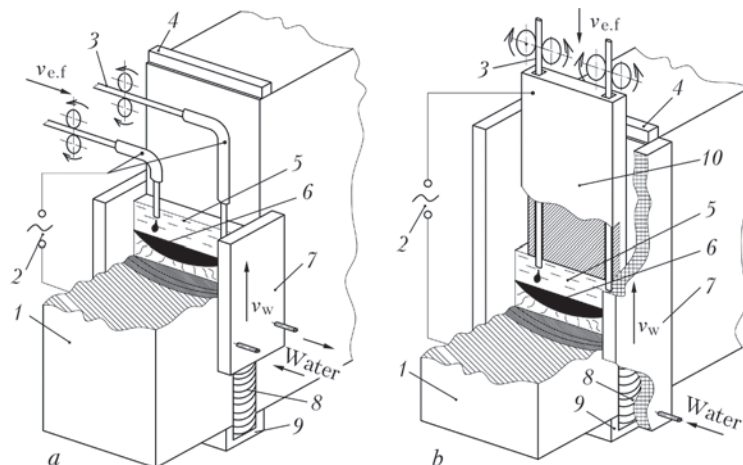

Figure 3. ESW schemes using wire electrodes (*a*) and consumable nozzle (*b*): 1 — parts being welded; 2 — power source; 3 — welding wire; 4 — run-on plate; 5 — slag pool; 6 — metal pool; 7 — water-cooled forming plate (mold); 8 — weld; 9 — starting block; 10 — nozzle

Table 2. Chemical composition of internals base and weld metal, wt.%

Material	δ-ferrite	C	Cr	Ni	Mn	Si	Ti	S	P	Mo	V
Base metal	2–3	0.06	17.89	9.06	1.17	0.31	0.6	0.010	0.009		
Weld metal	4.4	0.07	17.50	10.33	2.40	0.22		0.006	0.025	2.36	0.62

damaging dose rate in the baffle, obtained at Institute for Nuclear Research of the NAS of Ukraine [9] and DB «Gidropress», Podolsk, RF [10] were used in calculations.

Modelling of ESW. Baffle material is austenite steel 08Kh18N10T. Chemical composition of steel and internals welded assemblies in the initial (non-irradiated) state is taken from [7, 11] and given in Table 2.

As can be seen from Table 2, chemical composition of the welded joint has insignificant difference from that of the base metal, therefore, it is assumed that the baffle is uniform and all its volume has 08Kh18N10T steel properties. Dependence of steel yield strength on temperature taken from different sources is given in Figure 4. 3D finite-element model of baffle being welded is given in Figure 5.

Thickness of one layer of numerical elements in weld zone makes $h = 8.14$ mm and baffle height division contains 100 layers. The ESW modeling problem is referred to a moving boundary problem. Molten metal front edge is moved up on the part. Time dt , during which the front edge is shifted to height h of one numerical element, makes

$$dt = \frac{h}{v} = \frac{8.14}{0.42} \approx 19 \text{ s.}$$

The speed of ESW dV/dt can be evaluated on volume of metal being melted. Weld pool area makes $S = 30 \cdot 77.5 = 2323 \text{ mm}^2$. Volume of the metal melted in dt time equals $dV = Sh \approx 18.9 \text{ cm}^3$. Then $dV/dt \approx 1 \text{ cm}^3/\text{s}$. Amount of energy dQ , necessary for heating of $dV = 18.9 \text{ cm}^3$ of metal from $T_{\min} = 20 \text{ }^\circ\text{C}$ to $T_{\max} = 2000 \text{ }^\circ\text{C}$, is also evaluated:

$$dQ = dm(c\Delta T_1 + L + c\Delta T_2), \quad (1)$$

where c is the specific mass heat capacity of metal, J/(kg·K); dm is the material dV volume mass; ΔT_1 is the temperature range from $20 \text{ }^\circ\text{C}$ to melting temperature $T_{\text{liq}} = 1450 \text{ }^\circ\text{C}$; L is the specific mass melting heat, J/kg; ΔT_2 is the temperature range from T_{liq} to T_{\max} .

It is more convenient to transfer to volumetric heat capacity and melting heat:

$$dQ = dV(cp\Delta T_1 + L\rho + c_p\rho\Delta T_2) = dV(c_p\Delta T_1 + L_p + c_p\Delta T_2), \quad (2)$$

where ρ is the average density of steel in the whole temperature range; $c_p = cp$ is the specific volumetric heat capacity of metal, J/(m³·K); $L_p = L\rho$ is the specific volumetric melting heat, J/m³.

At $T \in [T_{\min}; T_{\text{liq}}] \bar{\rho} = 7575 \text{ kg/m}^3$.
Then

$$c = 462 \text{ J/(kg}\cdot\text{K)} \rightarrow c_p = 462 \cdot 7575 = 3.5 \cdot 10^6 \text{ J/(m}^3\cdot\text{K)} = 3.5 \text{ J/(cm}^3\cdot\text{K)}$$

$$L = 277 \text{ kJ/kg} \rightarrow L_p = 277 \cdot 10^3 \cdot 7575 = 2.1 \cdot 10^9 \text{ J/m}^3 = 2100 \text{ J/cm}^3$$

$$dQ = 3.5 \cdot 18.9(1450 - 20) + 2100 \cdot 18.9 + 3.5 \cdot 18.9(200 - 1450) \approx 171 \text{ kJ.}$$

Power consumed in welding makes $P = dQ/dt = 171/19 = 9 \text{ kW}$.

Given evaluations show that parameters of ESW mode provide sufficient power for baffle heating (60 %) and weld metal melting (40 %).

Time increment τ for solving temperature problem is determined from relationship

$$\tau < \frac{c_p h^2}{2\lambda}, \quad (3)$$

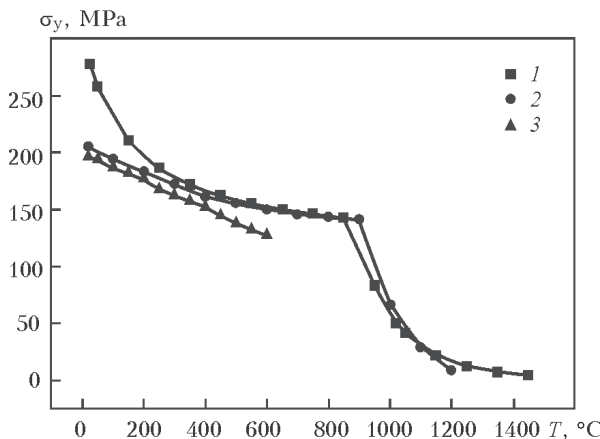


Figure 4. Yield strength of 08Kh18N10T steel versus temperature: 1 — JmatPro program calculation; 2 — Nejmark [12]; 3 — PNAE [13]

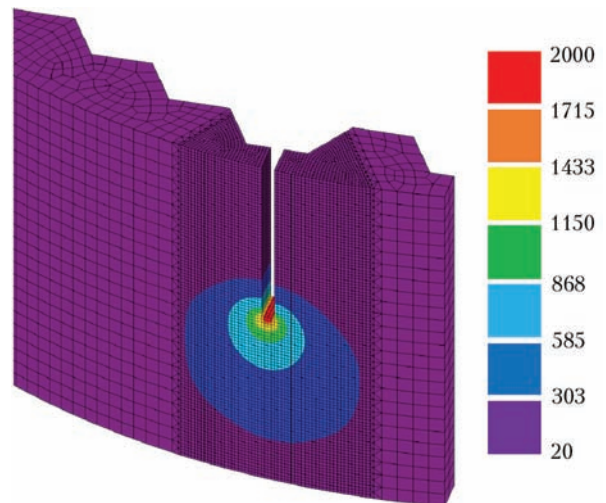


Figure 5. Numerical mesh, temperature (°C) and penetration zone in 3D model of ESW

where $h = 0.814$ cm is the thickness of numerical element (discrete layer of molten metal for time dt); $\lambda = \lambda(T)$ is the heat conduction; $\lambda|_{T=20} = 1.6$ W/(m·K) = 0.166 W/(cm·K); $\lambda|_{T=1000} = 30$ W/(m·K) = 0.3 W/(cm·K);

$$\tau|_{T=20} > \tau|_{T=1000} < \frac{3.5 \cdot 0.814^2}{2 \cdot 0.3} \approx 3.9 \text{ s.}$$

Thus, time step dt should be divided for $[dt/\tau] = 5$ increments or more for convergence of temperature problem solution. The increment can exceed τ for mechanical problem.

Heat treatment modelling. Critical welded structures of the elements of NPP equipment are subjected to mandatory heat treatment, which allows reducing the level of RWS. Thus, WWER-1000 baffle after welding is subjected to heat treatment on high-temperature tempering mode at 650 °C. Rise of temperature reduces the material yield strength, and RWS are relaxed due to instantaneous plasticity effect. Effect of material creep, which takes place at indicated temperature, has even more influence on RWS relaxation.

Creep strain rate $\dot{\varepsilon}_{\text{eq}}^{\text{cr}} = A\sigma_{\text{eq}}^n$ is related with the stress intensity σ_{eq} by Norton law [14]. Therefore, gain of creep strain intensity makes $d\varepsilon_{\text{eq}}^{\text{cr}} = A\sigma_{\text{eq}}^n dt$ for dt time increment.

For baffle material at $T = 650$ °C the creep function $\dot{\varepsilon}_{\text{eq}}^{\text{cr}}(\sigma)$ looks like

$$d\varepsilon_{\text{eq}}^{\text{cr}} = 6.07307 \cdot 10^{-14} \sigma^{4.8351} dt. \quad (4)$$

Dependence (4) is shown in Figure 6.

Radiation swelling model. Dependence of radiation swelling $d\varepsilon_{\text{eq}}^{\text{sw}}$ on damaging dose D have power nature [8, 15]:

$$\begin{aligned} \frac{d\varepsilon_{\text{eq}}^{\text{sw}}}{dt} &= C_D n D(t)^{n-1} f_1(T) f_2(\sigma_m, \sigma_{\text{eq}}) f_3(\mathbf{x}) \frac{dD}{dt}; \\ d\varepsilon_{\text{eq}}^{\text{sw}} &> 0; \quad d\varepsilon_{\text{eq}}^{\text{sw}} \Big|_{t=0} = 0; \\ f_1(T) &= \exp(-r(T - T_{\text{max}})^2); \\ f_2(\sigma_m, \sigma_{\text{eq}}) &= 1 + 8 \cdot 10^{-3} (0.85\sigma_m + 0.15\sigma_{\text{eq}}); \\ f_3(\mathbf{x}) &= \exp(-8.75\mathbf{x}); \\ C_D &= 1.035 \cdot 10^{-4}; \quad n = 1.88; \\ r &= 1.825 \cdot 10^{-4}; \quad T_{\text{max}} = 470 \text{ °C}; \\ \sigma_m &= \frac{\sigma_{xx} + \sigma_{yy} + \sigma_{zz}}{3}, \end{aligned} \quad (5)$$

where σ_{xx} , σ_{yy} , σ_{zz} are the normal components of stress tensor;

$$\mathbf{x} = \int_0^D d\varepsilon_1^{\text{p}},$$

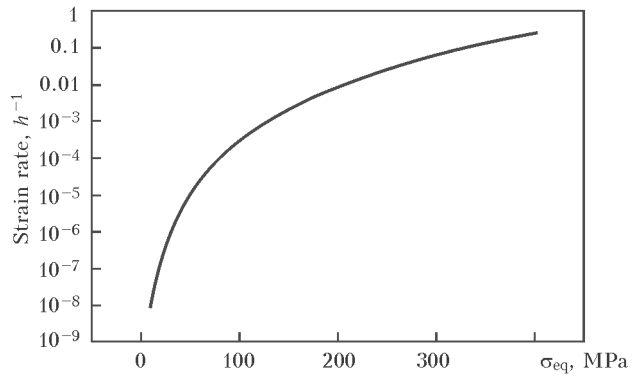


Figure 6. Creep function for steel 08Kh18N10T at $T = 650$ °C

where $d\varepsilon_i^{\text{p}} = \frac{\sqrt{3}}{2} \sqrt{d\varepsilon_{ij}^{\text{p}} d\varepsilon_{ij}^{\text{p}}}$, $i, j = 1, 2, 3$ is the intensity of plastic strain gain.

In order to consider radiation creep the expression is supplemented with relationship

$$\begin{aligned} \frac{d\varepsilon_{\text{eq}}^{\text{cr}}}{dt} &= \left(B_0 \frac{dD}{dt} + \omega \frac{d\varepsilon_{\text{eq}}^{\text{sw}}}{dt} \right) \sigma_{\text{eq}}; \\ d\varepsilon_{\text{eq}}^{\text{cr}} &> 0; \quad \varepsilon_{\text{eq}}^{\text{cr}} \Big|_{t=0} = 0; \\ B_0 &= 1 \cdot 10^{-6} (\text{MPa} \cdot \text{dpa})^{-1}; \\ \omega &= 2.95 \cdot 10^{-3} \text{ MPa}^{-1}. \end{aligned} \quad (6)$$

A total tensor of swelling strain gain $d\varepsilon$ is present as a sum of gain of radiation creep strain $d\varepsilon_{\text{eq}}^{\text{cr}}$ (deviator component) and gain of radiation swelling $d\varepsilon_{\text{eq}}^{\text{sw}}$ (spherical component) in this time step:

$$d\varepsilon = \frac{1}{3} d\varepsilon_{\text{eq}}^{\text{sw}} \mathbf{I} + d\varepsilon_{\text{eq}}^{\text{cr}} \mathbf{n}, \quad (7)$$

where \mathbf{I} is the identity tensor; $\mathbf{n} = d\sigma_{\text{eq}}/d\sigma$ is the stress intensity; σ is the stress tensor.

Strain gains $d\varepsilon$ are summed in all time steps, ε is the total tensor of radiation swelling strain, and its first variant is taken for volumetric swelling strain.

The relationships taken from [7] allows considering the change of material yield strength depending on radiation dose as well as temperature (see Figure 4) in the radiation swelling problem:

$$\begin{aligned} \sigma_{0.2}(T, D) &= \begin{cases} \sigma_{0.2}^0(T) + \Delta\sigma_{0.2}^T(T, D), & D < D^* \\ \sigma_{0.2}^*(T) + \Delta\sigma_{0.2}^*(D), & D \geq D^* \end{cases} \\ \sigma_{0.2}^0(T) &= 155 + 239 \exp(-2.22 \cdot 10^{-3} (T + 273)), \text{ MPa}; \\ \Delta\sigma_{0.2}^T(T, D) &= (\sigma_{0.2}^*(T) - \sigma_{0.2}^0(T)) \frac{\sqrt{1 - \exp(-C_{\sigma_{0.2}} D)}}{\sqrt{1 - \exp(-C_{\sigma_{0.2}} D^*)}}; \\ \sigma_{0.2}^*(T) &= 650 + 1405 \exp(-5.9 \cdot 10^{-3} (T + 273)), \text{ MPa}; \\ \Delta\sigma_{0.2}^*(D) &= A_{\sigma_{0.2}} \left(\sqrt{1 - \exp(-C_{\sigma_{0.2}} D)} - \sqrt{1 - \exp(-C_{\sigma_{0.2}} D^*)} \right); \\ D^* &= 7 \text{ dpa}, \quad C_{\sigma_{0.2}} = 0.126 \text{ dpa}^{-1}, \quad A_{\sigma_{0.2}} = 621 \text{ MPa}. \end{aligned} \quad (8)$$

Table 3. Maximum compressive/tension RWS in baffle, MPa

Stage	Radial	Circumferential	Axial (longitudinal)
1. After welding	-64/90	-52/105	-109/304
2. Heat treatment — heating	-41/57	-41/75	-67/170
3. Heat treatment — hot state after tempering	-23/24	-21/29	-27/50
4. Cold state after heat treatment	-30/31	-27/37	-34/65

Results. A field of RWS was received in baffle ESW taking into account heat treatment.

The problem of baffle radiation swelling was solved for two cases, i.e. taking into account RWS effect and without it.

All the problems are nonlinear and were solved using tracing on time with the help of finite-element method. The problem of RWS evaluation was solved in 3D problem statement, all the rest were made in 2D under the condition of generalized plain strain. The 2D problems consider median section of baffle ring.

Residual welding stresses. Table 3 shows the change of maximum tensile and compressive stresses after welding and in process of heat treatment. The maximum stresses after welding/heat treatment are axial (longitudinal) and their distribution is shown in Figure 7.

The RWS field is laid in the radiation swelling calculation as an initial condition. Model (5) takes into account the effect of stresses on swelling value, therefore, the differences in the swelling fields with and without welding are predicted.

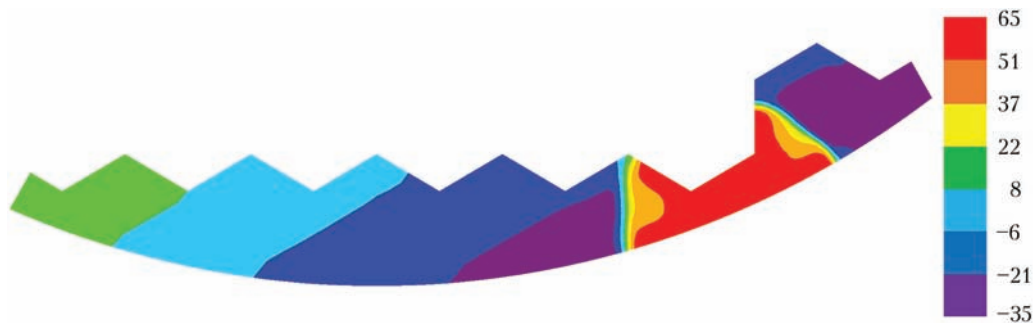


Figure 7. Distribution of axial (longitudinal) RWS in baffle after heat treatment

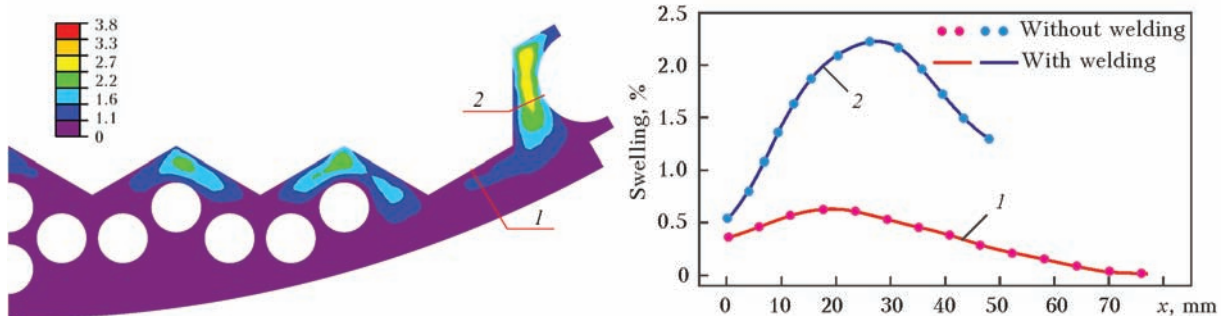


Figure 8. Field of volumetric swelling strain in baffle after 60 years of operation, and distribution of swelling in sections 1 and 2 in the problems with and without RWS

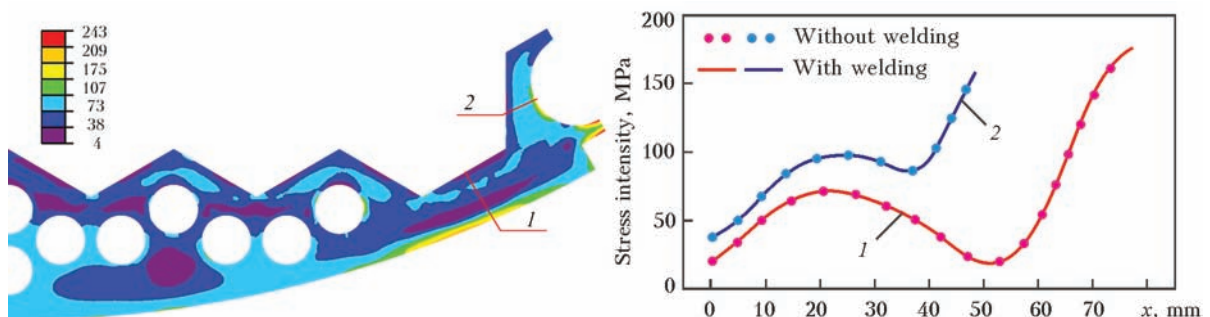


Figure 9. Field of stress intensity in baffle after 60 years of operation, and distribution of stresses in sections 1 and 2 in the problems with and without RWS

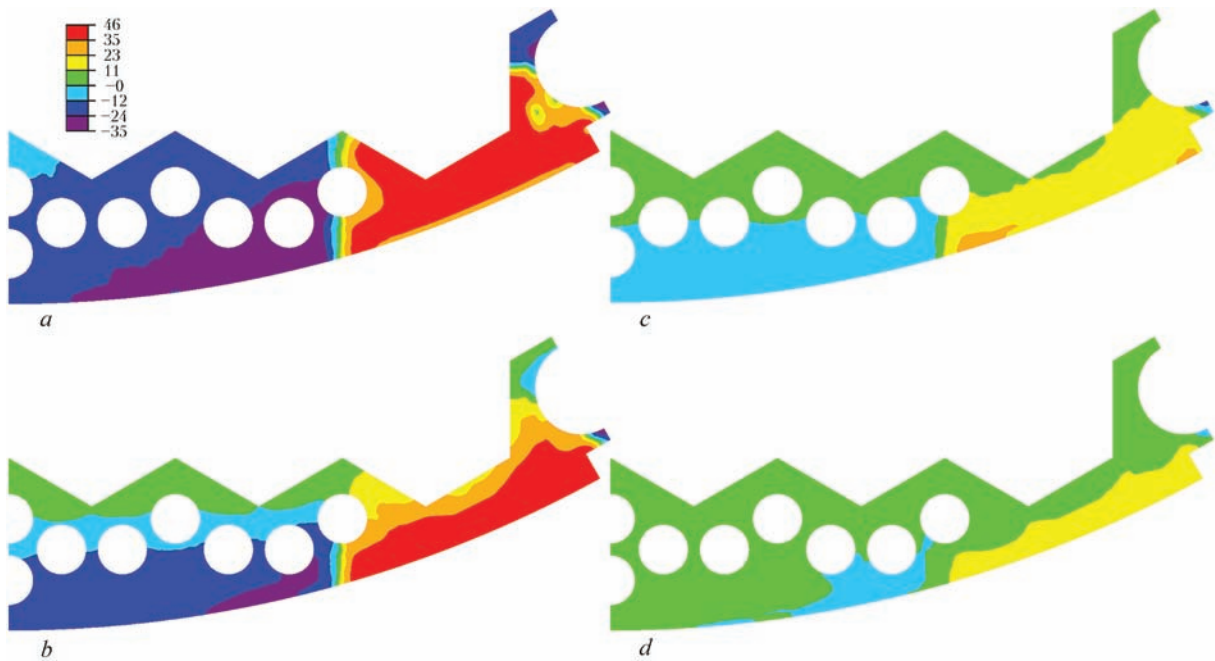


Figure 10. Relaxation of RWS in WWER-1000 baffle: *a* — in the beginning of operation; *b* — after 20; *c* — after 40; *d* — after 60 years of operation

Effect of RWS on in-service swelling and SSS. Figure 8 shows the results of calculation of baffle swelling on models (5)–(8).

The results of calculation of stressed state on models (5)–(8) are shown in Figure 9.

Discussion. The maximum RWS are axial one and in section *I* have sign «+», i.e. being tensile. Tensile stresses according to the model promote growth of radiation swelling. However, the results in Figure 8 do not indicate significant effect of RWS on radiation swelling. In other words, RWS at 65 MPa level are not large enough for influencing the value of swelling in zone of baffle welds.

Besides, as can be seen from Figure 9, *a*, difference of stress distribution in section *I* after 60 years of operation makes around 6 MPa, that is significantly lower than RWS level laid in swelling calculation. Such RWS behavior is explained by the effect of radiation creep, laid in the swelling model depending on (6). However, it is essential to find out the way of RWS relaxation under the effect of irradiation. For this, the difference of axial stress fields in the baffle was calculated in different moments of time after operation start. Such an approach allows tracing the history of change of RWS contribution in the total stressed state.

Figure 10 shows reduction of RWS in the baffle on time and explains the results, demonstrated in Figure 9: the stress fields in the baffle after 60 years of operation differ by about 6 MPa in swelling problems with and without welding.

It should be noted that RWS relaxation in the baffle does not happen immediately, it takes place in course

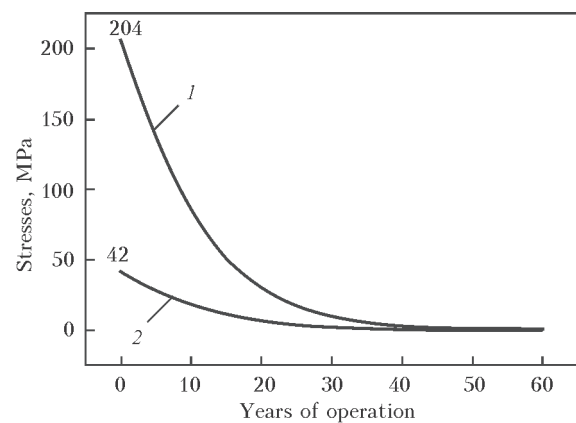


Figure 11. Quantitative characteristic of RWS relaxation in the WWER-1000 baffle in service: *1* — without heat treatment; *2* — after heat treatment

of 60 years of reactor operation. Qualitatively this effect can be described using the dependence

$$\sigma = \sigma_0 0.92^t, \quad (9)$$

where σ_0 is the RWS initial level in the baffle during reactor warming up for normal operation; t is the year of reactor operation.

Dependence (9) is the relationship which can be used for evaluation of static and cyclic strength as well as for evaluation of brittle fracture resistance of baffle material. This relationship is shown in Figure 11.

It should be noted that relationship (9) is received for specific output data such as volumetric heat generation and radiation dose [9, 10] which may significantly vary for different power units. Therefore, it is recommended to consider the welded joints in further evaluations on extension of life of WWER-1000 internals.

Conclusions

1. The work shows that RWS in WWER-1000 baffle taking into account heat treatment have virtually complete relaxation under effect of irradiation for the period of around 60 years.

2. The history of RWS effect in course of 60 years does not provoke significant change in baffle swelling in zone of welds.

3. The relationship has been deduced for evaluation of baffle RWS value during operation.

4. It is recommended to take into account welded joints in further evaluations of residual life of WWER-1000 internals.

1. (2000) *Irradiation effects on the evolution of the microstructure, properties and residual stresses in the heat affected zone of stainless steel welds*: INTERWELD Project. FIKSCT-2000-00103.
2. Makhnenko, O.V., Velikoivanenko, E.A., Mirzov, I.V. (2014) Redistribution of residual welding stresses in in-vessel core barrel of WWER-1000 reactor during operation. *The Paton Welding J.*, **11**, 8–14.
3. (1980) *Electroslag welding and surfacing*. Ed. by B.E. Paton. Moscow: Mashinostroenie.
4. (1975) *Main principles on welding and surfacing of assemblies and structures of nuclear power plants, pilot and research nuclear reactors and units*. Moscow: Metallurgiya.
5. Lychko, I.I., Sushchuk-Slyusarenko, I.I., Yushchenko, K.A. (1999) Specifics of electroslag welding of thick-wall long butts of 18-8 type steel. *Avtomatich. Svarka*, **9**, 61–65.
6. *GOST 30482–97*: Electroslag welding of steels. Requirements to technological process. Interstate Standard.
7. Sorokin, A.A., Margolin, B.Z., Kursevich, I.P. et al. (2011) Influence of neutron radiation on mechanical properties of internals materials of WWER type reactors. *Voprosy Materialovedeniya*, **66(2)**, 131–151.
8. Margolin, B.Z., Murashova, A.I., Neustroev, V.S. (2012) Analysis of influence of stressed state type on radiation swelling and radiation creep of austenitic steels. *Problemy Prochnosti*, **3**, 5–24.
9. Pishtora, V., Vandlik, S., Lauerova, D. et al. (2011) *Secondary operations on evaluation of technical state of reactor elements of power unit 1 of Yuzhno-Ukrainskaya NPP (Phase I)*: Report of IYaI.
10. Margolin, B., Fedorova, V., Sorokin, A. et al. (2012) The mechanisms of material degradation under neutron irradiation for WWER internals and methods for structural integrity assessment. In: *Proc. of Int. Conf. on Structural Integrity and Life of NPP Equipment* (1–5 Oct. 2012, Kiev, Ukraine).
11. Margolin, B.Z., Kursevich, I.P., Sorokin, A.A. et al. (2009) To problem of radiation swelling and radiation embrittlement of austenitic steels. Pt 2: Physical and mechanical principles of embrittlement. *Voprosy Materialovedeniya*, **58(2)**, 99–111.
12. Nejmark, B.E. (1967) *Physical properties of steels and alloys used in heat-power engineering*: Refer. Book. Moscow; Leningrad: Energiya.
13. *PNAE G-7002–86*: Codes of design on strength of equipment and pipelines of nuclear power units. Moscow: Energoatomizdat.
14. Rabotnov, Yu.N. (1966) *Creep of structure elements*. Moscow: GIFML.
15. Margolin, B.Z., Murashova, A.I., Neustroev, V.S. (2011) Effect of stresses on radiation swelling of austenitic steels. *Voprosy Materialovedeniya*, **68(4)**, 124–139.

Received 16.02.2015

PROPERTIES OF HIGH-ALLOYED METAL DEPOSITED USING ELECTROSLAG TWO-STRIP METHOD

A.A. BABINETS

E.O. Paton Electric Welding Institute, NASU
11 Kazimir Malevich Str., 03680, Kiev, Ukraine. E-mail: office@paton.kiev.ua

During surfacing of corrosion-resistant layer on the parts of power and chemical equipment it is often necessary to obtain a specified chemical composition and properties of deposited metal already in the first layer. The influence of current, voltage and deposition rate as well as the sizes of gap between the strips on the stability of electroslag process, geometric dimensions of deposited beads and volume of base metal in the deposited metal were investigated. The range of surfacing modes using two strips of stainless steel of 0.5×60 mm section was determined, in which a stable electroslag process with a good formation of deposited metal and minimum penetration of the base metal in the range of 7–9 %, i.e. $I_s = 1400\text{--}1500$ A, $U_s = 32\text{--}33$ V and $v_d = 14\text{--}17$ m/h; 16 mm gap between the strips, is observed. The mechanical properties of metal, deposited at these modes using strips ESAB OK Band 309LNb ESW and Sv-08Kh19N10G2B under flux ESAB OK 10.10, are at a sufficiently high level and meet the requirements specified to them. The obtained results may be used in selection or development of materials and technologies of anticorrosive surfacing of parts of power and chemical equipment. 11 Ref., 4 Tables, 5 Figures.

Keywords: electroslag surfacing, deposited metal, electrode strip, bimetal, corrosion-resistant layer, surfacing modes, mechanical properties

For protection against corrosion of parts of power and chemical equipment, electric arc surfacing of high-alloyed metal on low carbon steel is widely used performed under the layer of flux [1, 2]. Basically, surfacing is performed using one electrode strip of 0.5–0.8 mm thickness and 50–70 mm width, that depending on surfacing modes, provides the efficiency of 10–35 kg/h [2]. As the volume of base metal (VBM) in the deposited one amounts to 15–25 %, then to provide the required chemical composition of corrosion-resistant layer it is necessary to deposit two or more layers, that may lead to accumulation of microdefects, increase in the level of residual stresses, chemical and structural heterogeneity [3]. Under the difficult operation conditions, these factors can negatively influence the stability of deposited metal against the formation and development of hot cracking and intercrystalline corrosion, which negatively affects the service life of parts [4].

One of the ways for solving this problem is the use of methods and materials for surfacing, which would provide a minimum penetration of base metal. One of these methods is electroslag two-strip surfacing developed at the E.O. Paton Electric Welding Institute. According to some data [5–7], this method allows obtaining the required chemical composition of the deposited metal already in the first layer, that is particularly important in producing bimetallic products by surfacing of high-alloyed austenite steels on conventional structural steel. At the same time, the corrosion-resistant layer must also possess the necessary mechanical properties like sufficient strength, high ductility and impact toughness.

The aim of this work is to investigate the influence of current, voltage and deposition rate, as well as dimensions of the gap between the electrode strips on stability of electroslag process, geometric dimensions of deposited beads and VBM.

The scheme of electroslag two-strip surfacing process is shown in Figure 1. In the process two electrode strips are fed to the welding head at the same rate. The current supply is carried out through the copper insert located between the strips and thus providing a certain gap. The protection of surfacing area from atmosphere is carried out by electrically conductive flux. During surfacing at the first moment of time between the elec-

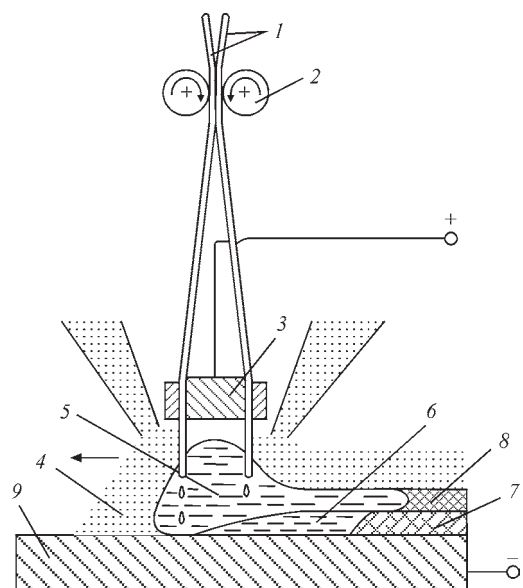


Figure 1. Scheme of electroslag two-strip surfacing [4]: 1 — electrode strips; 2 — feeding rollers; 3 — copper insert; 4 — slag (flux); 5 — slag pool; 6 — metal pool; 7 — deposited metal; 8 — slag crust; 9 — billet

Table 1. Chemical composition of strips for anticorrosion surfacing and volume fraction of δ -ferrite in the corresponding deposited metal [6–10]

Grade of strip	Volume fraction of elements, %						Volume fraction of δ -ferrite, %
	C	Mn	Si	Cr	Ni	Other	
Sv-03Kh22N11G2B	≤ 0.03	1.7	0.4	22	11.0	1.0 Nb	7–9
Sv-08Kh19N10G2B	0.09	1.8	0.4	20	10.4	1.3 Nb	2–8
Np-02Kh22N11G	≤ 0.02	1.5	0.4	22	11.0	-	2–6
LS-02Kh21N12G	≤ 0.02	1.2	0.4	21	11.5	-	2–8
LS-02Kh21N12G2B	≤ 0.02	1.7	0.4	21	11.5	0.3 Nb	2–8
ESAB OK Band 309L ESW	0.015	1.0–2.5	≤ 0.5	21–22	10–12	-	4–5
ESAB OK Band 309LMo ESW	Same	Same	≤ 0.4	19.5–21.5	13–14	2.8–3.3 Mo	Same
ESAB OK Band 309LNb ESW	»	»	≤ 0.4	20–22	11–13	0.4–0.8 Nb	»

Table 2. Chemical composition of fluxes for anticorrosion electroslag surfacing [6–10]

Grade of flux	Volume fraction of components, %						
	SiO ₂	MnO	CaO	Al ₂ O ₃	CaF ₂	FeO	Other
AN-72	8	1.0	30.0	20.0	30	≤ 2	10 ZrO ₂
AN-90	27*	-	23.5	10.5	39	-	-
ESAB OK 10.10	8*	-	-	25.0	63	-	-
ESAB OK 10.14	10*	-	-	20.0	70	-	-

*SiO₂ + MgO.

Table 3. Chemical composition of metal deposited using electroslag method with two strips OK Band 309LNb ESW

Number of deposited layers	Volume fraction of elements, %							
	C	Mn	Si	Cr	Ni	Nb	S	P
1	0.014	1.43	0.67	22.7	12.5	0.59	0.005	0.017
2	0.017	1.47	0.65	22.4	12.4	0.63	0.005	0.017
3	0.017	1.42	0.70	23.1	12.8	0.58	0.007	0.019

trode and the workpiece the arc appears, which melts the edges of strips, contributes to melting of flux and formation of slag pool, shunting the arc. Then the arc process is transferred into slag one, as far as current begins to run through the molten electrically conductive slag. The heating and melting of strips occurs due to heat transfer from the molten slag.

The main factors influencing the stability of electroslag process are compositions of strips and fluxes, surfacing modes and value of gap between the strips [5]. For anticorrosive surfacing at the present time a large number of surfacing materials were developed. As the electrode materials, the cold-rolled, flux-cored and sintered strips of grades Sv-08Kh19N10G2B, Np-02Kh22N11G, LS-02Kh21N12G2B, ESAB OK Band 309L ESW, ESAB OK Band 309LNb ESW, etc., as well as fluxes of grades AN-72, AN-90, ESAB OK 10.10, ESAB OK 10.14 etc. are mainly applied [5, 8–10].

Moreover, the composition of flux greatly influences the quality of deposited metal [7, 8]. First of all, the flux should have a high viscosity and be sufficiently «long» to provide a good formation of deposited metal. In addition, the flux should have a sufficient electric resistance, which provides generation of necessary amount of heat in the slag pool, at the same time increasing heating of electrode strips and improving efficiency of the deposition process. The

chemical composition of some corrosion-resistant cold-rolled and sintered surfacing strips is shown in Tables 1 and 2 [6–10]. The presence of certain amount of δ -ferrite in the austenite deposited metal provides its high resistance against crack formation [11].

In this work, strips ESAB OK Band 309LNb ESW of 0.5×60 mm cross-section and flux ESAB OK 10.10 were used in the experiments. For comparison, in some experiments strip Sv-08Kh19N10G2B of the same section was also used. Surfacing was performed on the billets of St3 steel of 200×100×30 mm dimensions, the current and voltage values were changed in the ranges of 1200–1600 A and 25–38 V, respectively. The deposition rate varied between 10–30 m/h, and the gap between the strips was 8–20 mm, the stickout of the strips remained unchanged and amounted to 35 mm.

After deposition the layer-by-layer spectral analysis of chemical composition of the deposited metal was conducted, the results of which are given in Table 3. The analysis of data, given in Tables 1 and 3, shows that in electroslag two-strip surfacing the specified chemical composition is achieved already in the first deposited layer.

The influence of current, voltage and deposition rate, as well as of gap between the strips on the stability of electroslag process, geometric sizes and VDM were investigated. It was found that sizes of the deposited

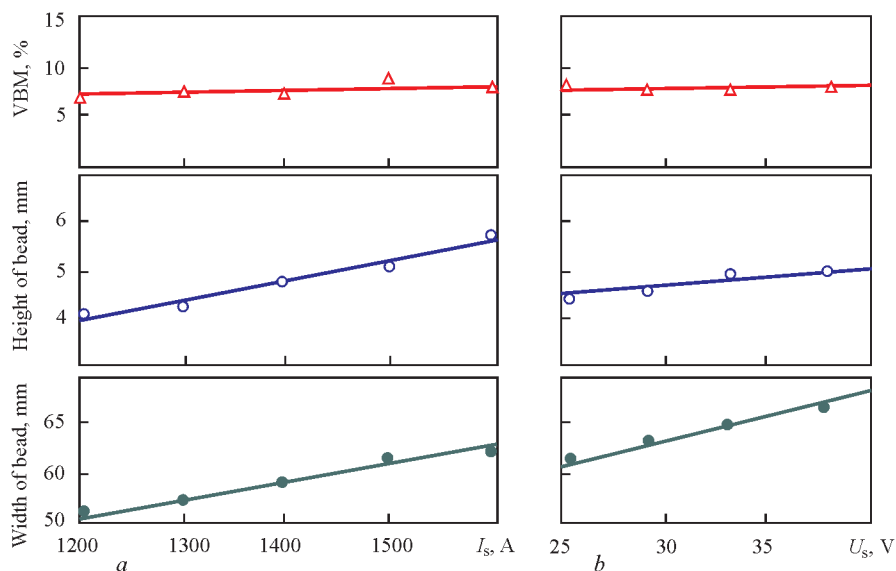


Figure 2. Influence of current (a) and voltage (b) of surfacing on geometric dimensions of deposited bead and VBM

bead are almost directly proportional to current and voltage, but VBM value remains almost unchanged (Figure 2). This is explained by the fact that during electroslag process the direct effect of arc on the base metal is absent, so increase in electric power affects mainly the increase in amount of deposited metal only.

The greater influence on VBM is provided by deposition rate, as well as the value of gap between the strips (Figure 3). The deposition rate determines duration of thermal effect of slag pool on the base metal, and the gap value significantly affects the stability of electroslag process itself.

The stability was determined by oscillograms as the ratio of duration of periods of electroslag and arc processes over the certain time. At small gap size the overheat of slag pool between the strips occurs, unsta-

ble slag-arc process is observed, in connection with which the penetration of base metal is increased and formation is deteriorated. With increase in the gap the area of the slag pool surface increases, the pool temperature is reduced and the stability of electroslag process N is improved (see Figure 3, b). From Figure 4 it is seen that at gap width of 16 mm, deposited bead has a more equal edges and smoother surface than the bead produced at the same mode, but with gap width of 8 mm.

It was found that a stable electroslag process using strips of 0.5×60 mm section is achieved under the following surfacing parameters: $I_s = 1400\text{--}1500$ A; $U_s = 32\text{--}33$ V; $v_d = 14\text{--}17$ m/h; and gap between the strips of 16 mm. Metallographic investigations showed that the specimens deposited at these modes

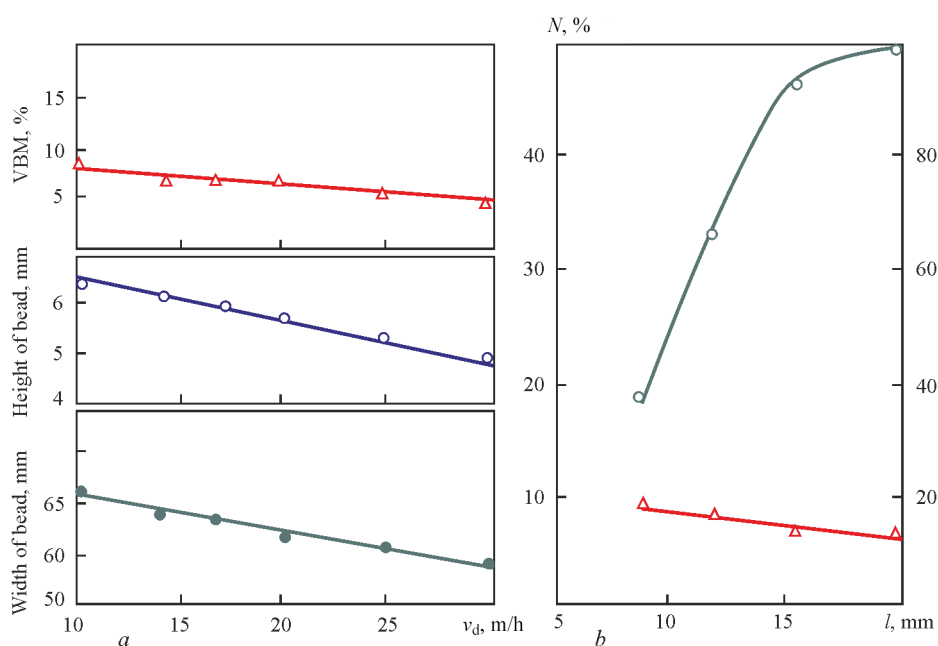


Figure 3. Influence of deposition rate (a) and gap between the strips (b) on geometric dimensions of deposited bead, VBM and process stability

Table 4. Mechanical properties of deposited metal at 20 °C

Deposited metal	σ_p , MPa	σ_y , MPa	δ , %	ψ , %
ESAB OK Band 309LNb	504–506	286–297	44–49	64.0–69.7
08Kh19N10G2B	523–588	295–314	24–28	52–55

**Figure 4.** Influence of gap size between the strips on stability of electroslag process at $I_s = 1200$ – 1300 A, $U_s = 32$ – 33 V, $v_d = 14$ m/h: a — $l = 8$ mm; b — $l = 16$ mm

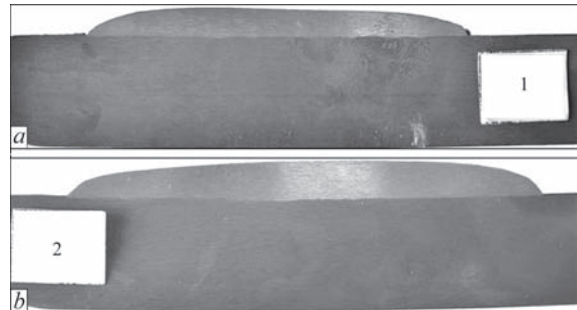
are characterized by a good formation of deposited metal and a minimum penetration of base metal in the ranges of 7–9 % (Figure 5). At the same time, the fusion boundary of deposited and base metal is flat enough, that positively affects the strength properties of the produced joint.

To determine the mechanical properties of the deposited metal, multi-layer surfacing was produced at the mode mentioned above. The total thickness of deposited metal was 16 mm, and the width was 62–65 mm. From the deposited billet the specimens for mechanical tests were cut out. The mechanical properties of the investigated deposited metal were determined at the temperature of 20 °C in the initial state applying tensile tests of specimens according to GOST 6996–66, the results of which are given in Table 4. For comparison, it presents also the mechanical properties of the metal deposited using electroslag two-strip method of widely used grade Sv-08Kh19N10G2B.

The test results show that the strength characteristics of the metal deposited using strips ESAB OK Band 309LNb ESW and Sv-08Kh19N10G2B are at sufficiently high level and meet the requirements specified to them. The obtained results may be used in selection or development of materials and technologies of anticorrosive surfacing of the parts of power and chemical equipment.

Conclusions

1. The range of surfacing modes using two stainless steel strips of 0.5×60 mm section, at which a stable electroslag process with a good formation of deposited metal and minimum 7–9 % penetration of base metal in the range

**Figure 5.** Macrosections of specimens deposited at two modes: a — $I_s = 1400$ A (VBM = 7 %); b — $I_s = 1500$ A (VBM = 9 %), with $U_s = 32$ – 33 V, $v_d = 12$ m/h and $l = 16$ mm

is achieved, i.e. $I_s = 1400$ – 1500 A, $U_s = 32$ – 33 ; $v_d = 14$ – 17 m/h, and 16 mm gap between the strips.

2. The mechanical properties of the metal deposited using electroslag method with strips ESAB OK Band 309LNb ESW and Sv-08Kh19N10G2B under flux ESAB OK 10.10 are at the sufficiently high level and meet the requirements specified to them.

- Kravtsov, T.G. (1978) *Electric arc surfacing by electrode strip*. Moscow: Mashinostroenie.
- Ryabtsev, I.A. (2005) High-efficiency wide-layer surfacing using electrode wires and strips (Review). *The Paton Welding J.*, **6**, 31–35.
- Ivanov, V.P., Ivashchenko, V.Yu. (2011) Influence of hardfacing technology and heat treatment on structure and properties of metal deposited on carbon steel by LN-02Kh25N22AG4M2 strip electrode. *Ibid.*, **8**, 7–9.
- Fetisov, G.P., Karpman, M.G. (2001) *Materials science and technology of metals*. Moscow: Vysshaya Shkola.
- Frumin, I.I., Kalensky, V.K., Panchishin, Yu.A. et al. (1977) Development of process and examination of some technological specifics of electroslag surfacing by strips. In: *Theoretical and technological principles of surfacing. New processes of mechanized surfacing*, 83–88. Kiev: PWI.
- Kalensky, V.K., Panchishin, Yu.A., Shekhter, S.Ya. et al. (1980) Application of electroslag surfacing using sintered strips for manufacturing of double-layer sheet billets. In: *Theoretical and technological principles of surfacing. Properties and tests of deposited metal*, 89–92. Kiev: PWI.
- Ignatov, V.A., Murzin, V.V., Rokhlin, E.A. et al. (1980) Study of process of electroslag anticorrosive surfacing by two-strip electrodes. In: *Ibid.*, 101–106.
- Buga, V.M. (1978) Development of flux and investigation of deposited metal properties with regard to single-layer surfacing of nickel-chrome alloy. In: *Theoretical and technological principles of surfacing. Surfacing consumables*, 95–98. Kiev: PWI.
- Kalensky, V.K., Panchishin, Yu.A. (1985) On efficiency of anticorrosive electrode strip surfacing. In: *Surfacing. Experience and efficiency of application*, 35–40. Kiev: PWI.
- Production of equipment and consumables for welding and cutting. <http://www.esab.com/>
- (1974) *Technology of electric fusion welding of metals and alloys*: Monograph. Ed. by B.E. Paton. Moscow: Mashinostroenie.

Received 21.01.2016

IMPROVEMENT OF ELECTRON DEVICES FOR INITIAL AND REPEATED IGNITIONS OF ALTERNATING CURRENT ARC

N.M. MAKHLIN

SE Research Engineering Center of Welding and Control in Power Engineering
of E.O. Paton Electric Welding Institute, NASU
11 Kazimir Malevich Str., 03680, Kiev, Ukraine. E-mail:electro@paton.kiev.ua

Taking into account earlier carried investigations, considered are the issues of development of the electron devices for contactless initial and repeated ignitions of alternating current arc in mechanized arc welding. They generate high and increased voltage pulses being injected in an inter-electrode gap. It is shown that the most reasonable way for improvement of the electron devices is a development of combined striker-stabilizers. They have a possibility to function in a mode of initial ignition (striking) of the arc as well as in a mode of its burning stabilizing. It can be reached by means of using at least two independent forming circuits in the generators of high or increased voltage pulses of the striker-stabilizers. A variant of circuit solutions for the combined electron arc striker-stabilizer having series connection to welding circuit is presented and described for mechanized consumable electrode AC welding. 22 Ref., 2 Figures.

Keywords: *mechanized arc welding, alternating current, initial and repeated arc ignitions, arc stability, electron striker-stabilizers of arc, generators of high and increased voltage pulses*

Up to the moment the most widespread method of contactless initial ignition (striking) of welding or pilot arc in an inter-electrode gap is its impact ionization by means of electric breakdown of this gap by high-voltage pulses, being generated with the help of special generators (arc strikers) [1–7].

The methods based on application of increase voltage pulses have gained the widest application among the well-known methods for increase of AC welding arc stability. Such pulses are generated by special voltage boosters (arc stabilizers) and being fed in the inter-electrode gap once in a period (at the moments of beginning of cathode formation on a part) or at each change of welding current polarity. Also different methods which provide for high speed of change of arc voltage and current at current zero values are used [1–5, 7–12].

Regardless the fact that a nature of processes of initial and repeated welding arc ignition is different [3–5, 7, 9, 10], a design structures of special strikers and stabilizers of arc is the same. Along with, due to the process peculiarities which are realized by these devices, they differ from each other not only by amplitude, energy and time parameters of the output pulses, but algorithms and modes of control assemblies. In this connection, the design of striker-stabilizers in course of long time was realized via combination in a one block virtually two independent devices. One of the devices is functioning in a mode of initial ig-

niton and being controlled by open-circuit voltage of AC power source. The second one operates in a mode of arc reignition in welding with arc voltage regulation. The examples of such a solution can serve the arc striking and stabilizing blocks of UDG-301 and UDG-501 units for TIG welding of aluminum and its alloys, UDGU-301, UDGU-302 and UDGU-502 units for TIG welding of steels and non-ferrous metals [5].

Based on mentioned above, the researchers and developers in a course of long time have been trying to develop the combined electron arc striker-stabilizers which can effectively function in a mode of arc initial ignition as well as in a mode of its reignition. A series of such devices [5, 7, 13–19 as an example], was developed up to the moment, however, area of their application is limited by such arc welding methods as manual and automatic non-consumable welding in inert gases (TIG) and manual metal arc welding (MMA). A number of difficulties and limitations in application [9, 10, 20] were found in development of the combined electron arc striker-stabilizers for mechanized AC metal arc welding in shielding gas (MIG/MAG).

Therefore, the development of efficient striker-stabilizers of arc for MIG/MAG welding is still relevant tasks. The analysis of circuit design and structural peculiarities of known combined electron arc striker-stabilizers shows that the solution of this problem is possible under conditions of improvement of operation algorithms of these devices and their control

assemblies as well as functional assemblies of their power part, first of all, generators of high and increased voltage pulses (GVP).

The aim of present paper lies in consideration of some proposals, developed at the E.O. Paton Electric Welding Institute, on creation and improvement of the functional assemblies of power part of the combined arc strikers-stabilizers for AC MIG/MAG welding and presentation of the results of these investigations and experimental works in this direction.

Main peculiarities of design of combined striker-stabilizers for mechanized welding. Comparison of the requirements with main parameters of high-voltage pulses and stabilizing increased voltage pulses, which was carried out taking into account calculation relationships and recommendations given in works [13, 15, 21], as well as results of earlier provided investigations and experience of practical application of the combined electron striker-stabilizers shows that:

- for safe initial ignition of arc in MIG/MAG welding the strikers' initial high-voltage pulses should have energy $W_{sr,p}$ from 0.2 to 0.5 J, amplitude $U_{m\ sr,p}$ from 3 to 3 kV and duration $\tau_{sr,p}$ (at the level of $0.05U_{m\ sr,p}$) from 5 to 20 μm ;

- for stability of AC arc in MIG/MAG welding the arc stabilizers' increased voltage output pulses should have energy $W_{m\ st}$ from 0.6 to 1.0 J, amplitude $U_{m\ st,p}$ from 400 to 950 V and $\tau_{st,p}$ (at the level of $0.05U_{m\ st,p}$) from 100 to 1000 μm ;

- since $W_{st,p}$ values are virtually always exceed $W_{sr,p}$ values, and value of energy W_c , accumulated in a capacitive storage of GVP forming circuit, is determined as $W_c = C_c U_{c0}^2 / 2$ (where C_c is the capacitive storage condenser (condensers) capacity, and U_{c0} is the set voltage of its charge), then at the same U_{c0} value the capacity C_{c2} of GVP circuit, forming stabilizing pulse, should not less than $W_{st,p}/W_{sr,p}$ times exceed C_{c1} capacity, necessary for formation in GVP circuit of the pulses providing initial ignition (striking) of the arc;

- for mechanized methods of metal electrode welding and series connection of voltaic pulses in the welding circuit using pulse transformer, its coefficient of transformation $k_{tr} = N_{III}/N_I$ should equal one (where N_{III} is the number of winds of pulse transformer secondary coil; N_I is the number of winds of this transformer primary coil for the mode of primary initiation as well as for the mode of generation of stabilizing pulses);

- the largest value of I_{Cm} current amplitude in GVP forming circuit, determined by formula $I_{Cm} = U_{c0} \sqrt{C_c} / L_c$ [15, 16], in the mode of pulse generation for initial arc ignition, makes from 80 to 445 A,

and it is from 50 to 170 A in the mode of stabilizing pulse generation.

Analysis of the differences in required values of main parameters of high-voltage pulses and increased voltage pulses show that GVP of striker-stabilizer should include at least two independent from each other switching LC-circuits for such pulses generation.

At that for optimizing the design of power part of the striker-stabilizers it is reasonable to support stable supply voltage as well as use feedback signals on voltage $U_{fb,v}$ in the inter-electrode gap and on arc current $U_{fb,c}$ in all modes of its operation.

The E.O. Paton Electric Welding Institute together with SE «Research Engineering Center of Welding and Control in Power Engineering» has developed and tested a series of the combined striker-stabilizers for mechanized AC welding using consumable electrode, description of base design model of which is given below. This work follows from mentioned above processes of contact-free initial and repeated ignitions of the arc and determined by these peculiarities requirements to main parameters of high-voltage pulses and increased voltage pulses initiating these processes.

Design of base model of the combined striker-stabilizer for AC mechanized welding. Figure 1 shows a design-functional scheme of base model of the combined striker for AC MIG/MAG welding*. The device is a modernized variant of asynchronous arc striker-stabilizer (AASS) with output pulse transformer *TV1*, where number of winds in each of coils equals one. The secondary coil *III* of this transformer is formed by consumable electrode part moving via opening of transformer ferromagnetic core from cassette to arc.

One of the ends of coil *III*, turned directly to the arc, is a stick-out of the consumable electrode contacting with welding electrode tip, and the second end is the sliding contact of moving consumable electrode with contact surfaces of embedded in the device contact assembly being located as close as possible to the outlet of guiding channel of output pulse transformer *TV1*. The device in addition to transformer *TV1* contains storage capacitors *C1*, *C2* and protective capacitor *C3*, output rectifier *I*, direct current voltage multipliers 2 and 3, control block 4, controlled high-voltage switching keys 5–8, contact assembly 9, at that keys 5–7 can have unidirectional conductance and key 8 — double-directional.

*Makhlin N.M., Korotynsky O.E., Skopyuk M.I. Device for ignition and stabilization of AC arc burning in mechanized consumable electrode welding: Pat. appl. 10698 UA. Fill. 03.11.2015.

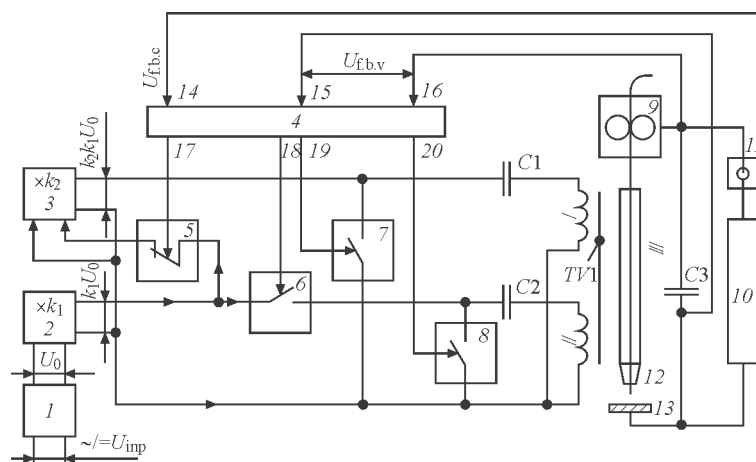


Figure 1. Block diagram of striker-stabilizer for mechanized AC welding using consumable electrode (see designations in the text)

In a primary stage of welding process in the mode of arc initial ignition keys 6, 7 and 8 are switched off, and key 5 is switched on by a signal from control output 17 of control block 4. U_{inp} voltage of input rectifier 1 is subjected to rectification, smoothing and filtering. It is supplied to input of this rectifier from AC mains or arc power supply secondary coil or from its outputs of alternating or direct current.

Smoothed and filtered voltage U_0 from input rectifier 1 is supplied to input of voltage multiplier 2, where this voltage is raised to $k_1 U_0$ level. Simultaneously, voltage $k_1 U_0$ from multiplier output 2 is supplied via switched on key 5 to multiplier input 3, using which this voltage is increased to $k_2 k_1 U_0$ level, i.e. to set charge level of storage capacitor C1.

Key 7 starts to generate control signal at the end of charge of this capacitor in the moment of time determined by control block 4 using voltage feedback signal $U_{f,b,v}$ which are supplied to inputs 15 and 16 of control block 4, and corresponding to (80 ± 5) el. deg phase of voltage of AC mains or open-circuit voltage of AC arc power supply. This signal from control output 19 of control block 4 will be supplied to control input of key 7 that causes switching on of the latter.

In turn, key 7 switching promotes for a recharge of storage capacitor C1 via primary coil I of output pulse transformer TV1, that results in formation of high-voltage pulse on coils I and III. Key 7 is switched off after finishing the recharging of storage capacitor C1. Process of capacitor C1 charging is renewed from this moment. Further all the processes of charging and recharging of this capacitor are repeated as described above. High-voltage pulses from coil III of output pulse transformer TV1 are applied via protective capacitor C3 to the inter-electrode gap, which is formed by stick-out of consumable electrode 12 and part being welded 13, and initiate spark discharge in it. This provides for impact ionizing of the inter-electrode gap

and creates the conditions for ignition in it of stable arc discharge with the help of AC power source 10.

Signal $U_{f,b,c}$ is supplied from information output of arc current probe 11 to input 14 of control block 4 from the moment of formation of stable arc discharge in the inter-electrode gap. The level of it is proportional to arc current, which leads to complete termination of supply of any signals from outputs 17 and 19 of control block 4 to control inputs of keys 5 and 7. It respectively stops formation of the high-voltage pulses and their injection in the inter-electrode gap. A signal of key switching on is supplied from output 18 of control block 4 to control input of key 6 simultaneously with keys 5 and 7 switching on. This promotes for start of storage capacitor C2 charging to $k_1 U_0$ level. Pulse signal of key switching on is supplied from output 20 of control block 4 to control input of key 8 at the end of charge of storage capacitor C2 in the moment time, which is determined by control block 4 with the help of $U_{f,b,v}$ signals and corresponds to phase of 68–75 el. deg relatively to zero phase of power supply 10 open-circuit voltage.

At double-directional conduction of key 8 will promote oscillatory discharge and recharge of storage capacitor C2 via primary coil II of output pulse transformer TV1 due to what damping HF oscillations will appear in C2–key 8–coil II circuit of transformer TV1. Thus, capacity of storage capacitor C2 is obviously more than the capacity of capacitor C1, then HF pulse of increased voltage is formed in primary II and secondary III coils of transformer TV1. Amplitude and frequency of HF oscillations of the pulse is significantly lower and duration is significantly larger than in the HF pulse being formed in recharge of storage capacitor C1. In the moment of finish of charge and recharge of capacitor C2, key 8 is switched off and process of charge of storage capacitor C2 is renewed. Further all the processes of charge, discharge and recharge are repeated as described above. The HF

pulses of increased voltage from secondary coil III of output pulse transformer TV1 are supplied via protective capacitor C3 in the inter-electrode gap promoting at that rapid increase of conductivity of this gap in the intervals of no-current conditions, which inevitably appear in arc current polarity change, thus creating conditions for free ignition of each next semi-wave of arc current.

If there is a break in stability of AC arc during welding, it provokes for termination of supply of $U_{f.b.c}$ signal to input 14 of control block 4, that will promote corresponding change in state of outputs 17–20 of control block 4. As a result, the device for mechanized AC consumable-electrode welding automatically return to function in the mode of initial arc ignition, and after repeated generation of stable arc discharge in the inter-electrode gap it automatically passes to function in the mode of AC arc reignition.

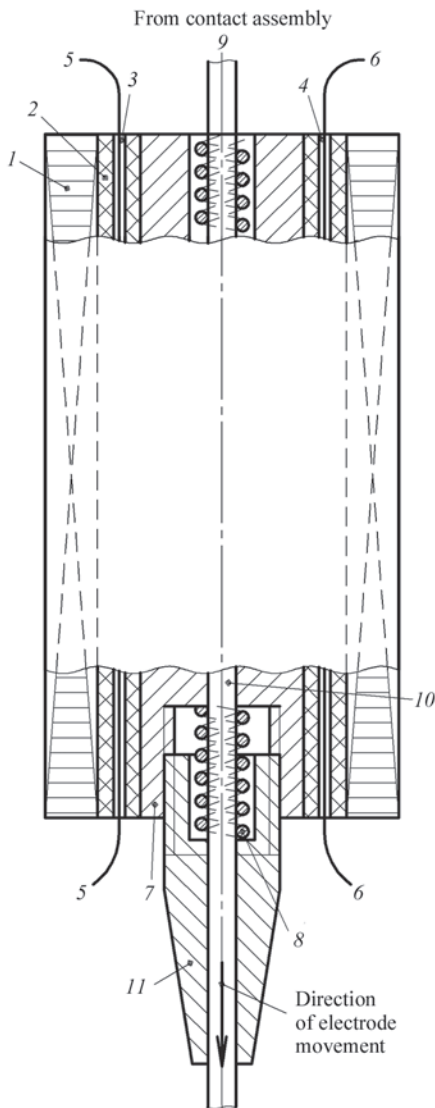


Figure 2. Variant of design scheme of output pulse transformer of striker-stabilizer for mechanized consumable-electrode welding (see designations in the text)

Among the peculiarities of developed combined striker-stabilizer for mechanized consumable-electrode welding is the necessity in use of high-voltage keys and feedbacks on arc current and voltage, special structure of output pulse transformer and presence of contact assembly.

The semiconductor power devices, for example, 65–95 class thyristors of T600N95 TOH type or FZ-75065KE3 type modules of INFINEON company [22] calculated for maximum-allowable collector-emitter 6500 B IGBT, can be used as electron high-voltage keys 5–8. The relationships and recommendations given in [14, 15] can be used in selection and calculation of parameters of the rest elements in design and construction of the striker-stabilizer for mechanized consumable-electrode welding and devices similar to it.

Figure 2 gives a scheme of one of the possible variants of design of the output pulse transformer of striker-stabilizer for mechanized consumable-electrode welding. The transformer consists of ferromagnetic core 1 being a solid tubular cylinder or set of ring cores, manufactured from ferrite mixtures or sprayed iron [15], internal insulation high-temperature bush 2 with two longitudinal holes 3 and 4 in each of which a wind of separate primary coil of the transformer is located (for example, a wind of primary coil 5 in hole 3, and wind of primary coil 6 in hole 4), guiding channel, set in insulation bush 2, containing rigid external non-magnetic bush 7 and spring internal non-magnetic bush 8 with low friction resistance in movement along it of consumable electrode 9, which forms transformer secondary coil with it part 10. From the side faced to the arc, rigid tubular bush 7 is connected (for example by thread) with welding torch tip 11. Electrode wire 9 is wind off from cassette and with the help of feeder of automatic and semi-automatic device is forced through to the arc via the contact assembly of developed striker-stabilizer, guiding channel of its output pulse transformer and tip 11. Ferromagnetic core 1 and primary coils 5 or 6 provide for electromagnetic coupling with part 10 of electrode 9 during generation in GVP of the developed striker-stabilizer the high-voltage pulses or pulses of increased voltage, which stabilize arc burning. It results in formation of pulses in part 10 of electrode 9 with virtually the same parameters as in corresponding primary coil of the output pulse transformer.

The contact assembly of the developed striker-stabilizer can be made in form of one of the wide-known clamping mechanisms. One of the examples of design of such clamping mechanism can be a structure, the main elements of which represent two contacts. One of them is stable and rigidly fixed to contact assembly body structure through insulation. The second can be

moved in the direction normal to consumable electrode longitudinal axis up to reaching such clamping level which would provide, on the one hand, virtually, free movement of the consumable electrode, and on the other hand, safe sliding contact with it. Both contacts from the side turned to the consumable electrode are equipped with semi-cylinder grooves, forming cylinder-like cavity. It is used for pushing the consumable electrode through the guiding channel of the output pulse transformer under effect of feeder of automatic and semi-automatic device in the direction from cassette to arc.

The striker-stabilizers, designed based on scheme with the output pulse transformer (see Figure 1), the example of design solution of which is given in Figure 2, are successfully used in the experimental special units for spot argon-arc welding of aluminum sheets of building structures as well as in the pilot samples of the equipment for mechanized welding using 1.6–3.0 mm diameter consumable electrode.

Conclusions

1. It was determined, based on considered peculiarities of initial and repeated ignition of AC arc, that improvement of design of arc striker-stabilizers is possible by means of introduction in the power part of this devices of additional GVP circuit including, at least, additional semi-conductor key and series capacitive storages and additional primary coil of step-up pulse transformer and application together with it feedbacks on current and arc voltage.

2. Developed striker-stabilizer for mechanized gas-shielded consumable-electrode welding allows significant expansion in application of alternating current with this method of arc welding.

1. Paton, B.E., Zavadsky, V.A. (1956) Pulsed arc ignition in gas- and manual arc welding. *Avtomatich. Svarka*, **3**, 26–35.
2. (1974) *Technology of fusion welding of metals and alloys*. Ed. by B.E. Paton. Moscow: Mashinostroenie.
3. Leskov, G.I. (1970) *Electric welding arc*. Moscow: Mashinostroenie.
4. Temkin, B.Ya. (1981) *Theory and calculation of welding arc strikers*: Syn. of Thesis for Cand. of Techn. Sci Degree. Leningrad.

5. (1986) *Equipment for arc welding*: Refer. Book. Ed. by V.V. Smirnov. Leningrad: Energoatomizdat.
6. Farson, D., Courardy, C., Talkington, J. et al. (1998) Arc initiation in gas metal arc welding. *Welding Res. Suppl.*, **8**, 315–321.
7. Makhlin, N.M. (2015) Peculiarities of contactless ignitions of alternating current arc. *The Paton Welding J.*, **10**, 29–35.
8. Lauzhadis, A.I. (1967) Influence of current frequency on stability of arc and process of manual arc welding. *Avtomatich. Svarka*, **9**, 29–32.
9. Dymenko, V.V. (1985) *Improvement of process stability and extension of technological feasibilities of alternating current consumable electrode welding*: Syn. of Thesis for Cand. of Techn. Sci. Degree. Kiev.
10. Paton, B.E., Zaruba, I.I., Dymenko, V.V. et al. (2007) *Welding power sources with pulsed stabilizing of arc burning*. Kiev: Ekotekhnologiya.
11. Korotynsky, O.E. (2007) *High-efficient power sources for arc welding based on inductance-capacitance converters*: Syn. of Thesis for Dr. of Techn. Sci. Degree. Kiev.
12. <http://www.fronius.com/cps/rde/xchg/SID-A4272FC1-EE958500>
13. Makhlin, N.M., Korotynsky, A.E. (2014) Analysis and procedure of calculation of series connection electronic devices for contactless arc excitation. *The Paton Welding J.*, **1**, 30–40.
14. Makhlin, N.M., Korotynsky, A.E. (2015) Asynchronous exciters and stabilizers of welding arc. Analysis and design procedure. Pt 1. *Ibid.*, **3/4**, 24–35.
15. Makhlin, N.M., Korotynsky, A.E. (2015) Asynchronous exciters and stabilizers of arc. Analysis and calculation procedure. Pt 2. *Ibid.*, **7**, 26–37.
16. Dudko, D.A., Fedotenkov, V.G., Makhlin, N.M. (1980) Thyristor pulse generators of UPD-1 type. *Avtomatich. Svarka*, **6**, 61–63.
17. Fedotenkov, V.G., Shmakov, E.I., Ivanov, G.P. et al. *Device for arc ignition*. USSR author's cert. 601877. Int. Cl. B23K 9/06. Publ.14.12.77.
18. Shmakov, E.I., Fedotenkov, V.G., Kolesnik, G.F. et al. *Device for arc ignition*. USSR author's cert. 490592. Int. Cl. B23K 9/06. Publ. 05.11.75.
19. Makhlin, N.M., Korotynsky, O.E., Skopyuk, M.I. *Device for ignition and stabilizing of AC arc burning process*. Pat. 109334 Ukraine. Int. Cl. B23K 9/067, B23K 9/073. Publ. 10.08.2015.
20. Lenivkin, V.A., Klenov, G.G., Sagirov, Kh.N. et al. (1986) Ignition of arc in consumable electrode welding. *Avtomatich. Svarka*, **2**, 30–34.
21. (2008) *Theoretical principles of electrical engineering*: Refer. Book on theory of electric circuits. St.-Petersburg: Piter.
22. <http://www.infineon.com>

Received 23.11.2015

STATE-OF-THE-ART INVERTER POWER SOURCES WITH INCREASED POWER FACTOR

V.V. BURLAKA, S.V. GULAKOV and S.K. PODNEBENNAYA

Priazovsky State Technical University

7 Universitetskaya Str., 87500, Mariupol, Ukraine. E-mail: vburlaka@rambler.ru

The paper proposes circuit design of high-frequency transformer-isolated converter and three-phase input without intermediate rectification of input voltage. A system was built using modular approach, i.e. each phase contains identical high-frequency AC/DC transformer-isolated converters, the outputs of these converters have series connection. Application of principle of direct conversion allows reducing amount of elements in the source power circuit, thus, reducing energy loss. Besides, high-frequency energy transformation allows significant improvement of weight-dimension characteristics of the system. Application of special algorithm of power key control provides for the possibility of active correction of input power factor and neutralization of circuit frequency harmonics in source output voltage that significantly reduces the requirements to output filter. The developed source has fast response and can be used for welding processes requiring high rates of change of arc current. 14 Ref., 3 Tables, 4 Figures.

Keywords: *power source, welding inverter, power factor corrector, direct converter, direct conversion, power quality, galvanic isolation*

Modern inverter power sources usually use double energy conversion, namely alternating voltage of supply mains is rectified and smoothed, after what it is supplied to DC/DC converter providing set output parameters of electric energy and transformer isolation from the mains.

A converter of mains alternating voltage in direct one determines power factor (PF) of the source. Usually this problem is solved with the help of a diode bridge with high-value filtering capacitor [1, 2] connected to its output. The disadvantage of such conversion method is low PF of around 0.5–0.7 and large distortions of shape of consumed current curve.

PF can be increased by means of installation of active power factor rectifier-corrector [3–7] or using direct energy conversion method.

Work [8] proposes a variant of single-phase welding source, in which function of input voltage rectification is eliminated due to application of four-transistor chopper of alternating voltage and low-frequency (50 Hz) transformer with low dissipation. The source has good results on efficiency and PF, but application of LF transformer leads to deterioration of weight-dimension characteristics of the device using similar control principle. Besides, necessity in DC welding requires application of energy stores for single-phase sources. These stores provide arcing at zero circuit voltage. This can be a filter capacitor or output chokes.

Attention is also to be given to circuit design with PF correction [9, 10]. It uses three-phase step-down mains frequency transformer, and its secondary wind-

ings have loading on three step-down DC/DC converters with series outputs (Figure 1).

Diodes VD1–VD6 form three full-wave rectifiers and elements C1VT1VD7, C2VT2VD8, C3VT3VD9 — three step-down converters operating with common HF smoothing choke L1. Capacitors C1–C3 have small capacity and designed for limitation of pulse surges appearing at power transistor closing. At that, their effect on circuit current formation can be neglected.

Close to one PF is achieved by means of setting VT1–VT3 control pulse relative duration proportional to modules of momentary values of corresponding phase voltages. Mains frequency harmonics are suppressed at the output in supply from symmetrical mains that allows using choke L1 with low inductance.

Work [8] outlines a perspective problem of development of three-phase sources with isolating HF transformer and direct conversion and proposes a scheme of single-phase source with direct conversion and HF transformer isolation. The source is designed based on forward converter with transformer. The disadvantages of scheme proposed in [8] are improper application of magnetic mains of pulse transformer due to contact with magnetic flow constant component and impossibility of arc current keeping at zero mains voltage.

Use of source transformers can be improved due to application of push-pull operation. This problem was solved in modular source [11], Figure 2 shows mains design of its power part.

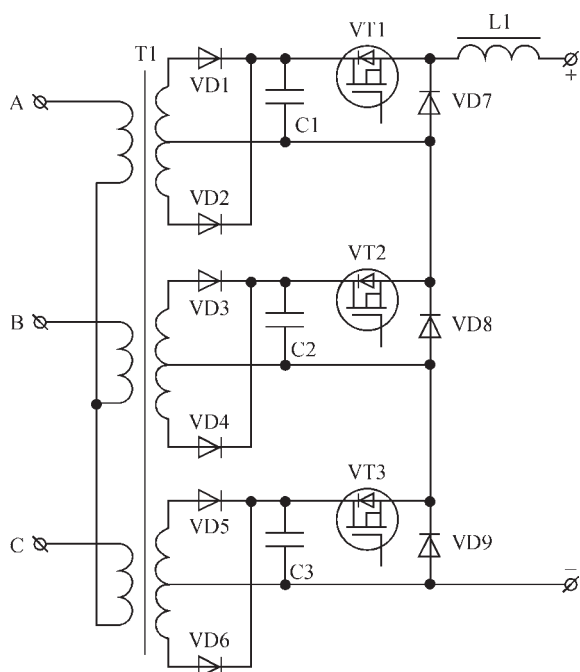


Figure 1. Scheme of hybrid source with LF transformer

Each phase of the source have connected HF transformer, the primary windings of which are switched on in such a way that magnetizing current has different polarity depending on switched on key (for phase A it is transformer T1 and keys S1 and S2). Two capacitors (C1, C2) are designed for power surge limitation in keys change. The transformer output winding is connected to two full-wave rectifier (diodes VD1, VD2). The outputs of rectifiers of all phases have series accordant connection and switched to the source output via smoothing choke L1.

Let's study the processes taking place in the elements, connected with phase A, since the processes in all other phases are similar. The same series of assumptions as in earlier described source is taken for analysis simplification.

Closure of key S1 provides for connection of the primary transformer winding to the input voltage. EMF of the output winding opens one of the output diodes (VD1 or VD2) and closes the second depending on the sign of input voltage. The current of primary winding of the transformer (and key S1) at that equals given load current. The voltages on capacitors C1, C2 are equal between themselves and to output voltage.

Closure of S1 promotes for cut of output winding voltage, load current is uniformly distributed between the output diodes. Key S1 current (it is magnetizing current T1) is flipped to capacitor C2.

S2 opening provokes for the same processes, but they are differ by the fact that a derivative of transformer linkage has opposite sign. It allows preventing saturation of magnetic core and providing push-pull operation mode.

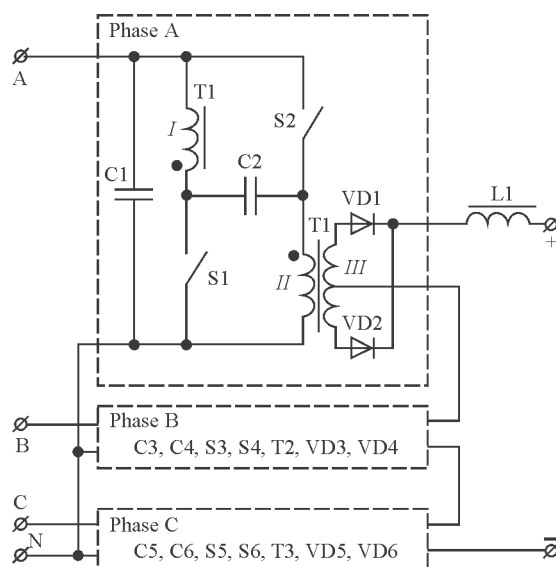


Figure 2. Power part of source with push-pull mode of transformer operation

It should be noted that keys S1, S2 should be designed for voltage not less than double amplitude of output phase voltage.

If power switches of phase A are switched with relative duration $D_a(t)$, the local average values of input current and output voltage for switching period (i.e. the average for the period of PWM carrier frequency) can be calculated. At that, maximum relative pulse duration makes $D_{max} = 0.5$ (at larger relative durations both keys will be switched simultaneously, that results in input short circuit). For better visualization Figure 3 shows equivalent network for local averages.

The local average input current equals

$$\hat{i}_a(t) = 2I_L \text{sign}(u_a(t))D_a(t). \quad (1)$$

Factor 2 appears because of the fact that the current is used 2 times during one switching period (one time at switched on S1 and the second at switched on S2). The sign of input current always matches with the voltage sign due to effect of output rectifier. The output voltage is respectively:

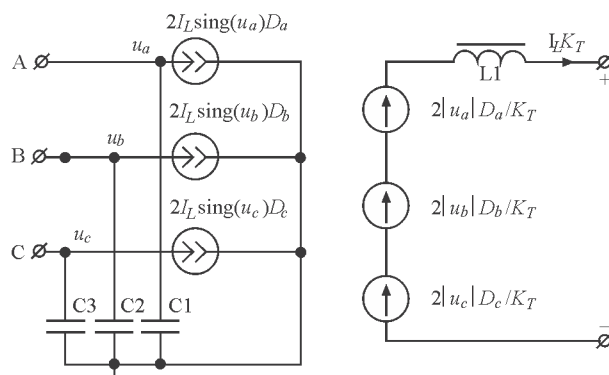


Figure 3. Equivalent network of Figure 2 source for local averages

$$\hat{e}_a(t) = 2 \frac{|u_a(t)|}{K_T} D_a(t). \quad (2)$$

The voltage is taken by modulo due to output rectifier.

The condition of close to one input power factor is $D_a(t) = v|u_a(t)|$, where v is the proportionality factor.

The output voltage of three phases of power source if supplied from three-phase symmetrical mains is

$$\begin{aligned} \hat{e}_a(t) + \hat{e}_b(t) + \hat{e}_c(t) &= 2 \frac{|u_a(t)|}{K_T} v |u_a(t)| + \\ &+ 2 \frac{|u_b(t)|}{K_T} v |u_b(t)| + 2 \frac{|u_c(t)|}{K_T} v |u_c(t)| = \\ &= 2 \frac{v}{K_T} (u_a^2(t) + u_b^2(t) + u_c^2(t)) = 3 \frac{v}{K_T} U_m^2. \end{aligned} \quad (3)$$

As can be seen from obtained expression, the output voltage does not include the components with mains frequency or its harmonics, that allows reducing inductance of output choke L1.

Control of output voltage is carried out by violation of parameter v at keeping the condition of relative duration limitation $D_a(t) \leq D_{\max}$. The following is received by substitution of the corresponding expressions:

$$v |u_a(t)| \leq D_{\max}; \quad (4)$$

$$v \leq \frac{1}{2U_m}. \quad (5)$$

Therefore, the maximum output voltage of the source is

$$[\hat{e}_a(t) + \hat{e}_b(t) + \hat{e}_c(t)]_{\max} = \frac{3U_m}{2K_T}. \quad (6)$$

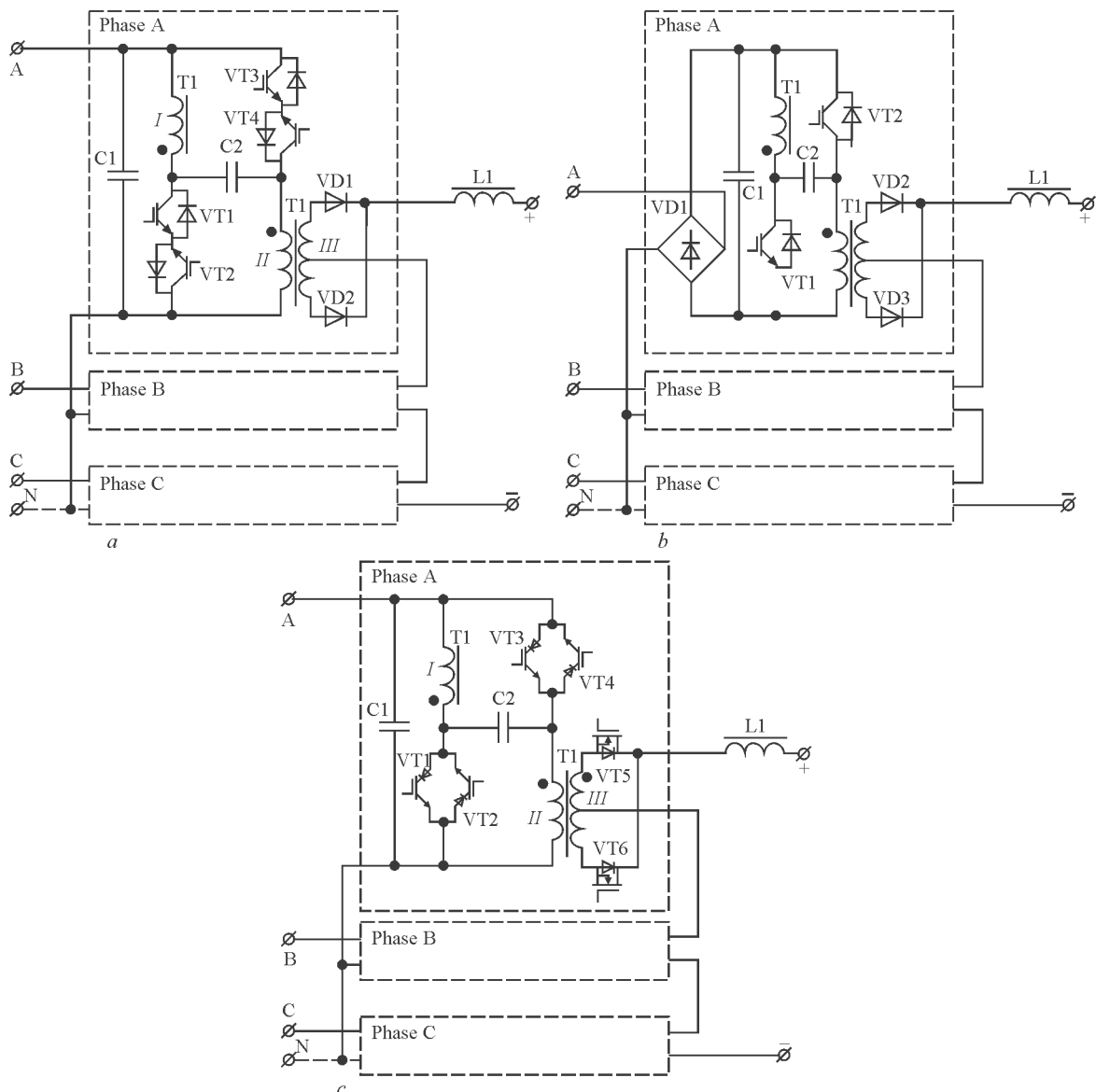


Figure 4. Variants of source power part in Figure 2 (for description see the text)

The maximum output voltage makes around 70 V with $U_m = 350$ V at practical implementation of three-phase source.

Amount of transformer winds is also determined from the condition of maximum inductance B_m in magnetic core. Let's determine amount of primary winds W_1 by equation of its maximum linkage, which take place at transfer of phase voltage through the maximum at set maximum output voltage. Taking into account push-pull mode of transformer operation (alternating magnetization from $-B_m$ to B_m) it can be written:

$$\frac{U_m D_{\max}}{f} = 2B_m S W_1; \quad (7)$$

$$W_1 = \frac{U_m D_{\max}}{2B_m S f}, \quad (8)$$

where S is the section of magnetic core, m^2 .

The variants of practical implementation of the source with power part based on Figure 2 can be different. Figure 4 shows several variants.

Figure 4, *a* shows bi-directional keys made in form of two back-to-back-series IGBT transistors with bypass diodes.

Variant, given in Figure 4, *b*, contains a diode bridge in the input of each phase modulus, that allows 2 times reduction of amount of power transistors and simplify control system. The price for simplification is reduced efficiency due to increase of number of semi-conductor elements in power mains (two diode bridges and transistor).

In variant in Figure 4, *c* the keys are made of two back-to-back parallel RB IGBT transistors capable to withstand reverse voltage. This solution allows reducing number of semi-conductor elements in the power mains to one, thus increasing efficiency. Besides, synchronous rectifier based on MOSFET transistors with low channel resistance is used for decrease of output energy loss.

Scheme of Figure 4, *a* is applied at practical implementation of the source. E42/21/20 (EPCOS) cores from N87 material with magnetic core section $S = 234$ mm^2 are used for phase transformers; the maximum inductance is taken equal $B_m = 0.25$ T. Switching frequency $f = 20$ kHz, $U_m = 350$ V. Using these data $W_1 = 75$ winds is obtained.

Power transistors are of STGW30N120KD type. Diodes of output rectifiers are the assemblies of 80CTQ150 type. Transformer ratio of HF transformers equals 7.5 (output winding has 2 sections by 10 winds). Capacitors have capacity of 4.7 μF and operating voltage 400 V. Output choke L1 has inductance 45 μH at 60 A current (43 winds for toroidal core T184-52).

Control scheme is made based on single-crystal microcontroller STM32F100C4T6B (STMicroelectronics), operating at 24 MHz frequency. For each phase the controller forms two impulse relative time signals F_1 and F_2 (for keys S1 and S2). These signals are distributed between transistors depending on sign of phase voltage. Table 1 shows such a distribution for phase A.

Formation of control signals for the transistor power gates is carried out with the help of special optical couplers FOD3120. Computational capabilities of applied microcontroller allows realizing source operation without connection to neutral circuit, at that balancing of input voltages of phase modules is carried out by program using known principle «two out of three» [12, 13], i.e. the correction of relative duration take place in phases with the maximum and minimum voltages that allows controlling displacement of Y-point formed by phase modules.

The source, based on scheme of Figure 4, *c*, can use IXRP15N120 (IXYS) transistors, and in output rectifier — IRFS4115-7P (International Rectifier) transistors. The transformers and capacitors are the same as in the source based on scheme of Figure 4, *a*. Formation of control signals for transistors of phase A is given in Table 2 (exclamatory mark (!) designates logical negation operation NOT).

Pairs of signals ($F_1; !F_1$) and ($F_2; !F_2$) are formed with dead time, necessary for corresponding switching of power keys.

Deterioration of the parameters at low loading can be explained by the fact that LF harmonics of rectifiers VD1C1 in Figure 4, *b* start prevailing in input current. In schemes (Figure 4, *a*, *c*) reduction of PF at

Table 1. Distribution of control signals

Phase to earth voltage	VT1	VT2	VT3	VT4
$U_{AN} > 0$	F_1	1	F_2	1
$U_{AN} < 0$	1	F_1	1	F_2

Table 2. Control signals for scheme in Figure 4, *c*

Phase to earth voltage	VT1	VT2	VT3	VT4	VT5	VT6
$U_{AN} > 0$	F_1	1	F_2	1	$!F_1$	$!F_2$
$U_{AN} < 0$	1	F_1	1	F_2	$!F_2$	$!F_1$

Table 3. Dependence of parameters of source prototype on output current

Output power, kW	0.25	0.5	1	1.8
Power factor	0.95	0.98	0.99	0.99
Mains current harmonics factor, %	28	15	5	4

low loading will take place due to capacitive current passing through input capacitors (C1 in Figure 4, a, c).

Setting of the relative duration of control pulses of key transistors being proportional to the modules of transient values of corresponding phase voltages is not the single possible algorithm for control of proposed converter. Thus, work [14] provides for a review of methods for formation of input currents in the active three-phase rectifiers under different conditions in supply mains, i.e. unbalance and presence of voltage higher harmonics. Regardless the fact that this network research is made for active current rectifiers and active voltage rectifiers, its results with some limitations can be applied to proposed direct converters since its equivalent network (see Figure 3) corresponds to the active current rectifier. It follows from the conclusions given in work [14] that at mains unbalance the optimum variant is control in order to minimize the output current pulsation, and the method, at which phase currents follow the shape of phase voltage is the best for mains voltage distortions.

Application of the considered converters of three-phase voltage allows eliminating distortions in supply mains voltage, reducing energy loss in the converter, improving its dynamic and weight-dimension characteristics.

1. Bin Wu (2006) *High power converters and AC drives*. New Jersey: IEEE Press, Wiley-Intersci.
2. Kolar, J.W., Friedli, T. (2011) The essence of three-phase PFC rectifier system. In: *Proc. of 33rd IEEE Int. Telecommunications Energy Conference* (9–13 Oct. 2011).
3. Lee, J.H., Kim, J.H., Kim, S.S. et al. (2001) Harmonic reduction of CO₂ welding machine using single-switch, three-phase boost converter with six order harmonic injection PWM. In: *IEEE ISIE Proc.*, Vol. 3, 1526–1529.
4. Salo, M., Tuusa, H., Hyqvist, J. (2001) A high performance three-phase DC voltage source — An application to a welding machine. In: *IEEE APEC Proc.*, Vol. 2, 793–799.
5. Huang, N., Zhang, D., Song, T. et al. (2005) A 10 kW single-stage converter for welding with inherent power factor correction. In: *IEEE APEC Proc.*, Vol. 1, 254–259.
6. Schenk, K., Cuk, S. (1997) A simple three-phase power factor corrector with improved harmonic distortion. *PESC*, 399–405.
7. Huang, Q., Lee, F. (1996) Harmonic reduction in a single-switch, three-phase boost rectifier with high order harmonic injected PWM. *Ibid.*, 790–797.
8. Rudyk, S.D., Turchaninov, V.E., Florentsev, S.N. (1998) Perspective welding current sources. *Elektrotehnika*, 7, 8–13.
9. Sekino Yoshihiro. *Three-phase rectifier*. Pat. 7-46846 A Japan. Int. Cl. H02M 7/25, 3/155, 7/08. Fil. 30.07.93. Publ. 14.02.95.
10. Burlaka, V.V., Gulakov, S.V. *Power source with three-phase input*. Pat. 63702 Ukraine for useful model. Int. Cl. H02H 7/09. Fil. 18.12.2009. Publ. 25.10.2011.
11. Burlaka, V.V., Gulakov, S.V. (2013) *Multiphase power source*. Pat. 102042 Ukraine for invention. Int. Cl. H02M 7/155. Fil. 14.05.2012. Publ. 27.05.2013.
12. Biela, J., Drogenik, U., Krenn, F. et al. (2007) Novel three-phase Y-rectifier cyclic 2 out of 3 DC output voltage balancing. In: *Proc. of 29th Int. Telecommunications Energy Conf.*, 677–685.
13. Biela, J., Drogenik, U., Krenn, F. et al. (2009) Three-phase Y-rectifier cyclic 2 out of 3 DC output voltage balancing control method. In: *IEEE Transact. on Power Electronics*, Vol. 24, Issue 1, 34–44.
14. Kondratiev, D.E. (2008) *Three-phase rectifiers with active power factor correction and bidirectional power transfer*. Syn. of Thesis for Cand. of Techn. Sci. Degree. Moscow.

Received 20.05.2015

COMPOSITION, STRUCTURE AND TECHNOLOGY FOR PRODUCTION OF ELECTRODE MATERIALS FOR ELECTRIC SPARK RESTORATION AND STRENGTHENING OF WORN-OUT PARTS*

A.V. PAUSTOVSKY, Yu.G. TKACHENKO, R.A. ALFINTSEVA, D.Z. YURCHENKO and V.G. KHRISTOV

I.M. Frantsevich Institute of Problems of Materials Science, NASU
3 Krzhizhanovsky Str., 03680, Kiev, Ukraine. E-mail: tkachenko_yuri@ukr.net

The electrode materials for producing electric spark coatings of Colmonoy–WC alloy containing 10–70 wt.% WC and hard alloys using TiC, Mo₂C, TiN, Co, Cr, Ni, Al were developed. The phase composition, structure, mass transfer kinetics, hardness and wear resistance of electric spark coatings of the developed alloys were investigated. It was shown that in Colmonoy alloys, Colmonoy–10 % WC and Colmonoy–25 % WC the structure of eutectic character is observed. At pulse energy of 7.5 J the thickness of formed coatings amounted to 3–5 mm. The wear resistance of coatings Colmonoy–WC is 3.5 times higher than that of Colmonoy alloy coatings. It was found that the structure and composition of the developed electrode materials of TiC-based hard alloys allows producing electric spark coatings of up to 100 μm thickness and with hardness of up to 14 GPa. The developed electrode materials were applied under the industrial conditions for strengthening and restoration of worn-out parts of structural steels using electric spark method. 4 Ref., 3 Tables, 7 Figures.

Keywords: *electric spark strengthening, electrode materials, restoration of parts, erosive properties, properties of coatings, wear resistance, heat resistance*

The producing of thick coatings using electric spark method for restoration of worn-out surfaces has a number of features, which require the development of electrode materials capable of erosion mainly in the liquid phase. The base for these compositions should be metals, erosion products of which adhere well to the base material. The realization of these principles in development of electrode materials will significantly increase the effectiveness of coating deposition on metal surfaces.

The eutectic alloys based on nickel and iron, containing alloying additives of boron, silicon and chromium, are used in producing plasma and detonation coatings [1]. The application of such alloys for electric spark alloying requires investigation of structure and properties of the produced coatings, development of technology for production of compact electrodes and development of technological process.

To produce the wear-resistant (0.5–2.0 mm thick) electric spark coatings the materials of electrodes of alloy with eutectic structure of Ni–Ni₃B system alloyed with silicon and copper and also with WC additives were investigated. The previous investigations [2] proved feasibility of work in this direction. In

the present study the investigations were carried out and the technology for producing eutectic Ni–Ni₃B alloy included into Colmonoy class, was developed. The technologies for producing powder mixtures of Colmonoy–WC system with a different ratio of components were developed. The technology was developed and the optimum modes for pressing and subsequent sintering of powder mixtures for production of electrodes were found, where the porosity does not exceed 10 %.

In order to produce coatings of high hardness and thickness of 40–80 μm the most effective direction of modern investigations consists in the development of electrode materials containing refractory compounds with metal bond, optimization of structural composition of this bond and technology for electrodes manufacture. It is feasible to conduct works on creation of electrode materials using TiC, Mo₂C, TiN, Co, Cr, Ni, Al.

Colmonoy–WC system alloys. The electrode materials Colmonoy–WC were manufactured using the following powder metallurgy methods: grinding, mixing, adding of plasticizer, pressing and sintering. For development of electrode material the powder al-

*According to the materials of the work performed within the frames of target integrated program of the NAS of Ukraine «Problems of Life and Safe Operation of Structures, Constructions and Machines» (2013–2015).

loy was used based on nickel belonging to the group of Colmonoy alloys produced using spraying method. This alloy is located in the area of triple eutectic with the main phase of Ni-based solid solution, the melting point of which is approximately 860 °C, that during electric spark alloying provides a high mass transfer and the coating thickness sufficient for restoration of worn-out parts. As an additive the copper was used. As a deoxidizer the silicon was used, which is the most effective alloying additive and significantly increases heat resistance. The hardness of the alloy depended on the amount of introduced tungsten carbide.

The tungsten carbide powder was grinded in a ball mill in the medium of rectified alcohol at powder:hard-alloyed balls:alcohol mass ratio of 2:6:1. The time of grinding was 72 h. The size of powder particles of the main fraction was less than 1 µm.

The Colmonoy–WC mixture was produced by grinding–mixing within 4 h at powder:hard-alloyed balls:alcohol mass ratio of 2:8:1. After grinding the mixture was dried in the exhaust hood and mixed with 5 % solution of synthetic rubber in gasoline. The produced mixtures were dried in the exhaust hood and grinded in the sieve 045. The powder mixtures Colmonoy–(10, 20, 25, 30, 40, 50, 70) wt.% WC were produced. The billets of 4×4×70 mm size were pressed in the hydraulic press at pressure of 300 MPa. The porosity of the billets was 40–42 %. The pressed billets were dried in the exhaust hood at 150 °C during 12 h.

The sintering of electrodes was performed in two stages. The preliminary sintering was carried out in the muffle furnace in the hydrogen environment at 800 °C for 2 h. The rate of increasing temperature was 0.06 °C/s. The specimens were placed into the bulky calcined alumina with 2 % additive of graphite grits. The final sintering was performed in the vacuum furnace at $6.67 \cdot 10^{-3}$ Pa and 960–980 °C for 2 h. At such a temperature of sintering the specimens have porosity of not more than 10 %, which is optimal. At higher porosity, which is obtained at lower temperature of sintering, the electrode is heated to 800–1000 °C in the process of coating deposition due to decrease in its thermal conductivity, and a significant oxidation of coating material occurs.

Colmonoy alloy has is the structure of hypoeutectic alloy, according to phase equilibrium diagram Ni–Ni₃B. The primary phase is the solid solution of boron, copper and silicon based on nickel with microhardness of 2.3 GPa; the secondary phase is the eutectic consisting of Ni-based solid solution and boron silicide phase based on nickel with microhardness of 7–8 GPa.

The X-ray phase analysis of cast nickel and Colmonoy indicates that during alloying of nickel with

silicon and copper the substitutional solid solutions are formed, and alloying with boron results in the formation of interstitial solid solution, as a result of which the lattice parameter of Ni-based solid solution increases from 0.3520 nm for nickel and to 0.3588 nm for Colmonoy (atomic radii are $a_{\text{Ni}} = 0.124$, $a_{\text{Si}} = 0.134$, $a_{\text{Cu}} = 0.128$ nm [3]).

The calculation of crystal lattice parameters for WC showed that in this case such elements as boron and silicon are dissolved in tungsten carbide forming substitutional solid solutions. Copper is dissolved in nickel. The microstructure of alloys containing 25, 50, 60, 70 and 80 % WC represents a conglomerate of fine-grained phases of Ni-based solid solution and refractory carbide-boron-silicide combinations. The produced microstructures have typical features of structures of hard alloys WC–Co (mixture of acicular-like phases of WC and metal-based solid solution).

The electric spark treatment of surface of steel 45 was carried out by the developed Colmonoy–WC alloys in ELITRON-52 installation at zero mode with voltage of 100 V and pulse energy of 7.5 J. The mass transfer from anode to cathode was measured by weighing the specimens on analytical balance. The hardness of the coating was measured in PMT-3 device. The value of mass transfer for the electrodes with different contents of WC (from 10 to 70 wt.%) was respectively changed from 2.30 to 0.49 g/cm² with maximum of 2.7 at 25 wt.% WC content.

The carried out investigations of dependence of hardness of the produced coatings on WC content in the electrodes showed a significant increase in hardness from 3 to 8.7 GPa.

For restoration of hardened steel parts those electrodes appeared to be optimal which contain 50–60 % WC. While using the alloy with 50 % WC the hardness of coating was about 5 GPa, however its transfer to the substrate is by 25 % lower than that of Colmonoy alloy. In case of using alloy with 60 % WC the hardness of coating was 7 GPa. Its mass transfer is by 1.5 times lower than for Colmonoy. This is sufficient to produce coatings of up to 2 mm thickness. The alloy with 70 % WC allows producing coatings with hardness of 8.7 GPa, but its transfer is by 5 times lower than that of Colmonoy.

The carried out investigations showed that changing the ratio of components in Colmonoy–WC alloy, according to specific needs, the coatings with different thickness, as well as hardness, can be produced. For example, on steel 45 thickness of electrode Colmonoy material was 4.2–4.8; Colmonoy–25 % WC — 4.0–4.5; Colmonoy–50 % WC — 3.2–3.8 mm. The developed alloys are recommended for restoration of worn-out parts of structural steels.

It should be noted that the surface of coatings produced in installation ELITRON-52 at powerful pulse energy is «hilly» and requires further machining.

The investigation of kinetics of mass transfer of Colmonoy–WC alloy to steel 45 was carried out in installation EFI-46A under the following conditions: oscillation frequency of 100 Hz, short-circuit current of 4 A, operating current of 1.5–2.0 A, energy of one discharge of 0.28 J (which is 27 times lower than the energy in ELITRON-52), period of treatment of 10 min/cm². The kinetics of changes of erosion of the anode and mass increasing of the cathode was determined for each minute of treatment of 1 cm² of the substrate (steel 45).

Figure 1 shows the dependences of mass increment of cathode Δ_c at electric erosion treatment of surface of steel 45 with alloys of Colmonoy–WC system and standard VK20 alloy.

The microhardness of coatings produced in installation EFI-46A is presented in Figure 2. The comparison of microhardness values of coating with 10 % WC with the coating containing 70 % WC showed that microhardness of the latter, depending on the distance from the surface, 5 times exceeds the microhardness of the Colmonoy–10 % WC coating.

The investigations of friction and wear of coatings on steel 45 under the conditions of dry sliding friction in air at room temperature according to the shaft–plane scheme were performed in the friction machine at sliding speed of 10 m/s and loading of 10 kg [4]. The coatings at the end surface were treated to smoothness $Ra = 0.2 \mu\text{m}$. The coefficient of friction f and wear intensity I was determined. For comparison, the specimens of steel 45 without coating were tested. The test results are given in Table 1.

The results of carried out investigations showed that wear resistance of coatings is increased with increase in the content of WC. The wear resistance of coating at application of the electrode with 70 % WC is almost 9 times higher than the wear resistance of steel.

The carried out investigations of properties of electric spark coatings (mass transfer, thickness, hardness and wear resistance) enabled the determination of the optimum content of alloying elements: Cu — 4–5,

Table 1. Wear rate of coatings of Colmonoy–WC system on steel 45 at $P = 10 \text{ kg}$ and $v_{sl} = 10 \text{ m/s}$

Electrode material	$I, \mu\text{m}/\text{km}$	f
Colmonoy	64.5	0.29
Colmonoy + 10 % WC	60.8	0.28
Colmonoy + 25 % WC	58.6	0.30
Colmonoy + 38 % WC	37.5	0.37
Colmonoy + 60 % WC	37.0	0.38
Colmonoy + 70 % WC	18.5	0.30
Steel 45	160	0.40

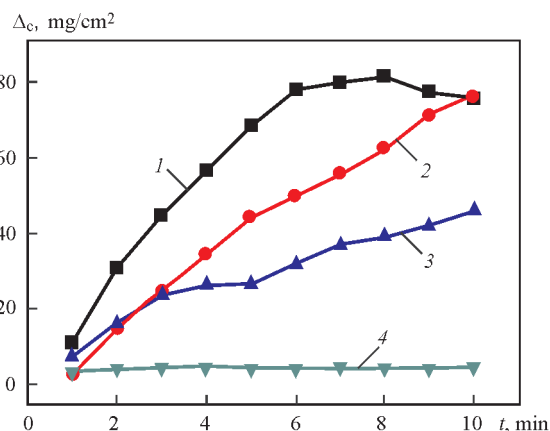


Figure 1. Kinetic dependences of mass increment of cathode at electroerosion treatment of steel 45 using alloys of Colmonoy–WC system and alloy VK20: 1 — Colmonoy–25 % WC; 2 — Colmonoy; 3 — Colmonoy–70 % WC; 4 — VK20

B — 0.5–0.7, Si — 3.2 %, that allows the formation of eutectics Ni–Ni₃B–Si–Cu, the low melting point of which allows obtaining the high values of mass transfer of the electrode material on the part surface. By WC content the hardness of the coating is regulated.

Electrode materials based on titanium carbides.

As the objects of investigations the alloys based on titanium carbides with additions of refractory compounds (Mo₂C, TiN), as well as metals (Co, Cr, Al and Ni) were selected. During manufacture of specimens the powders of refractory compounds of the Donetsk Plant of Chemical Reagents, as well as technical powders of Ni, Co and Cr were used.

The specimens of the alloys were manufactured by grinding of components in preset ratio in the planetary mill with subsequent hot pressing. The grinding of powder mixtures TiC–Mo₂C–Co–Cr, TiC–Mo₂C–TiN–Co–Cr and TiC–Co–Ni–C were carried out in acetone at powder:steel balls ratio of 1:5 within 30 min. The size of particles of the main fraction of the produced mixtures was less than 1 μm. The hot pressing of specimens in the graphite press molds was carried out in hydraulic press at 1420–1500 °C, 30 MPa and

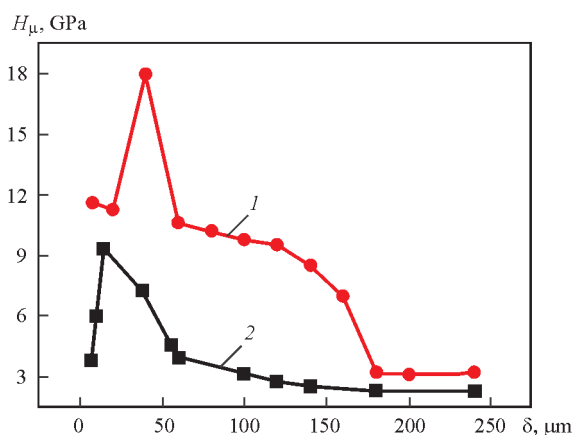


Figure 2. Microhardness of coatings versus distance to the surface: 1 — Colmonoy–70 % WC; 2 — Colmonoy–10 % WC

Table 2. Phase composition and microhardness of electrode materials

Composition of alloy, wt.%	H_{μ} , GPa	Phase composition of alloys
1. TiC–5Mo ₂ C–12Co–5Cr	27.0	TiC _{1-x} , Cr ₃ C ₂ , Mo ₂ C, CoTi ₂ , Ti _x O _{2x-1}
2. TiC–5Mo ₂ C–10TiN–12Co–5Cr	25.6	TiCN, Cr ₂ Ti, Co ₃ Ti, Ti _x O _{2x-1}
3. TiC–12Co–3Ni–0.5C	24.5	TiC _{1-x} , β-Co, Ti _x O _{2x-1}

Table 3. Phase composition of coatings of alloys based on titanium carbide on steel substrate

Composition of alloy, wt.%	Phase composition of coatings on substrate of steel 45
1. TiC–5Mo ₂ C–12Co–5Cr	TiC _{1-x} , Cr ₇ C ₃ , Ti _x O _{2x-1} , Co(Ti), Cr ₂ Ti
2. TiC–5Mo ₂ C–10TiN–12Co–5Cr	TiCN, Ti _x O _{2x-1} , Co(Ti), Co ₃ Ti, FeTi
3. TiC–12Co–3Ni–0.5C	TiC _{1-x} , Co(Ti), Ti _x O _{2x-1} , Fe ₂ O ₃ , CoO, CoTi ₂

sintering duration of 5–20 min. The relative density of hot-pressed specimens amounted to 0.96–0.98.

The developed titanium carbide alloys were used as electrode materials for deposition of protective coatings on the substrate of steel 45. Electric spark treatment of steel surfaces was performed in installation ELITRON-22A at $I_{op} = 0.8, 1.3, 1.8$ and 2.3 A. In the process of investigations the mass of eroded anode and mass increment of cathode were determined. The investigations of phase composition of hot-pressed specimens of titanium carbide alloys and structure of protective electric spark coatings of them on the steel substrate were performed in installation DRON-3M in CuK_{α} radiation. The electron microscopic examinations of substructure and fractures of hot-pressed specimens based on titanium carbide as well as formed layers on the steel substrate (in depth) was performed in installation PEMU SelMI. The density of the produced specimens was determined using the method of hydrostatic weighing on analytical balance of ADV-200 type, the microhardness was measured in microdurometer PMT-3 at loading of 1 N to indenter.

The X-ray phase analysis of electrode materials of the following compositions was carried out, wt.%: TiC–12Co–3Ni–0.5C, TiC–5Mo₂C–12Co–5Cr and TiC–5Mo₂C–10TiN–12Co–5Cr as well as coatings, deposited on the steel 45 substrate using the specified electrode alloys (Tables 2 and 3).

According to the data of X-ray investigations the steel substrate represents α -Fe with a very small amount of iron oxide Fe₂O₃. The main phase of electrode alloy TiC–Co–Ni–C is the non-stoichiometric composition titanium carbide in the homogeneity region TiC_{1-x}. Moreover, β -Co and the lines of a very weak intensity presented at the diffractogram were revealed, which are indentified as titanium oxide Ti_xO_{2x-1}. In electrode TiC–Mo₂C–Co–Cr similarly to electrode TiC–Co–Ni–C the main phase is titanium carbide of non-stoichiometric composition in the ho-

mogeneity region TiC_{1-x}. Chromium carbide Cr₃C₂ was also revealed. Also, according to the diffractogram the traces of Co(Ti), Mo₂C, intermetallic CoTi₂ and titanium oxide Ti_xO_{2x-1} are present in the electrode material. In alloy TiC–Mo₂C–TiN–Co–Cr the main phase is titanium carbonitride TiCN. In the diffractogram the weak lines are also present which are identified as intermetallics Cr₂Ti, Co₃Ti, as well as very weak lines of titanium oxide Ti_xO_{2x}.

The developed alloys have a similar structure and differ only in the dispersion. In alloy TiC–Mo₂C–Co–Cr the size of grains of titanium carbide reaches 10 μ m, and in alloy TiC–Mo₂C–TiN–Co–Cr it does not exceed 5 μ m. In these alloys, according to the data of local X-ray analysis, the grain boundary interlayers, containing Co and Cr, are observed.

In alloy TiC–Co–Ni–C the grains of titanium carbide of 2–10 μ m size are separated by the interlayer of the grain-boundary phase of up to 1 μ m thickness. The grain-boundary phase according to the data of local X-ray analysis contains cobalt and nickel. In the specimen the pores (mainly at the grain boundaries) of up to 10 μ m are observed.

Figure 3 shows kinetics of increment of mass of the steel 45 cathode at electric spark alloying using electrodes of titanium carbide hard alloys, as well as standard alloy TN-20 (TiC–15 % Ni–6 % Mo).

The maximum effect during formation of protective coating on steel substrate is observed when the alloy is used based on titanium carbide, containing molybdenum carbide, cobalt and chromium. At the same time, the mass of the transferred electrode alloy to steel substrate is more than 3 times higher as compared to standard hard alloy TN-20.

According to the results of X-ray phase analysis (see Table 3), in the coatings produced using electric spark alloying with $I_{op} = 0.8$ and 1.3 A and electrode TiC–Co–Ni–C, the main phase is titanium carbide of non-stoichiometric composition in the region of ho-

mogeneity TiC_{1-x} with interplanar distance which is slightly smaller than that in the electrode material. In the coating the solid solution of titanium in cobalt $\text{Co}(\text{Ti})$ and titanium oxide $\text{Ti}_x\text{O}_{2x-1}$ are also present. In addition, the components of the substrate iron and iron oxide Fe_2O_3 — are manifested in the coating as well as weak lines are observed which may indicate the presence of traces of cobalt oxide CoO and intermetallic CoTi_2 .

The carried out electron microscopic examinations of surface morphology of the electric spark coatings of alloys based on TiC showed that for all three coatings the presence of two kinds of morphologies on the surface is characteristic: the first one, when the surface is fused, the second one is represented by accumulation of rounded particles of the size from fractions of micron to $10\ \mu\text{m}$. In the coatings, formed of the first two alloys, the accumulations of fine rounded particles are observed, in case of alloy 3 using the rounded particles are rather uniformly distributed over the surface. In the relatively smooth fused areas the cracks are observed. The investigation of the composition using the method of local X-ray analysis did not show differences in the composition of fused areas and the areas covered with accumulations of particles. The analysis of cross-sections of electric spark coatings of alloys based on titanium carbide on the steel 45 substrate showed that thickness of the formed coatings amounts to $50\text{--}100\ \mu\text{m}$.

On the same specimens the distribution of microhardness in the depth of coatings was studied (Figure 4). From the given data some abnormality in the change of microhardness in the depth of coating, namely, at distance of $10\text{--}15\ \mu\text{m}$ from the coating surface the microhardness is $7\text{--}9\ \text{GPa}$ with its subsequent increase with increase to $12\text{--}14\ \text{GPa}$ in distance from the surface. The explanation to this phenomenon should be sought in changing the content of elements across the thickness of coatings, for example, of oxygen in the subsurface layer. Thus, the lower the oxygen content, the lower is the presence of solid phases containing oxygen (see Table 3) in the process of formation of electric spark coatings.

The coatings of hard alloys based on titanium carbide were tested under the conditions of friction against the abrasive cloth of silicon carbide of R 1200 gritness. The wear intensity at abrasive friction of coating of alloy $\text{TiC}\text{--}\text{Mo}_2\text{C}\text{--}\text{Co}\text{--}\text{Cr}$ on friction path of up to $15\ \text{m}$ is 2 times lower as compared to steel 45.

The wear resistance, determined during friction against the abrasive cloth, is a fundamental characteristic of strength properties of the specimen surface layer. The relative wear resistance in dimensionless units gives a quantitative estimation of resistance to

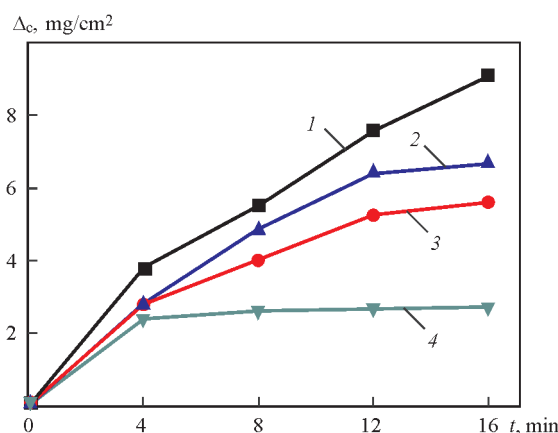


Figure 3. Kinetics of mass increment of steel 45 cathode during electric spark alloying using alloys based on titanium carbide: 1 — $\text{TiC}\text{--}\text{Mo}_2\text{C}\text{--}\text{Co}\text{--}\text{Cr}$; 2 — $\text{TiC}\text{--}\text{Mo}_2\text{C}\text{--}\text{TiN}\text{--}\text{Co}\text{--}\text{Cr}$; 3 — $\text{TiC}\text{--}\text{Co}\text{--}\text{Ni}\text{--}\text{C}$; 4 — TN-20

material fracture. The obtained data combined with the data on coating hardness in the cross-section confirm the effectiveness of electric spark strengthening of steel surfaces with the developed materials.

The evaluation of tribological properties of specimens of steel 45 with electric spark coatings deposited in installation ELITRON-22A at $I_{\text{op}}\ 1.3\ \text{A}$ using electrodes of the developed alloys based on titanium carbide and those of the standard alloy TN-20 was carried out. The tests for friction and wear were carried out according to the shaft–plane scheme in the friction machine [4] at $v_{\text{sl}}\ 0.5, 1.2$ and $3\ \text{m/s}$ and $P = 1\ \text{MPa}$. As the counterbody the ring (shaft) of $40\ \text{mm}$ diameter of hardened steel 45 ($HRA\ 42\text{--}48$) with roughness of working surface $Ra = 0.2\ \mu\text{m}$ was used. The tests were carried out in air without lubrication. The friction path amounted to $3\ \text{km}$. The temperature in the contact zone was measured at distance of $0.3\ \text{mm}$ from the friction surface. The wear rate was determined by weighing the specimen with coating before and after tests.

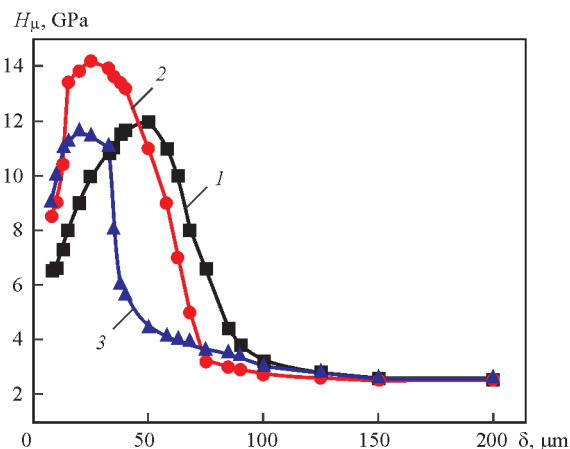


Figure 4. Distribution of microhardness in depth of coatings produced at alloying the steel 45 substrate using carbide-titanium solid alloys: 1 — $\text{TiC}\text{--}\text{Mo}_2\text{C}\text{--}\text{Co}\text{--}\text{Cr}$; 2 — $\text{TiC}\text{--}\text{Mo}_2\text{C}\text{--}\text{TiN}\text{--}\text{Co}\text{--}\text{Cr}$; 3 — $\text{TiC}\text{--}\text{Co}\text{--}\text{Ni}\text{--}\text{C}$

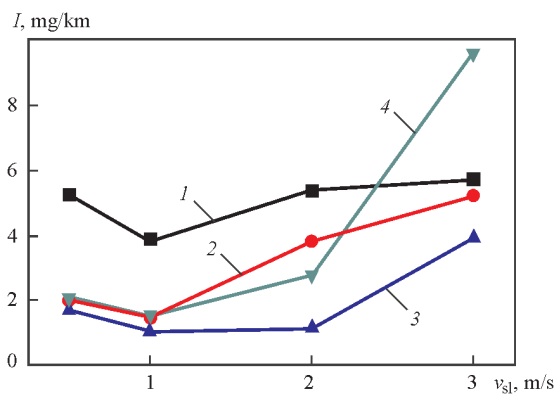


Figure 5. Sliding speed versus wear intensity of electric spark coatings during friction against steel 45: 1 — TiC–Mo₂C–Co–Cr; 2 — TiC–Mo₂C–TiN–Co–Cr; 3 — TiC–Co–Ni–C; 4 — TN-20

Figure 5 shows the dependence of wear intensity of electric spark coatings of the developed electrode materials on steel 45 substrate at different sliding speeds. The temperature in the contact zone changed depending on sliding speed in the range of 92–275 °C. The temperature growth in the contact area in all the pairs with increase in the sliding speed results in increase in wear intensity and reduction in friction coefficient. The investigations showed that the coatings produced at sliding speed of 2 m/s during friction against steel 45 have a high wear resistance and can be used in friction pairs.

Practical application of the developed electrode materials. The application of new composite electrode materials Colmonoy–WC allows producing electric spark coatings of up to 2–4 mm thickness with wear resistance 5–10 times higher than that of steel 45. By changing the ratio of components of Colmonoy and WC it is possible to produce coatings on the structural steels with a wide spectrum of properties. To restore the parts of steel St3 or non-hardened steel 45 it is rational to use coatings of alloy containing up to 25 wt.% WC. To restore the parts of hardened steels it is necessary to use coatings of alloy containing 50 wt.% WC. The work was carried out for the practical application of materials and technology of



Figure 6. Mine hydraulic support posts after restoration using method of electric spark alloying

electric spark strengthening and restoration of metal surfaces at the enterprises «Tekhmashkompani» and «Ukrmetallurgremont» (Dneprodzerzhinsk, Ukraine).

One of the causes of fracture of machine parts is fretting corrosion, which occurs at the interface between the two bodies contacting with each other. The combination of natural corrosion with fretting- and mechanical wear of two surfaces having a relative small mutual displacement results in a significant increase in the degree of wear of surfaces and the danger of local fracture. The wear has a form of so-called pits (cavities), reaching a considerable depth. To such pairs the contacting surfaces of bearing, nicks, key connections, press fits, parts of electric motors, cam mechanisms and adjoining shafts belong. These pits lead to fatigue fracture and local fracture. Removing of these pits, especially on the parts where thermal effect on the metal is not admitted, is almost impossible. Only electroerosion treatment allows correcting this defect, but in this case the depth of pits can not exceed 0.4 mm. Colmonoy–WC alloy developed by the authors allows increasing the spot thickness of the deposited layer to 1.8 mm, which allows considerably expanding the range of repairable parts.

Colmonoy–WC alloy was successfully used at the enterprise «Tekhmashkompani» for restoration of rods of mine hydraulic support posts (Figure 6) operating in wet environment, and at long operation the spot cavities are formed on the surface of rod in the place of contact with the lower and upper supports of the post, leading to a loss of tightness in the assembly and a sharp decrease in the load, perceived by the post. This causes a need in repair of supports. The electroerosive elimination of cavities with subsequent smoothing instead of currently applied surfacing of the whole surface of rod with subsequent machining allowed a significant reducing the restoration period of the support and 3 times shortening the repair costs.

The industrial tests of Colmonoy–WC alloy showed that according to a number of values it is superior to the alloys of VK and Stellite type, which at the present time are applied in electric spark restoration. The maximum thickness of the deposited layer was increased from 0.5 to 1.8 mm.

Under the industrial conditions the technology of electric spark deposition of coatings was implemented for restoration of seat surfaces of axles of crane trolleys of overhead cranes, seat holes in the body of axle of crane trolley, seat holes of bearings in the lids of electric motors and for strengthening of tools. The axle of the crane trolley has diameter of 100 mm and length of 700 mm. It is manufactured of steel 45. In the process of operation the seat surface at the ends of axles of 40 mm width is worn out. The amount of

wear reaches 0.4 mm. The restoration is performed completely without subsequent machining. The operator determines the required thickness of coating and restoration and, by selecting one of the nine modes of installation EIL8a, deposits the required layer on the surface of the part. The restoration of seat holes of bearings in the lids of electric motors is carried out using the same technology.

Electric spark alloying was used to restore the shafts of electric motors. Previously, these shafts were replaced by the new ones. The restoration of shafts using the method of electric arc surfacing on the worn-out bearing seats of metal alloys showed that as a result of high temperature of surfacing the structural changes occur in steel of the shaft, and, therefore, it provokes a deformation which cannot be corrected using machining. In the electric motor the beat appeared and it became unfit for operation. The problem was solved by using the method of electric spark alloying. Electrode material Colmonoy-50 % WC was used at the enterprise «Elektromash» (Sumy, Ukraine) for local strengthening of plough shares in installations «Elitron-22A» and «Elektron-52A» and restoration of mill rolls and seats of industrial fans (Figure 7).

Conclusions

1. The technology of producing eutectic alloy Ni-Ni₃B (Colmonoy) with WC additives was developed. The presence of eutectic structures in the designed electrodes was revealed. It is shown that the hardness increases from 2.8 to 8.7 GPa with increase in WC content, respectively, for Colmonoy and Colmonoy-70 % WC alloys. The thickness of coatings is reduced from maximum of 4.2–4.8 mm for Colmonoy to 3.2–3.8 mm for the alloy with 50 % WC. The microstructure of the produced coatings has a character of thin conglomerate of phases based on nickel and WC. The wear resistance of coatings of Colmonoy-



Figure 7. Restoration of seats of industrial fans

WC is 3–5 times higher than the wear resistance of steel 45.

2. The coatings on metallic substrates deposited with electrodes on TiC base have thickness of 50–100 μm, about 80 % of continuity and microhardness of 12–14 GPa. During sliding friction the wear resistance of coatings of the developed alloys based on TiC is 2–4 times higher as compared to the coatings of standard alloy TN-20.

3. The implementation of technology of electric spark treatment of worn-out surfaces and of new electrode materials 1.5–2 times increases the resistance of parts and tools and 3–5 times shortens the costs associated with the repair of equipment.

1. Borisov, Yu.S., Kharlamov, Yu.A., Sidorenko, S.L. et al. (1987) *Gas-thermal coatings of powder materials*: Refer. Book. Kiev: Naukova Dumka.
2. Paustovsky, A.V., Tkachenko, Yu.G., Alfintseva, R.A. et al. (2013) Optimization of composition and properties of electrode materials and electric spark coatings during strengthening and repair of metallic surfaces. *Elektron. Obrab. Materialov*, 49(1), 4–13.
3. Umansky, Ya.S., Trapeznikov, A.K., Kitajgorodsky, A.I. (1951) *Radiography*. Moscow: Mashgiz.
4. Kolesnichenko, L.F., Polotaj, V.V., Zabolotny, L.V. (1970) Method for investigation of friction and wear of cermets. *Poroshk. Metallurgiya*, 3, 61–66.

Received 25.12.2015

PATON PUBLISHING HOUSE

www.patonpublishinghouse.com

SUBSCRIPTION

The Paton
WELDING JOURNAL

«The Paton Welding Journal» is Published Monthly Since 2000 in English, ISSN 0957-798X.

**АВТОМАТИЧЕСКАЯ
ВАРКА**

«Avtomaticeskaya Svarka» Journal (Automatic Welding) is Published Monthly Since 1948 in Russian, ISSN 005-111X.

«The Paton Welding Journal» is Cover-to-Cover Translation of Avtomaticeskaya Svarka» Journal into English.

If You are interested in making subscription directly via Editorial Board, fill, please, the coupon and send application by Fax or E-mail.

The cost of annual subscription via Editorial Board is \$348 for «The Paton Welding Journal» and \$180 for «Avtomaticeskaya Svarka» Journal.

«The Paton Welding Journal» can be also subscribed worldwide from catalogues subscription agency EBSO.

SUBSCRIPTION COUPON

Address for journal delivery _____

Term of subscription since _____

20

till _____

20

Name, initials _____

Affiliation _____

Position _____

Tel., Fax, E-mail _____

We offer the subscription all issues of the Journal in pdf format, starting from 2009.

The archives for 2009–2014 are free of charge on www.patonpublishinghouse.com site.



ADVERTISEMENT

in «Avtomaticeskaya Svarka» and «The Paton Welding Journal»

External cover, fully-colored:

First page of cover (190×190 mm) — \$700
Second page of cover (200×290 mm) — \$550
Third page of cover (200×290 mm) — \$500
Fourth page of cover (200×290 mm) — \$600

Internal cover, fully-colored:

First/second/third/fourth page of cover (200×290 mm) — \$400

Internal insert:

Fully-colored (200×290 mm) — \$340
Fully-colored (double page A3) (400×290 mm) — \$500

- Article in the form of advertising is 50 % of the cost of advertising area
- When the sum of advertising contracts exceeds \$1001, a flexible system of discounts is envisaged

Size of journal after cutting is 200×290 mm

Editorial Board of Journal «Avtomaticeskaya Svarka» and «The Paton Welding Journal»

E.O. Paton Electric Welding Institute of the NAS of Ukraine

International Association «Welding»

11 Kazimir Malevich Str. (former Bozhenko Str.), 03680, Kiev, Ukraine

Tel.: (38044) 200 60 16, 200 82 77; Fax: (38044) 200 82 77, 200 81 45

E-mail: journal@paton.kiev.ua; www.patonpublishinghouse.com